Quantum Scale Plasmonic Material for Biomedical Applications

By

Ayushi Agarwal

Master of Technology in Biotechnology

SRM University, Chennai, India, 2016

Bachelor of Technology in Biotechnology

SHIATS University, Allahabad, India, 2014

A dissertation

presented to Ryerson University in partial fulfillment of the

requirements for the degree of

Doctor of Philosophy

in the program of

Mechanical and Industrial Engineering

Toronto, Ontario, Canada, 2020

Author's Declaration

I hereby declare that I am the sole author of this dissertation. This is a true copy of the dissertation, including any required final revisions, as accepted by my examiners. I authorize Ryerson University to lend this dissertation to other institutions or individuals for the purpose of scholarly research. I further authorize Ryerson University to reproduce this dissertation by photocopying or by other means, in total or in part, at the request of other institutions or individuals for the purpose of scholarly research. I understand that my dissertation may be made electronically available to the public.

Quantum Scale Plasmonic Material for Biomedical Applications

Ayushi Agarwal, 2020

Doctor of Philosophy

Mechanical and Industrial Engineering, Ryerson University

Abstract

Here physically synthesized (non-chemically engineered) gold quantum particles were investigated to study the structural behavior of genomic DNA towards gold particles in the microcellular environment for sensing, diagnosis, and therapeutics nanomedicine application. The non-conformational changes in genomic DNA were witnessed for three different cell types: lung cancer cells (H69), pancreatic cancer cells (ASPC-1), and healthy fibroblast cells (NIH 3T3). By the intracellular chemical analysis of gold quantum particles, results show that the gold quantum particles remain in their native chemical state (Au (0)) after internalizing inside the nucleus, and do not undergo a redox reaction in the cellular environment which leads to the low affinity of gold ions towards the cellular components. The physically synthesized native gold quantum particles do not fluctuate the sodium concentration inside the nucleus which is known to impact the stability of the genomic DNA structure directly. In contrast to commonly used gold particles the ultrafast laser synthesized (physically engineered) quantum size native gold particles can be internalized inside the cells as well as the nucleus without causing any conformational changes in secondary genomic DNA structure. Additionally, label-free gold quantum particles were used for cancer sensing to provide the opportunity to attain the sensing of oncoprotein and nuclear components instantaneously. Since the gold quantum particles are non-toxic, no layering is required, enabling the study of the exact quantum effect in plasmonic cellular signaling. The naked gold quantum particles confirmed self-cellular uptake with even

distribution and non-specific attachment to all the cellular components. The gold quantum particle size is found to be inversely related to the signal strength of the plasmonic readout. The gold quantum particles provide a holistic picture of cell states and may open up new possibilities for accurate SERS diagnosis of cancer. Adding to this the concept of small-sized self- functionalized pristine also introduced gold quantum particles for cancer theranostics. The pristine gold quantum particles demonstrated cancer-selective cell uptake enabling dosage- dependent fluorescent detection/differentiation of cancerous cells and cancer-selective cytotoxicity. The fabricated gold quantum particles demonstrated fluorophore-free fluorescence illuminance at a broad range of excitation wavelengths and drug-free cancer-specific treatment. According to this study the as-fabricated gold quantum particles have dual functions of fluorescent diagnosis and treatment of cancerous cells. Moreover the drug-free gold quantum particles may find advantages in fighting drug-resistant cancers. Here the current research opens a frontier for the future of gold-based nanomedicine and its application for sensing, diagnosis, and therapeutics in *in vitro* environment.

Acknowledgments

First and foremost, I would like to take this opportunity to express my profound gratitude and sincere regards to the benevolent advisors **Dr. Krishnan Venkatakrishnan and Dr. Bo Tan**, Department of Mechanical and Industrial Engineering and Department of Aerospace Engineering, for their excellent guidance, monitoring and constant encouragement throughout this research. The blessing and guidance given by them time to time shall carry me a long way in the journey of life on which I am about to embark.

I am profoundly thankful to the committee members **Dr. Vincent Chan and Dr. Ziad Saghir,** for their ingenious advice, guidance, and constructive counsel for this research work.

Literary skills grope in the dark when it comes to express what I owe to my parents and my brother Aman. The mean achievement to which I lay claim today has all precipitated from the sincere prayers and silent sacrifice of my family. I will always seek their blessings in my life.

I would like to express my heartiest gratitude to my partner Amol. All the sacrifices and being away from home, he was there to support me, encourage me, and never let me give up on my parents' dream. He stood by me when I was struggling the most and encouraged me throughout. Without his unwavering support, I would not have achieved what I have.

I express my appreciation to all the members of my family and my friends for being a source of active encouragement and inspiration throughout my life and educational career.

Last but not least, I wish to acknowledge the untiring help of all the Ph.D. scholars of the Ultrashort Laser Nano manufacturing lab for their help and support during my entire research work. Swarna Ganesh was always there with ideas and would help me whenever I needed, and I am incredibly grateful for that.

I offer my sincere thanks to "Almighty God" for standing by me at every step, and by whose blessing I have been able to conquer another task of my life.

Dedication

To my Maa, Papa, Aman and Amol

Table of Contents

List of Tables

List of Figures

List of Appendices

List of Abbreviations

- **DMSO**- Dimethyl Sulfoxide

- **CGM**- Complete Growth Medium

- **EDX**- Energy Dispersive X-ray

- **HR-TEM**- High resolution Transmission Electron Microscope

- **MRI**- Magnetic Resonance Imaging

- **NIR**- Near Infrared

- **SEM-** Scanning Electron Microscope

- **SERS**- Surface Enhanced Raman Scattering

- **TEM**- Transmission Electron Microscope

- **XPS**- X-ray spectroscopy

- **XRD**- X-ray Diffraction

- **NP**- Nanoparticles

- **NS**- Nanostructure

- **QD**- Quantum Dots

- **PQPs**- Plasmonic Quantum Probes

- **EGFR**- Epidermal Growth Factor Receptor

- **HPV**- Human Papilloma Virus

- **DNA**- Deoxyribose nucleic acid

- **PCA**- Principal Component Analysis

- **BQGPs**- Bright Quantum Gold Probes

- **PL**- Photoluminescence

List of Nomenclature

- Apoptosis- Programmed cell death
- Biocompatible- Characteristic of not being harmful in *in vivo* and *in vitro* environment
- Fibroblasts- Healthy cells
- *In vivo*- Outside the living organism
- *In vitro*- Inside the living organism
- Nucleus- Dense organelle in a cell that contains the genetic material of the cell
- Proliferation- cell division
- Theranostics- Simultaneous detection and treatment of cancer
- Biomarkers- Specific kind of proteins

Chapter 1

1.1 Introduction

Gold nanoparticles are extensively used for the evolution of nanomedicine due to their unique features such as small size, high surface area and highly tunable binding affinity [1]. Gold nanoparticles have a multifunctional ability where gold nanoparticles can be used for medical imaging, diagnosis and therapy [2]–[6] [7]. With gold nanoparticles it is easy to accomplish different biomedical applications with a single platform [4]. Gold nanoparticles attracted tremendous research interest due to their excellent physicochemical and optoelectrical properties that hold the potentials of improving specificity, accuracy, and sensitivity of early cancer detection [8]. Gold quantum dots have a size comparable to biomolecules that are capable of deciphering the mechanism of cancer invasion and progress at the molecular level.

1.1.1   Traditional synthesis of gold nanoparticles

Conventionally, gold particles are most commonly synthesized by using different chemical methods; for example, cetyltrimethylammonium bromide (CTAB) and trimethylammonium bromide (MTAB) [9], [10]. Chemical synthesis generates a bilayer of synthetic molecules on the surface of gold nanoparticles which dissociates from the surface of gold nanoparticles under physiological conditions resulting in toxicity [11]. Apart from the cytotoxicity chemical-deterioration on the surface of gold particles alter the DNA conformation, which distorts the diagnosis results. Adulteration may also cause mutation in healthy cells leading to different alterations in organs [10]. The toxicity and adulteration significantly interfere with the natural interaction between gold particles and cellular components therefore currently there is a limited understanding of gold particle-cell interaction.

1.1.2 Nuclear uptake of gold nanoparticles

Earlier studies have shown that the nuclear uptake of nanoparticles is difficult as the nuclear structure involves the nuclear membrane which consists of a double lipid layer, chromosomes which again consist of DNA, RNA, rRNA and other proteins and the nuclear lamina which include membrane-associated proteins [12]. The presence of a nuclear membrane keeps the macromolecule and many Nano-molecules from entering the nucleus. Only the particles which are synthesized explicitly for nuclear targeting (coated with a biocompatible layer or with specific proteins) or the particles which are extremely small (<5 nm) can only enter inside the nucleus [13]–[15]. Also to overcome the cytotoxicity of gold nanoparticles [16] researchers coat the nanoparticles with a biocompatible layer which allows the nuclear uptake of gold nanoparticles. The presence of a biocompatible layer increases the overall hydrodynamic diameter of the nanoparticles and results in a damaged nuclear envelope during the nuclear uptake mechanism [17]. Recent studies have used bare gold nanoparticles of 2.5 nm for the nuclear uptake mechanism. However, the gold nanoparticles of 2.5 nm and its interaction with DNA distorts the secondary structure which results in the de-condensation of nuclear chromatins [18].

1.1.3 Biomedical applications of gold nanoparticles

Gold nanoparticles have proven to be a versatile material for a broad range of biomedical applications with potential use in numerous areas like diagnosis sensing, *in vitro* and *in vivo* imaging and therapeutic techniques. With recent advances in size-tunable synthesize routes gold nanomaterials can be synthesized in a variety of structure their large specific surface, high surface activity, active antioxidant property, excellent biocompatibility and suitableness for manipulations at the molecular level. Due to the presence of charge on the surface of gold

nanomaterial they can be easily functionalized by all kinds of biomolecules such as drugs, genes and targeting ligands. The possibility of conjugate gold nanoparticles with a variety of biologically active moieties, especially with amine and thiol groups provides possibilities for critical biomedical applications. All of these particular properties have caused gold nanomaterial to be the potential material for various biomedical applications including biosensing, molecular imaging, and drug carriers.

1.1.4   Therapy applications of gold nanoparticles

Gold nanoparticles have numerous advantages and utilizations in several aspects of cancer therapeutics. Drug delivery is the prime application where gold-based nanomaterials can be used for therapeutic applications. Most studies in this area have centered on cancer treatment as targeted therapies are much needed in this field due to the harsh side effects of current broad- based treatments. Conjugates of gold nanoparticles with drug molecules play an essential role in the therapy of endocellular diseases. In chemotherapy (drug delivery) the involvement of gold nanoparticles increases the efficiency of drug delivery to target cells. Due to their unique properties like the high surface area of nanoparticles this provides the site for drug loading and drug stability and its property to functionalize the nanoparticle with a ligand that specifically binds to the cancer receptors which increases the specificity. Antibiotics or other drug molecules can directly conjugate with gold nanoparticles via ionic covalent bonding or by physical absorption. The binding of the drug molecules with the gold nanoparticles allows the intracellular triggered release once they are inside the acidic organelles. However, after drug delivery is completed the route of excretion for gold nanoparticles remains unknown.

Additionally, after the drug release gold nanoparticles deposits in organs like liver and kidney it leads to organ failure. Other cancer therapy techniques include photothermal and combination

therapy, gold nanoparticles exhibit unique photothermal properties like converting electromagnetic radiation into heat due to coherent oscillation of electrons in the conduction band which has been used for the thermal ablation (destruction) of cancer cells. Thus, laser- exposed gold nanoparticles could act as therapeutic agents by themselves and without the need for the drug during photothermal therapy. NIR lasers are most commonly used in gold nanoparticle-induced photothermal therapy. NIR exposure allows for high-depth photothermal therapy due to the higher penetration of laser into the tissues. However, due to high depth penetration of the NIR laser the healthy cells present around cancerous cells get affected which may damage other organs present near cancer. To improve the outcomes of photothermal and chemotherapy a combination of these therapies have been used. Gold nanoparticles have been intensely used for chemo-photothermal (combined) therapy because of two foremost attributes. Firstly, gold nanoparticles can be easily conjugated with drugs and also with other reactive groups of capping agents. Second, the tunable surface plasmonic property of gold nanoparticles can convert the irradiation into thermal energy. Till now most scientists have focused on the combined gold nanoparticle with doxorubicin drug together for treatment. However, the challenges generated by the combination of chemotherapy and photothermal therapy remain unsolved.

1.1.5 Imaging by using gold nanoparticles

Currently, the clinical diagnosis of cancer mainly depends on imaging techniques. This includes X-ray, computed tomography (CT), magnetic resonance imaging (MRI), photoacoustic imaging, and fluorescence imaging. Among these several researchers have shown more interest in the fluorescence imaging technique due to its relatively high sensitivity and controllable signal readout. Till now fluorescence imaging is used to monitor the uniformity of drug release and

drug effects. Moreover, fluorescence imaging is also hugely significant for visualizing the cellular activity and expression of particular molecules. In this context, noble metal gold is a promising nanomaterial as it offers optical chirality, fluorescence, and photoluminescence that will provide higher sensitivity and stability to the fluorophore used. Recent research has enlightened the feasibility of using gold nanoparticles because of their optical efficiency for bio- imaging applications. The gold nanoparticles are conjugated by the specific fluorophore (dye) which increases the life span of dyes and reduces fluorescence quenching. Under prolonged conditions the presence of chemical molecules degrades the chemical composition of gold nanoparticles which results in reduced fluorescence emission. Gold nanoparticles also carry a few more restrictions of using gold nanoparticles for fluorescence imaging, cytotoxic, and bio- conjugation of biocompatible material for cellular uptake. The appearances of gold nanoparticles have greatly improved the sensitivity, specificity, multiplexing, and turnaround times of molecular imaging. The presence of gold nanoparticles has shown a significant increase in the excitation of fluorescence probes. The plasmonic properties of the gold nanoparticles enable to study specimen with weak fluorescence emission sometimes even at the molecular level and provide the opportunity to utilize high-resolution imaging in order to overcome the diffraction limit. Fluorescence imaging has been used to examine the endocytic uptake process due to their intrinsic fluorescence many studied have used gold nanoparticles for the direct imaging of cells and animals. The presence of gold nanoparticles allows the direct imaging of their internalization process into cells. However, the practical application of *in vivo* imaging is still challenging due to the penetration depth of the scattered light in tissue samples. Fluorescence technique reported so far are only able to integrate a limited number of clinically useful functions thus narrowing its usefulness to image the tumor and track the uniform release of drug and other

biomolecule delivery and to image the drug effects. Concerns also remain with the fluorescence quenching and biocompatibility of gold quantum dots. There is a requirement for the development of a biocompatible, self-mobilize quantum gold particle that combines a variety of clinically advanced diagnosis and imaging techniques that can not only image the presence of cancer but can also diagnose cancer.

1.1.6   SERS based detection of cancer by using gold nanoparticles

Current approaches to cancer detection by SERS (Surfaced Enhanced Raman Spectroscopy) focuses on sensing cancer-related biomarkers and *in vitro* detection. The presence of gold nanoparticles near the Raman reporters increases the sensitivity of SERS signals the shorter the distance the stronger the SERS signal. The enhancement of SERS signals was mainly due to collective oscillations of the conduction electrons in the gold which generated an ultra-strong electromagnetic zone in the proximity of the nanostructures [19] resulting in the amplification of the inherently weak Raman signals of different biomolecules. Gold nanoparticles based SERS has been researched intensively not only for the detection of the individual building blocks of life like amino acids and cancer receptors but also for the complex functional structures like single-stranded DNA, RNA, antibodies, and proteins [20], [22]. So far, a cancer diagnosis is made by the SERS sensing of cancer receptors, markers, and aptamer and mutated DNA/RNAs using labels and tags. Each label or tag reveals one specific bio-marker providing limited tumor information [23], [24] due to the limited specificity of labels only single biomarker sensing was done [24]. The measurement of a single tumor marker is usually not sufficient to diagnose cancer. In order to attain full signature and precise cancer diagnosis label- free and simultaneous sensing of multiple biomarkers or nucleic acids are required.

1.2 Research objectives

The principal objective of the present research is to study and explore the possibilities of creating un-tamped and pure gold quantum particles for cancer theranostics and cancer detection.

a. To study the nuclear uptake the cytotoxic effect of quantum gold particles and how they influence the stability of the genomic DNA structure.

b. SERS sensing and differentiation of different cancer types by studying Raman readout of surface and intracellular markers.

c. SERS sensing and differentiation of different cancer types by studying Raman readout of nucleic acid (DNA) molecules.

d. Cancer theranostics by Fluorescence-based cancer cell sensing and differentiation and cancer therapy simultaneously.

1.3 Organization of the Dissertation

This dissertation has been organized in a chapters based manner that describes the synthesis of quantum scale gold particles by using the physical synthesis method (femtosecond laser ionization). Following is the list of manuscripts in peer-review and also already published in journals:

Chapter 2- studied the nuclear uptake cytotoxic effect of quantum gold particles and how they influence the stability of the genomic DNA structure. Here the physically synthesized native gold quantum particles do not induce conformational changes in the genomic DNA secondary structure even after internalizing inside the nucleus. The non-conformational modifications in genomic DNA were witnessed for three different cell types that are lung cancer cells (H69), pancreatic cancer cells (ASPC-1) and healthy fibroblast cells (NIH 3T3). By the

intracellular chemical speciation of gold quantum particles results show that the gold quantum particle remain in their native chemical state (Au (0)) after internalizing inside the nucleus and does not undergo a redox reaction in the cellular environment which leads to the low affinity of gold ions towards the cellular components. The physically synthesized native gold quantum particles do not fluctuate the sodium and potassium concentration inside the nucleus which is known to impact the stability of the genomic DNA structure directly. Visualization of genomic DNA structures including gel electrophoresis, UV analysis and fluorescence analysis confirms that there is no structural change in the dynamics of genomic DNA. In contrast to commonly used gold particles the ultrafast laser synthesized (physically engineered) quantum size native gold particles can be internalized inside the cells as well as the nucleus without causing any conformational changes in secondary genomic DNA structure. The nuclear localization of native gold quantum particles does not perturb the dynamic of microenvironment within the nucleus. This opens a frontier for the future of gold-based nanomedicine and its application for sensing, diagnosis and therapeutics.

Chapter 3- studied objective b (sensing and differentiation of different cancer types by studying Raman readout of surface and intracellular markers). Where the quantum sized Plasmonic Quantum Probes (PQPs) a potential tool for cancer sensing which provides the chance to attain the diagnosis of surface oncoprotein, intracellular oncoprotein, and nuclear metabolites instantaneously. By using multiphoton laser ionization (physical synthesis) biocompatible PQPs were synthesized without chemical adulteration and eliminated the need for biocompatible layering. The PQPs are non-toxic and no layering is required enabling the study of real quantum effect in plasmonic cellular signaling. The bare PQPs demonstrated self-internalized with even dispersion and non-specific attachment to all the cellular biomolecules. As a result, the Raman

spectra revealed rich information of multiple cell components including surface markers (e.g., EGFR), intracellular markers (e.g., HPV E6/HPV E7) and nuclear metabolites (e.g., DNA/RNA) simultaneously in one single Raman profile. Due to the variation in the number of probes inside the cells the signal strength of cancerous cells is prominently higher than that of healthy cells inferring that the variation of cancerous cells is conceivable through the analysis of the intensity of Raman signals. The probe size is found to be inversely associated with the signal strength of the plasmonic fingerprint. The PQP provides a holistic picture of cell states and may open up new possibilities for accurate diagnosis of cancer.

Chapter 4 explored the objective 4- SERS sensing and differentiation of different cancer types by studying Raman readout of nucleic acid (DNA) molecules. Here the physically synthesized small quantum probes are used for the intracellular sensing of DNA molecules without the need for labels and coatings. In this study the small quantum probes internalize inside the cells by endocytosis mechanism and internalize inside the nucleus through a diffusion mechanism. The presence of small quantum probes inside the nucleus increases the SERS enhancement yield by a minimum of 700 folds. The SERS signals resulted in the simultaneous sensing of multiple cellular components including DNA and proteins which can be used for the analysis of cancer. Raman spectra present the different signal configuration because of the different molecular composition and different cell phases. Therefore, by using Principal Component Analysis (PCA) and Hierarchical Clustering analysis it can identify a significant difference between malignant (lung cancer and pancreatic cancer) and non-cancerous cells.

Moreover, by using the same analysis lung cancer cells from pancreatic cancer cells were differentiated. This indicates that the un-tamped small quantum probes internalize inside the nucleus without altering the cellular metabolism and are capable of sensing genomic DNA

molecules more accurately. The present study holds a promising potential for developing a new technique for accurate diagnosis of cancer-based on cell DNA diagnosis.

Chapter 5- studied the Cancer theranostics by Fluorescence-based cancer cell sensing and differentiation and cancer therapy simultaneously. This chapter presents the small-sized self-functionalized pristine bright quantum gold probes (BQGPs) for cancer theranostics. It is the first time cell interaction of pristine quantum gold was investigated and the results suggest that it can be used for inorganic (label-free drug-free) cancer quantum-theranostics. Hereby using multiphoton ionization (physical synthesis) non-toxic BQGPs were synthesized without chemical contamination and eradicated the requirement of labeling. Since the BQGPs are free from labels they remained in small quantum size in theranostics application enabling the investigation of real quantum effect in cell interaction. The small quantum-sized BQGPs facilitate a new concept of inorganic cancer quantum-theranostics. The fabricated BQGPs demonstrated fluorophore-free fluorescence illuminance at a broad range of excitation wavelengths and drug-free cancer- specific treatment. According to this study the as-fabricated BQGPs have dual functions of fluorescent diagnosis and treatment of cancerous cells. Moreover, the drug-free gold quantum dots have advantages in fighting drug-resistant cancers.

1.4 Statement of Co-Authorship

The following persons and organizations contributed to the publications of the research undertaken as a part of this dissertation:

Ayushi Agarwal, Ryerson University- Ph.D. Candidate (1st Author)

Dr. Krishnan Venkatakrishnan, Ryerson University, Ph.D. supervisor- Co-Author

Dr. Bo Tan, Ryerson University, Ph.D. supervisor- Co-Author

Author details and their roles:

Manuscript 1- A revival of precious Nobel metal for nanomedicine- physically engineered gold quantum particles for intracellular non-conformational dynamics of genomic DNA presented in Chapter 2. Candidate and Co-authors worked together in designing the project, Candidate performed the experiments and wrote the manuscript, Co-Authors assisted in results, discussion, and editing the manuscript for the publication.

Manuscript 2- Cancer Signaling by Plasmonic quantum Probes presented in Chapter 3. Candidate, Co-authors worked together in designing the project, Candidate performed the experiments and wrote the manuscript, Co-Authors assisted in results, discussion, and editing the manuscript for the publication.

Manuscript 3- DNA based sensing of different cancer cells presented in Chapter 4. Candidate, Co-authors worked together in designing the project, Candidate performed the experiments and wrote the manuscript, Co-Authors assisted in results, discussion, and editing the manuscript for the publication.

Manuscript 4- Small Gold Quantum Probes for drug-free Cancer Theranostics presented in Chapter 5. Candidate, Co-authors worked together in designing the project, Candidate performed the experiments and wrote the manuscript, Co-Authors assisted in results, discussion, and editing the manuscript for the publication.

Chapter 2

A revival of precious Nobel metal for nanomedicine- physically engineered gold quantum particles for intracellular non-conformational dynamics of genomic DNA

Submitted in Applied Healthcare Materials

2.1 Abstract

Chemically engineered gold-based nanomaterials have been widely explored for nanomedicine applications such as sensing, diagnosis and therapeutics. However, it has been recently reported that chemically engineered gold nanomaterials alter the conformational dynamics of genomic DNA which limits the applicability of the data. Generally cell localized gold particles undergo an intracellular redox reaction for the formation of stable gold oxides which are highly toxic. Adding to this, the presence of ubiquitous thiol chemical groups on the surface of chemically engineered gold nanoparticles may alter the microenvironment within the nucleus and also inhibit the direct interaction between gold nanoparticles and genomic DNA. Hence, chemically engineered gold-based materials cannot be used for intracellular applications in nanomedicine. To elucidate this physically synthesized (non-chemically engineered) gold quantum particles were used to investigate the genomic DNA structural behaviour towards gold particles in the microcellular environment. In this study results show that physically synthesized native gold quantum particles do not induce conformational changes in the genomic DNA secondary structure even after internalizing inside the nucleus. The non-conformational modifications in genomic DNA for three different cell types were witnessed which are lung cancer cells (H69), pancreatic cancer cells (ASPC-1) and healthy fibroblast cells (NIH 3T3). By the intracellular chemical speciation of gold quantum particles results show that the gold quantum particle remain

in their native chemical state (Au (0)) after internalizing inside the nucleus and does not undergo a redox reaction in the cellular environment which leads to the low affinity of gold ions towards the cellular components. The physically synthesized native gold quantum particles do not fluctuate the sodium concentration inside the nucleus which is known to impact the stability of the genomic DNA structure directly. Visualization of genomic DNA structures including gel electrophoresis, UV analysis and fluorescence analysis and further confirms that there is no structural change in the dynamics of genomic DNA. In contrast to commonly used gold particles the ultrafast laser synthesized (physically engineered) quantum size native gold particles can be internalized inside the cells as well as the nucleus without causing any conformational changes in secondary genomic DNA structure. The nuclear localization of native gold quantum particles does not perturb the dynamic of microenvironment within the nucleus. This opens a frontier for the future of gold-based nanomedicine and its application for sensing, diagnosis and therapeutics.

2.2 Introduction

Gold nanoparticles are the most commonly explored plasmonic materials for applications in medicine. The development of gold nanoparticles in nanomedicine has directed the growth of different techniques for cancer treatment, diagnosis, mutation detection and imaging of damaged organisms [2]–[6].

Gold nanoparticles are extensively used in the evolution of nanomedicine due to their unique features such as small size, high surface area and highly tunable binding affinity [1]. Gold nanoparticles have a multifunctional ability where gold nanoparticles can be used for medical imaging, diagnosis and therapy [7]. With gold nanoparticles it is easy to accomplish different biomedical applications with a single platform [4]. Therefore, it is crucial to study the interaction of gold particles with cellular components. However, as gold nanoparticles are researched for

different nanomedicine applications it is difficult to ignore its toxic nature [25] and the DNA changes generated by gold nanoparticles [9]. Traditionally, gold particles are most commonly synthesized by using different chemical methods for example cetyltrimethylammonium bromide (CTAB) and trimethylammonium bromide (MTAB) [9], [10]. Chemical synthesis generates a bilayer of synthetic molecules on the surface of gold nanoparticles which dissociates from the surface of gold nanoparticles under physiological conditions resulting in toxicity [11]. Apart from the cytotoxicity chemical deterioration on the surface of gold particles alter the DNA conformation which distorts the diagnosis results. Adulteration may also cause mutation in healthy cells leading to different alterations in organs [10]. The toxicity and adulteration greatly interfere with the natural interaction between gold particles and cellular components therefore currently there is limited understanding of gold particle-cell interaction.

The intracellular study of DNA and gold nanoparticle interaction is essential because different proteins and other cellular metabolites present in the cellular environment may also affect the DNA structure. However, most of the previous researchers have studied the interaction between gold nanoparticles and DNA in the non-cellular environment because of the limited uptake [26]. Earlier researches have shown that the nuclear uptake of nanoparticles is difficult as the nuclear structure involves the nuclear membrane, which consists of a double lipid layer, chromosomes which consist of DNA, RNA, rRNA and other proteins and the nuclear lamina which include of membrane-associated proteins [12]. The presence of a nuclear membrane keeps the macromolecule and many nano-molecules from entering the nucleus. Only the particles which are synthesized explicitly for nuclear targeting (coated with a biocompatible layer or with specific proteins) or the particles which are extremely small (<5 nm) can only enter inside the nucleus [13]–[15]. Also, to overcome the cytotoxicity of gold nanoparticles [16] researchers

coat the nanoparticles with a biocompatible layer which allows the nuclear uptake of gold nanoparticles. The presence of a biocompatible layer increases the overall hydrodynamic diameter of the nanoparticles and results in a damaged nuclear envelope during the nuclear uptake mechanism [17]. Recent studies have used bare gold nanoparticles of 2.5 nm for the nuclear uptake mechanism. However, the gold nanoparticles of 2.5 nm and its interaction with DNA causes the distortion of the secondary structure which results in the de-condensation of nuclear chromatins [18].

Although DNA interaction with gold particles inside a cell is not investigated due to transmission issues the interaction has been studied outside a cell using isolated DNA, DNA binding proteins or nucleic acid sequences in the extracellular environment. However, few studies outside the cellular environment show that gold nanoparticles occupy free space available in the double-stranded structures and can interact with the nitrogen-based molecules this may cause conformational changes in the DNA structure [27]. It has been established that the binding of nanoparticles to DNA changes the properties of both the components (DNA and gold nanoparticles). Binding alters the chemical state and dispersibility of gold nanoparticles [28]. The interaction between nanoparticles with DNA may increase binding efficiency and cause conformational changes. Nanoparticles may also induce other changes in the DNA molecule for example, binding between DNA and nanoparticles promote the relaxations of the supercoiled DNA structure [29]–[31]. Besides gold nanoparticles of 5 nm inhibit the hybridization of DNA strands as the small nanoparticles cause non-specific interactions [31].

The chemical adulteration in gold nanoparticles alters the gene expression despite the gold nanoparticles localizing in the cytoplasm with no DNA interactions. Non-cellular environment studies have shown that adulteration of gold nanoparticles directly affect the stability of the DNA

structures by affecting the binding affinity of the nucleic acids present. Previous studies show that charges on nanoparticles also play a critical role in altering the DNA structure. For example, if the nanoparticles are positively charged the DNA is more likely to wrap and bind the nanoparticles. Whereas, if the nanoparticles are weakly charged then it will not induce the compaction of DNA [32]–[34]. Very few studies have shown this effect of gold nanoparticles on the DNA structure in the cellular environment. Even these studies do not indicate direct interaction of gold nanoparticles with the genomic DNA. For example, the research presented by Diwei Ho shows the indirect effect on genomic DNA studied the alteration in the gene expression of MYC, BCL2, and HNRPAB which has high, intermediate and low potential to form a G4-DNA structure.

Earlier researches show that gold nanoparticles are cytotoxic and alter the gene expression profiles in the cells following the internalization of gold nanoparticles in the cytoplasm [35]. Previous research shows that gold nanoparticles are cytotoxic despite their uptake in different cell types through different uptake mechanisms [26]. Gold nanoparticles localize within the cytoplasm of the cells with no nuclear localization. However, the presence of gold nanoparticles in the cytoplasm affects the stability and conformation of the DNA structure [35] affecting DNA binding proteins signals transmitted to the nucleus from the cytoplasm and the sequence of DNA [10]. It has also been reported that the internalization of gold nanoparticles alter the gene expression even though gold nanoparticles are internalized in the cytoplasm with no DNA interactions.

The above discussion shows that the current understanding of gold particle-cell interaction either inside or outside a cell is all based on chemical residual. Most of these responses show that the gold particles induce the DNA conformational changes by promoting the relaxation of

supercoiled DNA molecules and inhibit the hybridization of DNA strands[29], [30], [36]. It does not replicate the natural response of cellular components to a un-tamped gold particle.

In this study, chemical-free stable pure gold quantum particles (Au (0)) were achieved by using an ultrafast laser (non-chemically engineered). The physically engineered gold quantum particles demonstrated non-conformational alteration in the dynamics of genomic DNA in the microcellular environment. The native gold quantum particles exhibit non-cytotoxic behavior in the microcellular environment and internalize inside the cells and the nucleus by the endocytosis uptake mechanism. Results show that the gold quantum particles retain their chemical state after localizing inside the nucleus do not undergo leaching (oxidation) in the microcellular environment, which results in the low binding affinity of gold ions towards the genomic DNA resulting in non-conformational changes in the genomic DNA structure. It was studied that the presence of native gold quantum particles does not disturb the ionic balance (sodium and potassium ion concentration) inside the cellular environment which is known to impact the stability of the genomic DNA structure directly. The non-conformational changes in the dynamic of genomic DNA were witnessed in three different cell types: pancreatic cancer (ASPC-1), lung cancer (H69) and healthy fibroblast cells (NIH3T3). Additionally, visualization of intact genomic DNA bands presented in gel electrophoresis, UV analysis and fluorescence analysis proved that the nuclear localization of the gold quantum particles do not perturb the dynamic microenvironment within the nucleus, and does not affect the genomic conformation of the DNA structure. These results imply that physically engineered native gold quantum particles do not alter the conformational dynamic of genomic DNA. Therefore, this research is a breakthrough for non-toxic gold quantum particles in the era of nanomedicine applications.

2.3 Materials and Methods

The details of the experiment performed to achieve the objective-1 study the nuclear uptake the cytotoxic effect of quantum gold particles and how they influence the stability of the genomic DNA structure are explained in this section.

2.3.1 Synthesis of gold quantum particles

A tunable Yb doped laser from the Impulse series (Clark-MXR) with a central wavelength of 1030 nm. This ultra-short pulsed laser system utilizes varying power between 1 to 17 watts and varying laser repetition rate between 200 kHz to 25 MHz to synthesize plasmonic quantum particles. The laser beam was focused on the gold-coated silicon wafer. The gold coated silicon samples were mounted on an x-y precision stage normal to the laser beam. To maximize the fabrication the power of the laser was kept constant. The gold quantum particles were created over an array of lines with uniform spacing.

2.3.2 Material Characterization of synthesized gold quantum particles

A high-Resolution Transmission Electron Microscopy (HRTEM) was used to determine the size and morphology of synthesized gold quantum particles. The elementary analysis was done by using EDX (Hitachi SU8200). EDX showed the composition of gold, silicon, oxygen and nitrogen in the synthesized gold probe. To quantify the chemical state of gold, silicon and oxygen XPS was used. Besides this to identify the oxide phase quantitatively and qualitatively, X-ray diffraction (XRD) was performed.

2.3.3 Stability analysis of gold quantum particles

For stability, the nanoparticles were treated with the Phosphate Saline Buffer (PBS) and complete growth medium (DMEM) for 24 hours. A high-Resolution Transmission Electron Microscopy (HRTEM) was used to determine the hydrodynamic size of the gold quantum particles. To study the chemical stability XPS analysis was performed.

2.3.4 Cytotoxicity analysis

Cytotoxicity evaluation of synthesized gold quantum particles was performed by using MTT assay, as described by Sigma Aldrich. Approximately 1×10^6 ml^{-1} cells per well in 96 well plate for 24 hours at 37°C in a 5% CO_2 incubator. Cells were treated with gold nanoparticles. After 24 hours of incubation, 10 µl of MTT reagent was added to each well and was incubated for 4 hours. After that, 100µl solubilizing solution was added and waited till the color change and plate was read immediately in a microplate reader (BIO-RAD microplate reader). Well, with cell medium used as blanks and untreated cells were used as control.

2.3.5 Cell culture

The lung cancer cells (H69), pancreatic cancer cells (ASPC-1), and nano-cancerous fibroblast cells (NIH3T3) (ATCC, American Type Culture Collection) were used to study the DNA conformational changes. ASPC-1 were cultured in a T25 flask with RPMI 1640 with 10% FBS, 1% antibiotic and antimycotic solution. H69 cells were cultured in a T25 culture with Roswell Park Memorial Institutes (RPMI) 1640, 20% Fetal Bovine Serum (FBS), 1% antibiotic, and antimycotic solution (complete growth medium). NIH3T3 cells were cultured with Dulbecco's Modified Eagle's Medium (DMEM) with 10% FBS, 1% antibiotic, and antimycotic solution. The flasks were maintained in a sterile incubator with 5% CO_2.

2.3.6 XPS analysis of Au and Na$^+$ inside the cells

The cancerous and non-cancerous cells were c with the physically synthesized gold quantum particles for 24 hours. The samples were air-dried and analyzed with XPS for sodium and gold composition and the physical state of a gold element.

2.3.7 Gel electrophoresis

Genomic DNA was isolated from the treated and untreated cells as per the instruction from Bio Vision. Gel electrophoresis was performed by using 1.5% of agarose gel in Tris base, acetic acid, and EDTA buffer (TAE buffer) at 20 volts for 90 mins. The genomic DNA was mixed with the loading dye. The treated and untreated genomic DNA samples were loaded in the wells.

2.3.8 UV absorbance analysis

UV absorbance measurements were carried out using by using NanoDrop with a 2 µl isolated genomic DNA at 260 nm.

2.3.9 Fluorescence analysis of DNA by using Hoechst stain

Cancerous and non-cancerous cells were seeded at 3 X 10^5 cells per well, in six-well plates, following the incubation with synthesized gold quantum particles. The cells were incubated at 5% CO_2, 37°C for 24 hours. The cell was stained with the Hoechst stain, according to the Thermo fisher. Hoechst stain is specific, H-stains binds with the condense chromatins (intact DNA).

2.4 Results and Discussion

This section explains the detailed analysis of the results achieved from the experiments performed.

2.4.1 Synthesis and material chemistry of gold quantum particles

The unique quantum plasmonic quantum particles were synthesized by a physical method using a tunable Yb diode-pumped fiber laser having a central wavelength of 1030 nm under atmospheric nitrogen conditions. The femtosecond laser causes a high temperature which generates the ionic plume when the laser beam strikes the gold-coated silicon wafer. The generated plume consists of Au^+ and Si^+ ions, interacted with the N_2 in the nitrogen atmosphere and formed the intricate gold and silicon structures showed in Supplementary Figure 2.1. Gold quantum particles condense before silicon because of the different ionization threshold. The ionization temperature rapidly fluctuates creating moments of higher and relatively lower temperatures. At higher ionization temperature the Au^+ and Si^+ ions when interacting are more likely to arrange themselves in an amorphous and polycrystalline structure. These gold quantum particles coalesce and aggregate to form the structures which are arranged in a manner where silicon acts as cargo for the delivery of plasmonic quantum particles showed in Figure 2.1.

Earlier nanolithography or wet chemical synthesis was used for the synthesis of nanoparticles which require the presence of different chemicals and results in non-biocompatible and toxic particles with chemical contamination. However, by using laser synthesis (physical method) new material was created directly from the target free from chemical residues.

Physical analysis of gold quantum particles was established by using High-Resolution Transmission Electron Microscope (HRTEM), Scanning Electron Microscope (SEM) and Field

Emission Scanning Electron Microscope (FESEM). The size of the synthesized quantum particles at a nitrogen-filled atmosphere was observed and analyzed to have a broader size distribution curve of synthesized quantum particles as can be seen in Figure 2.1. Based on this observation the synthesized quantum particles were characterized as small gold quantum particles. The increase in the laser ionization energy results in a decrease in the size of the plasmonic quantum particles. Higher laser ionizations cause higher plasma temperature which results in a breakdown of plasmonic quantum particles into a smaller probe size shown in Figure

2.1. The HRTEM images in Figure 2.1 show the spherical morphology of the gold quantum particles. In addition to this for the present study the gold quantum particles of 2.01 nm were used because of the extremely small size. Furthermore to determine the material chemistry Energy Dispersive X-ray (EDX), X-ray photoelectron spectroscopy (XPS) and X-ray diffraction (XRD) were used. EDX studied the relative proportion of silicon, gold, oxygen and carbon. By fine-tuning the laser ionization gold concentration was controlled to 45%. Moreover XPS spectra analysis shows that the synthesized gold quantum particles peaks at binding energies ~84 eV and 88 eV corresponding to the purest form of gold [37]. Adding to this, the XRD spectra of physically synthesized gold particles show two major diffraction peaks for gold which can be indexed to the (111) and (222) reflections of face cubic structure of metallic gold. This reveals that the synthesized gold particles are composed of pure crystalline gold. The peaks correspond to (111) is more prominent than others, suggesting that (111) is the dominant orientation [38]
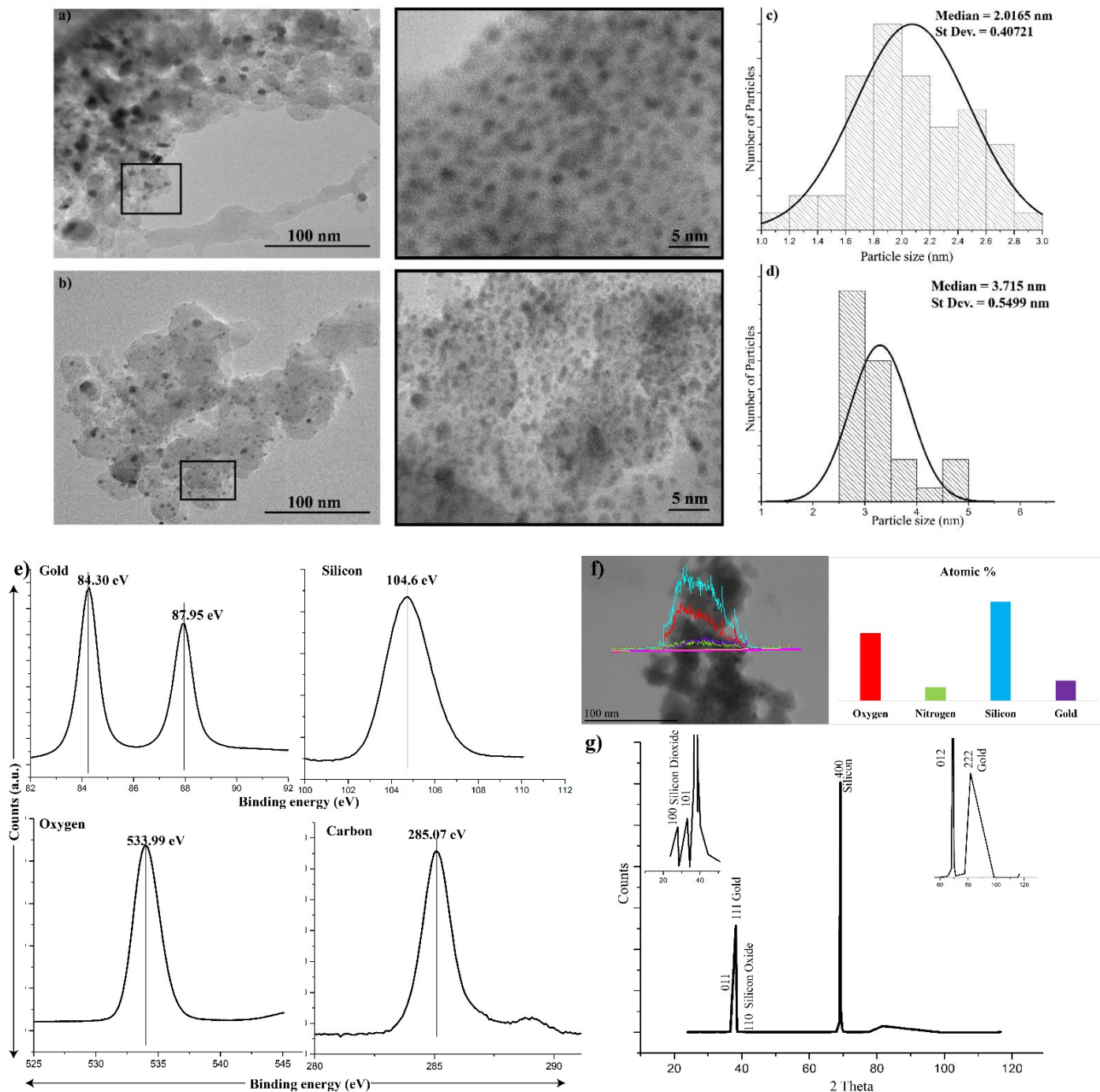
Figure 2.1 **Physically synthesized gold quantum particles characterization** a) and b) HRTEM images of 2.01 nm and 3.72 nm gold quantum particles respectively and c) and d) Size distribution of gold quantum particles as assessed by HRTEM images e) XPS analysis of physically synthesized gold quantum particles, f) Elemental composition of physically synthesized particles g) XRD analysis of different gold phases

2.4.2 Stability analysis of synthesized gold quantum particles

Previous studies have shown that chemically synthesized gold quantum particles have free chemical groups attached to the surface of gold nano quantum particles. The presence of free chemical groups allows the gold probe to bind with the protein molecules present in the cellular environment and will enable the formation of protein corona [39]. The composition of protein corona increases the biocompatibility of gold quantum particles. However, the presence of protein can critically affect the direct interaction of nanoparticles and cellular components [17]. Adding to this, the formation of protein corona affects the biomedical applications or modulate the nano-toxicological effects, including ecotoxicology [40], [41]. Therefore, in the development of gold nanoparticles for nanomedicine, it is essential to determine the presence of protein corona on the surface of gold nanoparticles.

To understand the stability and formation of protein corona on the surface of physically synthesized gold nanoparticles, two different environments, complete growth medium (CGM) with 10% fetal bovine serum (FBS) and phosphate saline buffer (PBS) were used. Synthesized gold nano-quantum particles were treated for 24 hours with the CGM and PBS. To study the physical properties of gold nano quantum particles, here the HRTEM images were studied, and the hydrodynamic size of the treated gold nano quantum particles was calculated. HRTEM images in Figure 2.2 show that the treated gold nano quantum particles remain the same size as untreated gold nano quantum particles (~2 nm). The piratical distribution curve measured the hydrodynamic diameter of a gold nanoprobe (Figure 2.2). The HRTEM images and the calculated particle size distribution curve of treated gold nano quantum particles show that the gold quantum particles are stable and retain their hydrodynamic diameter in CGM and PBS. Besides, HRTEM images also show that the synthesized gold quantum particles do not form the

layer of the protein corona, which helps to maintain the quantum size of the gold quantum particles and initiates the cellular uptake of gold quantum particles inside the cells.

Further, to analyze the chemical properties of treated gold quantum particles in different environments, XPS data were analyzed. The XPS results show that the presence of PBS and CGM does not affect the chemical stability of gold particles. Figure 2.2 shows that the binding energy of the treated and untreated gold quantum particles remains almost the same at 83.98 eV. This indicates that PBS and CGM do not affect the elementary composition of gold quantum particles.
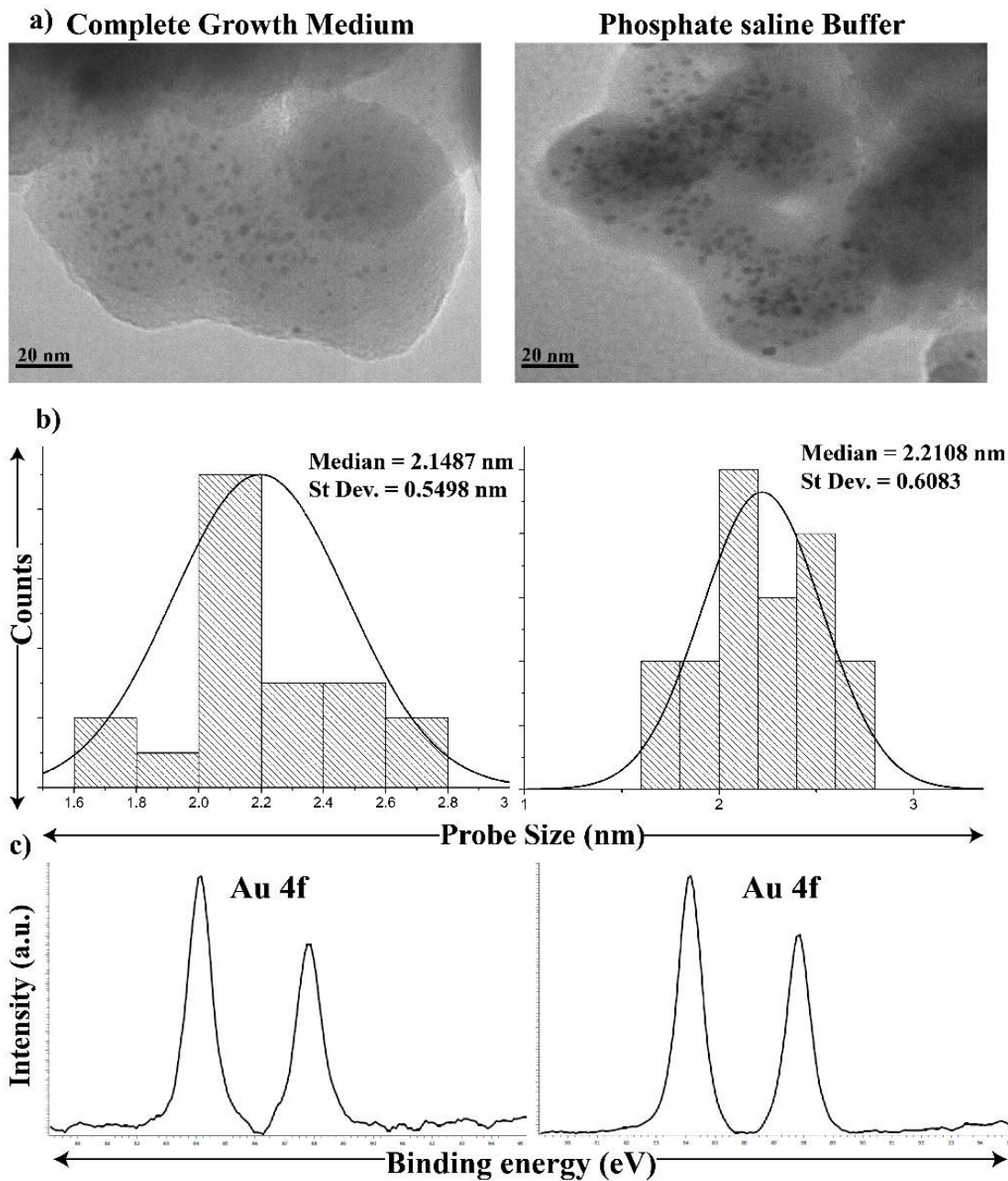
Figure 2.2 **Stability of physically synthesized gold quantum particles after treating with the complete growth medium and Phosphate buffer saline**. a) HRTEM images of 2.148 nm and 2.21 nm gold quantum particles treated with CMG and PBS respectively, b) Size distribution of treated gold quantum particles as assessed by HRTEM, c) XPS analysis of treated gold quantum particles.

2.4.3 Nuclear internalization and cellular toxicity analysis of gold quantum particles

The nucleus maintains the uprightness of genes and the cellular activity by gene expression. The nucleus has a nuclear envelope, which consists of a double lipid bilayer, the nucleus lumina and the nucleolus. The nucleus lumina consist of intermediate filaments and membrane-associated proteins. The chromosome consists of DNA and histones and the nucleolus consists of coding rRNA, rDNA, and proteins [12]. Since the nuclear envelope keeps most of the macromolecules and prevents many different components from entering the nucleus, particle entry into the nucleus is minimal unless the particles are extremely small (<5 nm) or engineered with nuclear target molecules [42]–[44]. Researchers used coatings and biocompatible layers to overcome the cytotoxic nature of chemically synthesized gold nanoparticles [45]. The added biocompatible coating on the surface of gold nanoparticles increases the overall dynamic size which increases the difficulty of internalization of gold nanoparticles inside the cells particularly inside the nucleus [17]. Most recent studies have shown that unmodified QDs (3.2 nm) can penetrate inside the nucleus, accumulate in the nucleus, and exhibit strong affinity to core histones and histone abundant cell organelles [43]. However, the accumulation of QDs inside the cells causes the decompensation of the nuclear chromatins in the mouse sperm causing potential spermatotoxicity [18]. Gold nanoparticles and DNA interactions majorly drive such effects. The interaction between gold nanoparticles and DNA strands are primarily driven by electrostatic interactions [46], [47] with CTAB and MTAB on the surface of chemically synthesized gold nanoparticles forming a strong covalent bond between the DNA. Usually, this interaction happens in 3 steps: a) the first step is the formation of an external adduct, b) the formation of DNA-gold particle complex based on the binding affinity of gold particles and c) the last step is the formation of a more compact DNA-gold nanoparticle complex which results in DNA

conformational changes [48], [49]. This generates the requirement to synthesize the gold particles which can penetrate the nuclear envelope and adhere to nuclear components with loose bindings so that it enhances the single without causing any conformational changes to the secondary DNA structure.

Non-destructive interaction of DNA and gold nanoparticles is a prerequisite for the accurate study of DNA conformation. The gold nanoparticles must penetrate through the plasma membrane and the double-membrane nuclear envelope to reach DNA. Presently synthesized gold quantum particles retain their quantum size as they are synthesized by using the physical synthesis method which eliminates the chemical residues. Because of the unique size of the physically synthesized gold quantum particles (2.01 nm), they can easily penetrate inside the plasma membrane and the double-membrane nuclear envelope. The average number of quantum particles inside the nucleus is 123. Figure 2.3 shows the formation of vacuoles (caring for the gold quantum particles) inside the cells. The presence of vacuoles and bending of the cell membrane indicates the endocytosis mechanism. From Figure 2.3, it was hypothesized that the uptake of the gold quantum particles is mediated by the conventional adsorption of protein on the surface of gold quantum particles. These proteins help the gold quantum particles to enter inside the cell membrane via endocytosis. However, the presence of these proteins does not affect the morphology and the chemical stability of the synthesized gold quantum particles as discussed in the previous section.

Probing further, the toxicity profile of physically synthesized gold quantum particles inside the ASPC-1, H69, and NIH3T3 cells were evaluated. Here MTT assay was studied to analyze the toxicity of gold quantum particles. All the three different types of cells were treated with the gold quantum particles for 24 hours. The toxicity profiles include the gold quantum particles, cell

culturing medium, and untreated cells as control. No changes were observed in the cell viability of the three cell lines on the exposure to gold quantum particles (Figure 2.3 e)). There was no observable toxicity associated with gold quantum particles according to the MTT data.

The reduction or absence in toxicity associated with the gold quantum particles is due to the physical synthesis of gold quantum particles where there are no chemical residues and chemical layers present on the gold quantum particles. Physical synthesis allows the gold quantum particles to retain the properties of biocompatible gold without the need of an external layer.

To study the presence of gold quantum particles inside the cell nucleus, the Mass spectrometry analysis was performed of the cells. Mass spectrometry monitors the localization of gold particles inside the ASPC-1, H69, and NIH3T3 cells. The existence of gold signals in the cells was observed which were enriched with gold particles, and more importantly, the presence of gold particles within the ASPC-1 and H69 were higher as compared to NIH3T3 cells. It corresponds to the BioTEM data generated Figure 2.3.
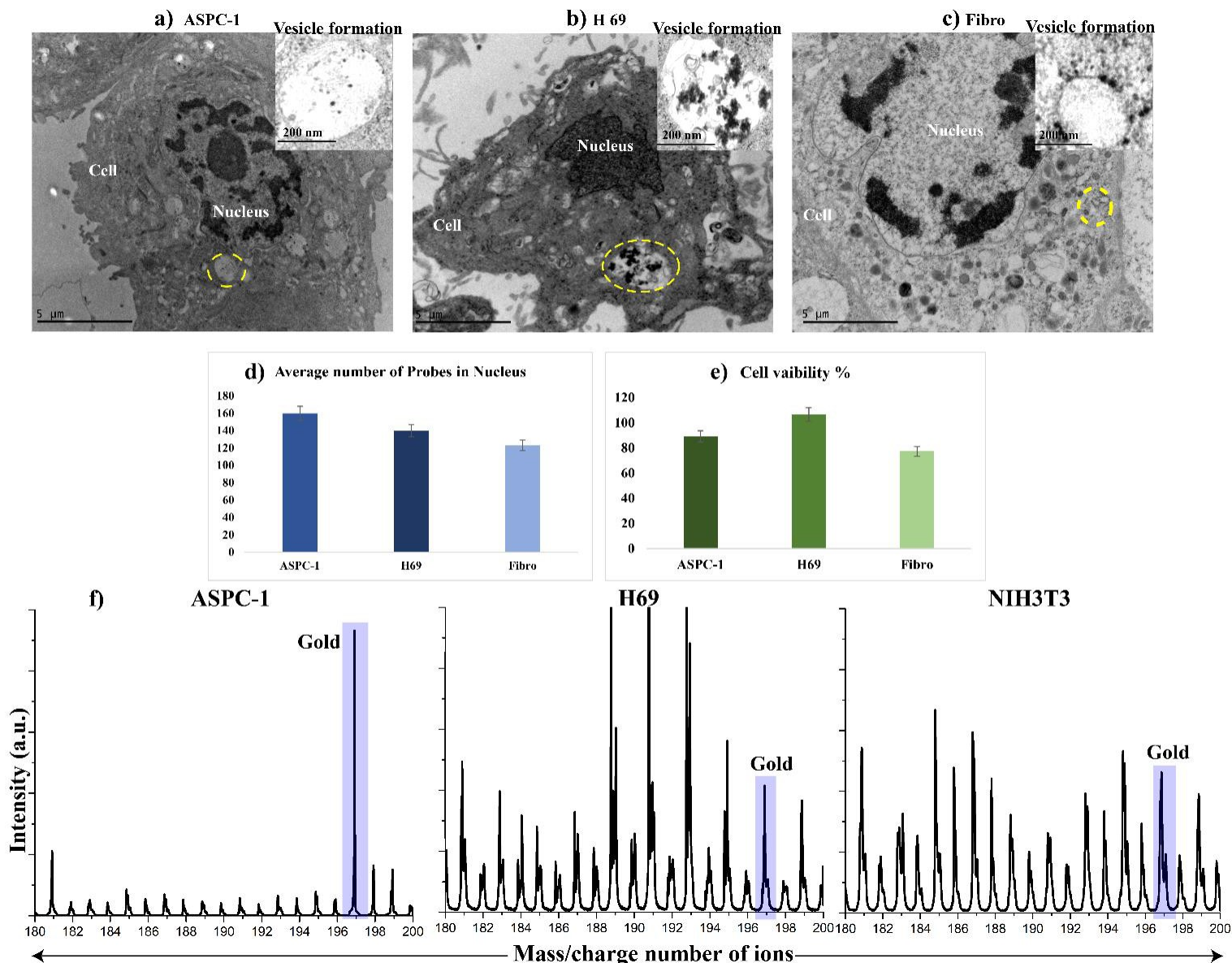
Figure 2.3 **Non-toxic gold quantum particles are localized in intracellular vesicles following endocytosis**. a-c) BioTEM images of gold quantum particles internalizes in H69, Fibro, and ASPC-1. Insets, Regions of vesical formation in the cells and the nuclear uptake of gold quantum particles indicated by the yellow dashed circles d) the graph to show the average number of quantum particles present inside the nucleus of each cells e) Physically synthesized gold quantum particles are non-toxic. Live/dead cell viability assays on ASPC-1, H69 and fibro (n=5 per condition) cells treated with gold quantum particles for 48 hours. One-way analysis variance

(ANOVA) was performed ($p<0.05$). f) Mass spectrometry element signals of ASPC-1, H69 and NIH3T3 cells treated with gold quantum particles.

Previous researches show that gold particles localized within the cytoplasmic vesicles even with no nuclear localization. Even without entering the nucleus they can still alter the gene expressions and DNA binding proteins [9]. It was observed that native gold nano-rods before the treatment of cells have an Au (0) state. However, after treating the GNRs to cell culture media and the following internalization in cells, the binding energy increases by ~1.2eV which is consistent with the presence of Au (I). The formation of the stable Au (I) oxidation state is due to intracellular redox conditions coupled with the presence of stabilizing biomolecules. Adding to this, the changes in the concentration of Na^+ can also directly impact the stability of the DNA structure. As the DNAs are negatively charged, Na^+ ions stabilize the DNA structure and the fluctuation in Na^+ ions affect the stability of the DNA structure. In the following sections experimental results were performed to demonstrate that the physically synthesized gold quantum particles do not cause any conformational changes in the secondary DNA structure in the cellular environment.

2.4.4 Effect of Na^+ concentrations inside the cells

Nucleic acid molecules are highly charged poly-anions. In the compact formation of nucleic acids, the cations such as sodium and magnesium ions are required to counterbalance the negative charges on the backbones to decrease the repulsive Coulombic interactions among the phosphates, to the DNA biomolecules can fold into condensed natural structures. The formation of a stable DNA structure can significantly become weaker as the salt concentration (Na^+) increases. The presence of salt affects the binding affinity of the DNA and with the increased salt concentration, the binding affinity of DNA increases. The amount of Na^+ ions

thermodynamically bound to DNA results in DNA strand extension [50], [51]. The secondary structure of a random sequence single DNA strand is strongly dependent on the counter-ion concentration (Na). The change in structure can significantly affect ligand ssDNA interactions. DNA binding affinity with ligands generally becomes weaker as the salt concentration increases. The slope of this plot has been read as representing the number of Na+ ions thermodynamically bound to DNA that is released per ligand-bound [52]. The ion release occurs as a result of ion- pair formation in the case of cationic ligands and also as a result of DNA strand extension in the case of inter collators [53].

Previous researches show the fluctuation in the concentration of Na^+ ions inside the cells treated with chemical synthesized gold nanorods. The localization of gold nano-rods within the cells alters the DNA conformations. A significant change was seen in the concentration of Na^+, which shows the indeed deregulations of the cellular electrophysiology. Earlier studies showed that the concentration of Na^+ was undeniably higher in the treated cells when compared to the control cells [9].

In the present study, the physically synthesized gold quantum particles have the unique ability to penetrate inside the nucleus without the need of labeling which helps to study the effect of gold quantum particles on DNA conformation which has not been explored because very few studies were able to deliver particles inside the nucleus. Here XPS analysis was performed of the whole cells (ASPC-1, H69, and NIH3T3) following exposure to the synthesized gold quantum particles. XPS analysis demonstrates the localization of quantum particles within the cells. As evidenced by the measurable sodium (Na^+) concentration within the treated cells remain the same as compared to the untreated control cells, shown in Figure 2.4. The graphs presented in Figure 2.4 show the XPS generated peak for Na^+ at 1071.68 eV which remains the same for treated cells

and untreated control cells. XPS analysis of whole Fibro, ASPC-1 and H69 cells following the exposure to the gold quantum particles demonstrated that the localization of gold quantum particles within the cells does not deregulate the cells' electrophysiology as evidenced by the same concentration of sodium within the cells Figure 2.4. The same analysis was repeated with the other two cancer types (Lung cancer and pancreatic cancer). Similar results were observed and localization of gold quantum particles inside the nucleus does not change the sodium concentration.
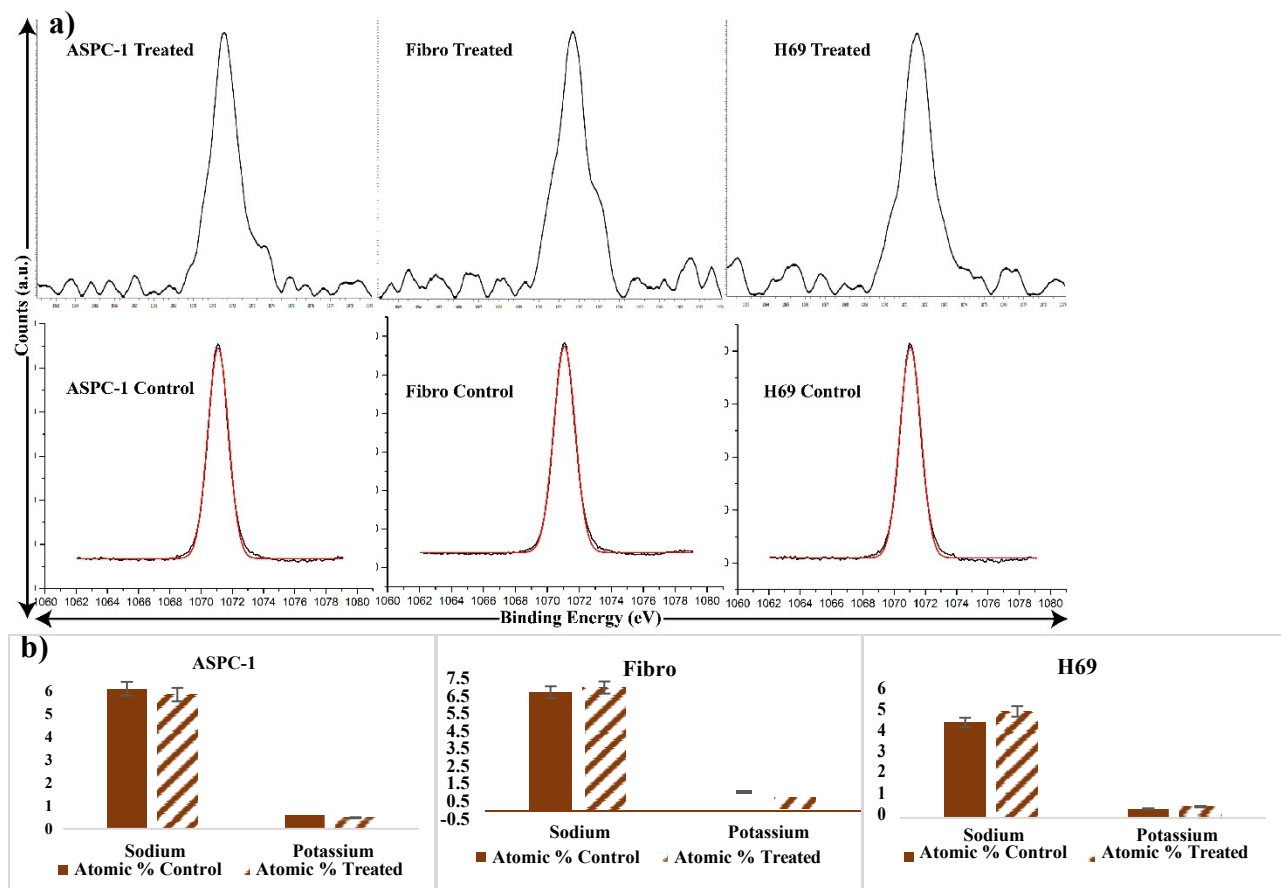
Figure 2.4 **Studying the stability of the genomic DNA structure by monitoring the sodium and potassium concentration in treated and untreated cells**. a) X-ray photoelectron spectrum of the sodium region of treated ASPC-1, H69 and fibro cells and the corresponding spectra of

control cells for reference b) Elemental composition of sodium and potassium in ASPC-1, H69, and Fibro cells proportion, as assessed by XPS

2.4.5 Studying changes in Au state inside the cells

Figure 2.5 compares the gold state before and after the internalization of gold quantum particles inside the cells. The significant peaks with the Au 4f spin-orbit centered at 84 eV correspond to Au (o), and the other major peak positioned at 87.6 eV. There is a ~0.1 eV shift in the peaks following the cell internalization for all three cell lines and the shift might be caused by weak bonding between the gold quantum particles and DNA. According to the previous study the binding energy of pure gold can vary up to ~ 0.4eV [54]. Adding to this deconvoluted the generated peak were presented to determine the presence of different chemical states of gold quantum particles inside the cells. So as evidenced by the deconvolution (Supplementary Figure 2), Au 4f spectra do not show the presence of any different chemical state of gold quantum particles following the exposure of gold quantum particles to the cell culture media and following the internalization in the cells as well as the nucleus.

XPS analysis shows that gold does not change chemically after cell internalization which contradicts previous studies [9]. Generally, in an extracellular environment chemically synthesized Au (III) particles are most stable in Au (I) or Au (0) state due to the intracellular redox conditions coupled with the stabilizing biomolecules and result in the formation of Au (I) oxidative [55]. The gold used for this study however was not oxides therefore does not affect the intracellular redox reactions resulting in no change in the DNA structure. This result shows that gold did not change its chemical state after cell internalization and as a result does not cause any change in the conformational dynamics of DNA secondary structure.
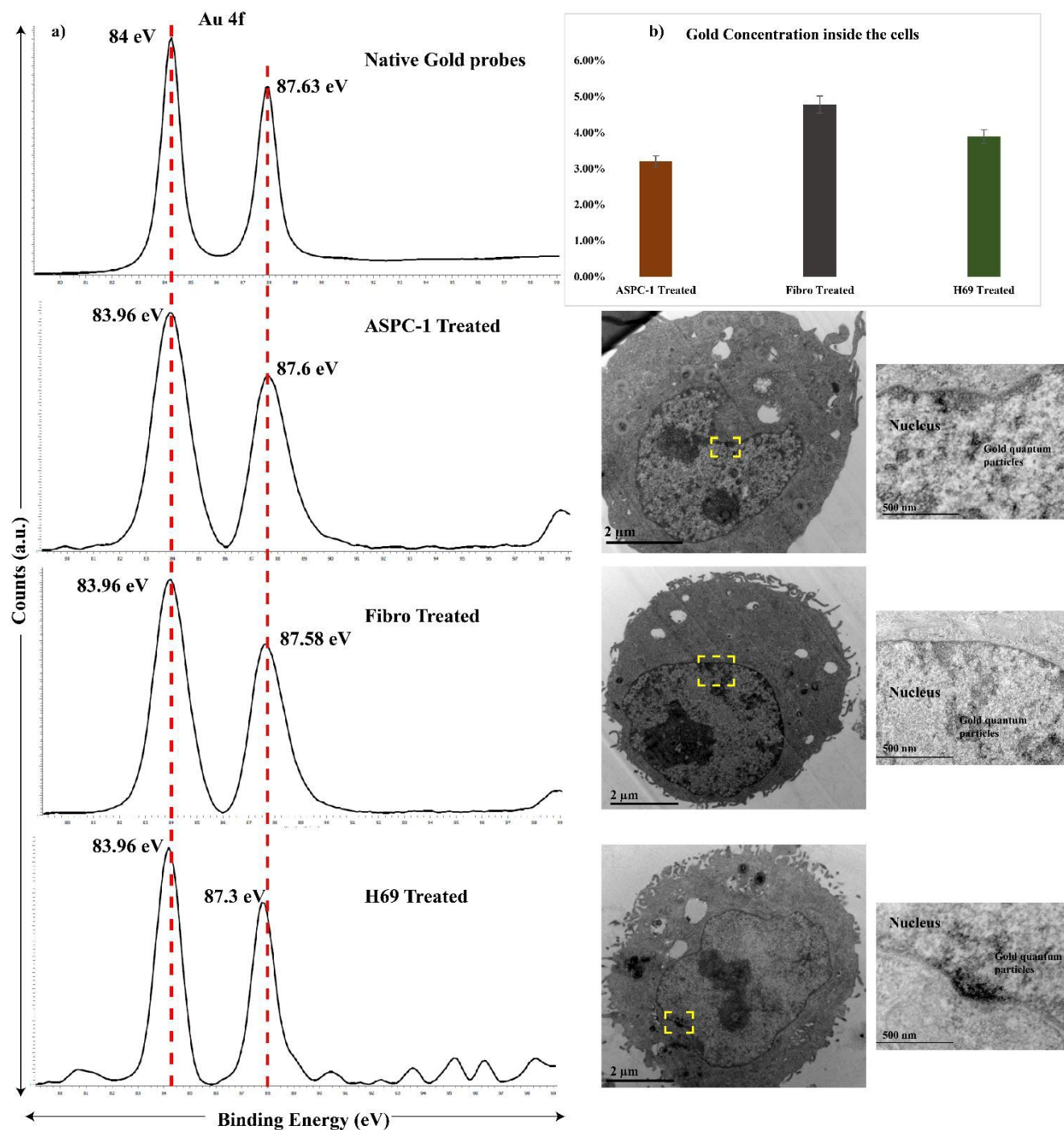
Figure 2.5 **Monitoring the chemical state of native gold quantum particles after localizing inside the cells**. a) X-ray photoelectron spectrum of Au 4f electron region of physically synthesized gold quantum particles-treated ASPC-1, H69, and Fibro cells and the corresponding

spectra of gold quantum particles only samples for reference, b) Elemental composition of ASPC-1, H69 and fibro cells by proportion, as assessed by XPS.

2.4.6 Structural analysis of Genomic DNA

To validate that the physically synthesized gold quantum particles do not cause any conformational changes in the DNA secondary structure the structure of genomic DNA isolated from treated and untreated cells were analyzed.

Gel electrophoresis was performed by using 1.5% agarose in TAE buffer for solutions with different cell types (Figure 2.6). The gel electrophoresis shows the appearance of intact genomic DNA strands (Figure 2.6). The treated cells do not show a discrete change in the structure of genomic DNA. The DNA bands remained closed to the well which is the result of the intactness of DNA. Moreover, the DNA bands of treated and untreated cells appear similar. This showed that the structure of genomic DNA remained intact and unchanged after the treatment with gold quantum particles.

Further, to elucidate the details of the DNA structure the UV spectra were analyzed. UV absorbance is conventionally used to determine the concentration of isolated DNA. It can also be used to identify structural changes in the DNA strand with the help of a hyperchromic shift [56] upon the change in structure. Succeeding this UV absorbance was initially used to quantify the genomic DNA concentration and then determine if there is any change in DNA strands (Figure 2.6). Comparing the control DNA (black curve Figure 6) to the treated DNA (red curve Figure 2.6), there was no significant hyperchromic shift in the treated cells. Thus the absorbance of DNA at 260 nm indicates that DNA-gold quantum particles complex possess no structural changes.

a) Genomic DNA structural analysis by Gel electrophoresis

Lane 1	DNA Ladder
Lane 2	ASPC-1 Control
Lane 3	ASPC-1 Treated
Lane 4	H69 Control
Lane 5	H69 Treated
Lane 6	Fibro Control
Lane 7	Fibro Treated

b) Genomic DNA structural analysis by UV-vis
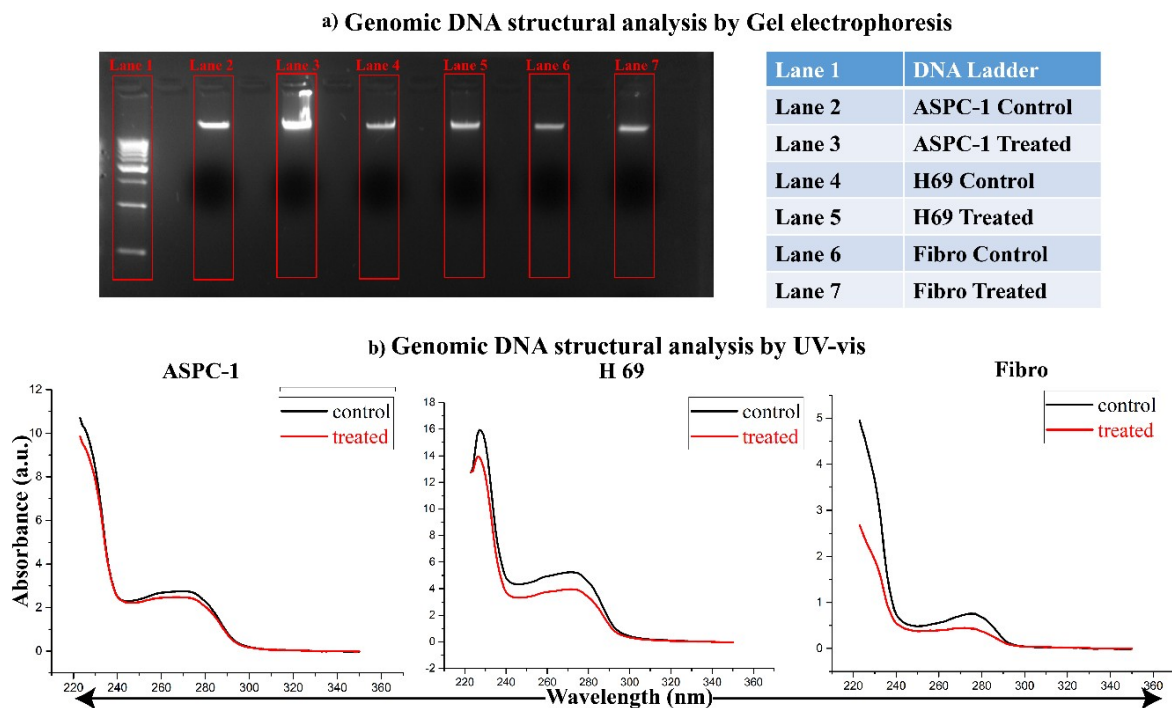
Figure 2.6 **Intact genomic DNA in the nucleus, observed following the gold probe internalization in the cells as well as the nucleus** a) structural analysis of genomic DNA by using gel electrophoresis b) UV absorbance spectrum

2.4.7 Intact genomic DNA study by Hoechst Fluorescence

To determine whether exposure of cells to gold quantum particles results in no structural alterations in the genomic DNA the intactness of DNA in the nucleus was evaluated inside the cells exposed to the sub-one nanometer plasmonic quantum particles and then compared treated and untreated cells. Quantitative visualization of genomic DNA was conducted via fluorescence microscopy with a genomic DNA specific dye. There was no substantial difference in DNA fluorescence intensity that was observed when compared to controls. This confirms that the

physically synthesized gold quantum particles do not cause changes in the secondary DNA conformation.
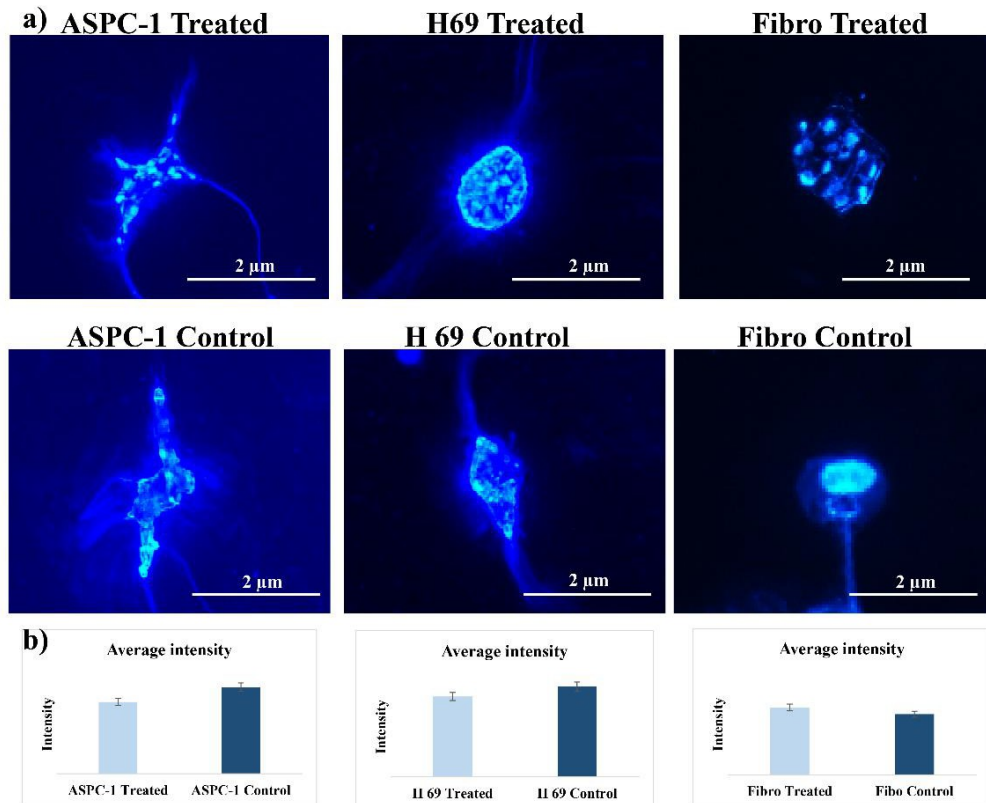
Figure 2.7 **Visualization of condensed DNA in the cell, following gold quantum particles internalization in the cells**. a) Visualization of intact chromosome in ASPC-1, H69 and Fibro cells (treated and control cells respectively) b) Quantification of average fluorescence intensity generated by treated and control cells.

2.5 Conclusion

This study positively demonstrated that physically synthesized native gold quantum particles do not alter the secondary structure of genomic DNA. Now using ultrafast laser gold quantum particles was synthesized without chemical contamination. These gold quantum particles were 2nm in diameter and exhibited non-cytotoxic behavior in the intracellular environment. The genomic DNA conformational analysis was done with three different cell types namely lung cancer (H69), pancreatic cancer (ASPC-1) and healthy fibroblast cells (NIH 3T3). The native gold quantum particles localized inside the cells and the nucleus by the endocytosis uptake phenomenon. They do not undergo a chemical oxidation reaction and retains their native chemical state (Au (0)). This indicates that the gold ions and the cellular and nuclear components bind through low-affinity bonds which do not induce conformational changes in the genomic DNA structure. Adding to that the native gold quantum particles do not perturb the ionic balance (sodium concentration) inside the cells which is known to affect the stability of the genomic DNA structure directly.

Furthermore, visualization analysis of genomic DNA by gel electrophoresis and fluorescence analysis show that the secondary structure of DNA remains intact. Results surmise that the nuclear localization of gold quantum particles does not cause changes in the intracellular environment. This study successfully overcomes the stumbling block for the DNA conformational changes induced by gold-based nanomaterials.

Chapter 3

Cancer Signaling by Plasmonic quantum Probes

3.1 Abstract

Although the use of gold quantum dots for non-cellular sensing is overgrowing the use of quantum gold dots are still limited because of comparatively large overall size (biocompatible layer) overlapped Raman readout of lower concentrated metabolites inside the cells and dispersion of QDs inside the cancer cells. This is due to the labeling of QDs which results in specific binding and non-uniform distribution of QDs inside the cells. Besides this QDs are toxic due to the presence of chemical residues from the wet synthesis hampering its rendition to clinical application. To increase biocompatibility and surge the cellular uptake gold probes are usually layered with bio-films (PEG). However, layering impedes the interaction of metabolites and gold QDs and damps the surface plasmonic resonance resulting in a low Raman signal. The addition of biofilm increases the overall hydrodynamic size of gold QDs limiting the dispersion and internalization of plasmonic QDs inside the cell as well as the nucleus. Therefore, the unique properties that arise from the quantum size of the plasmonic probe are lost. To retain the quantum size of QDs there is a need to use a physical method of synthesis and use gold QDs layering free. In this research manuscript the quantum sized layering free Plasmonic Quantum Probes (PQPs) are introduced a potential tool for cancer sensing which provides the opportunity to attain the sensing of surface oncoprotein, intracellular oncoprotein and nuclear metabolites simultaneously. This work introduces the concept of Plasmonic Quantum Probes (PQPs) for intercellular sensing. It was the first time the probe close to the size of cellular metabolites was

synthesized. By using physical synthesis (multiphoton laser ionization) biocompatible PQPs were synthesized without chemical adulteration and eliminated the need for biocompatible layering. Since the PQPs are non-toxic no layering is required enabling the study of the exact quantum effect in plasmonic cellular signaling. The naked PQPs demonstrated self-cellular uptake with even dispersion and non-specific attachment to all the cell components. As a result the Raman spectra revealed rich information of multiple cell components including surface (e.g., EGFR), intracellular (e.g., HPV E6/HPV E7) and nuclear metabolites (e.g., DNA/RNA) simultaneously in one single Raman profile. Due to the difference in the number of probes inside the cells the signal strength of cancerous cells is significantly higher than that of fibroblast cells implying that the differentiation of cancerous cells is possible through the analysis of the intensity of Raman readout. The probe size is found to be inversely related to the signal strength of the plasmonic readout. The PQP provides a holistic picture of cell states and may open up new possibilities for accurate diagnosis of cancer.

3.2 Introduction

In recent years, the use of RAMAN based plasmonic signaling of individual mutated metabolites has gained significant attention in cancer signaling [19], [20], [57]–[64]. Plasmonic sensing is usually achieved by two different methods direct and indirect methods. Direct plasmonic sensing is the most upfront method of sensing metabolites as sensing is done by directly acquiring the RAMAN signals for the required metabolite without the need of RAMAN reporters or molecule sensors [65]–[73]. However, current research is limited to the sensing of single mutated metabolites such as amino acids, proteins, biomarker and receptors in the non-cellular environment[62], [63], [74]–[77]. Cellular signaling of metabolites is essential because mutated metabolites in cellular conditions behave differently from metabolites in non-cellular conditions

providing more exciting new possibilities diagnosis and therapy. Research shows that probe cytotoxicity, cellular uptake, navigation of probes to the nucleus, the proximity of the probe to metabolites, reliable spectra, reproducibility, and retaining the Raman sensitivity inside the cells is the cornerstone for the direct intracellular sensing [45], [78].

In order to increase the uptake and reduce the cytotoxicity of plasmonic probes, researchers started using the indirect method for plasmonic sensing where plasmonic probes are labeled or layered with biocompatible materials (bio-films) such as Polyethylene glycol (PEG). It is used to coat the plasmonic materials to bind specific proteins, cellular components, and up- taken by the specific pathway [79]–[81]. The significant challenges of using biocompatible layers include the layering of a biocompatible material controlling the location of particles, uptake pathways and destination of particles which restricts the Raman signal readout. Adding to that Raman signal readout is enhanced only in the close vicinity roughly up to 10 nm the encapsulation of particles with bio-films generates the range of the evanescent field on the surface of probes leading to the decrease in the formation of hot spots and results in low signal enhancement [82]. Raman signal enhancement is based on the interaction of the plasmonic material and the metabolites which generate resonant excitation of a charge transfer between metabolites and plasmonic probes. Layering hinders the interactions resulting in reduced signal sensitivity and intensity[62] leading to the noise and overlap of signals which prevent the signaling of single metabolites[24], [64], [83].

The measurement of the single mutated metabolite is usually insufficient for cancer cellular diagnosis. Some cancer metabolites like carcinoembryonic antigen (CEA), ferritin, carbohydrate antigen (CA) and CA125 are linked with lung, breast, pancreatic and other cancer types[84], [85]. This means there are more possibilities for what the diagnosis could be. If the

intracellular metabolites and the mutated markers associated with the cancer cells are identified this situation is eluded leading to more accurate results. For instance the study of mutation occurred in the nucleic acids and specific proteins such as mutations in Estrogen and HER2 receptors used to diagnose breast cancer while mutations in the HPV E6 and HPV E7 are used for cervical cancer diagnosis [86]–[90].

Besides the layering of biocompatible materials also increases the overall hydrodynamic size of the plasmonic probes which leads to aggregation by forming the protein corona and limiting the dispersion and internalization of probes inside the nucleus[58], [91]. The particle size of plasmonic material has a significant influence on the cellular/nuclear uptake and dispersion inside the cell. To facilitate the navigation and dispersion of plasmonic probes inside the cells without aggregation researchers began to use gold quantum dots (QDs). Due to their small size QDs can penetrate the cells as well as the nucleus when compared to nanoparticles[91]. Gold QDs have shown size-dependent penetration within a biological system, especially with respect to cellular and nuclear uptake[10], [26], [92]–[96]. For instance brain microvasculature permeation of QDs shows that 4nm core size led to the optimum result. The transport and kinetic profile of 4 nm gold core are substantially different from those of its large- sized (>15nm) counterparts[97]. Gold quantum dots usually more readily cross barriers[92]. It is particularly true for small gold quantum dots.

Adding to the above-mentioned biological properties gold quantum dots have better optoelectrical properties and high surface area when compared to large ones due to the quantum confinement effect. Due to its small size QDs show the increased plasmonic nature leading to molecular level detection with accuracy, unprecedented sensitivity and more reliable signals which make it more suitable for intracellular SERS cancer signaling.

Gold quantum dots offer exceptional opportunities in intracellular cancer signaling. However, the toxicity induced by the chemical synthesis of QDs hampers its application for intracellular sensing. QDs are mostly synthesized in a non-polar organic solvent and therefore have a hydrophobic surface. This hydrophobicity usually leads to irreversible aggregation and instability in a cellular environment thus limiting their biological application. To improve the attributes of QDs they have been encapsulated with biocompatible materials in order to prevent aggregation and increase uptake and biocompatibility[98]. However, encapsulation increases the overall hydrodynamic size of QDs. Therefore, the unique properties that arise from quantum size are lost. By far reports on the cell signaling by exact quantum size are limited if any.

This work introduces gold plasmonic quantum probes (PQP) for the detection and monitoring of intracellular biochemistry through plasmonic readout. Here the probe size was close to the size of cellular metabolites which helps to increase cellular plasmonic sensitivity. Non-toxic quantum-size PQP were synthesized by laser-based physical means without chemical contamination which eliminates the need for labels and coatings. Intercellular detection was tested on three different cell lines namely breast cancer (MDA MB 231), cervical cancer (HeLa), and normal fibroblast (NIH 3T3). Due to the quantum size PQPs exhibit unique self- internalization through passive dispersion with anomalous dispersion all over the cell including the nucleus. Due to the unique dispersion of PQPs inside the cells a 1000-fold increase in the Raman readout of cells compared to the control were seen. Breast cancer and cervical cancer uptake at least six times more cells than normal fibroblasts (NIH 3T3) after 18 hours of cell seeding.

Consequently, the SERS signals from breast cancer and cervical cancer cells are higher than those from fibroblast cells. The naked PQPs demonstrated self-cellular uptake and

dispersion, enabling simultaneous plasmonic readout for surface (e.g., EGFR), intracellular (e.g., HPV E6/HPV E7) and nuclear metabolites (e.g., DNA/RNA). Signals generated by the multiple mutations and cellular metabolites are revealed on a single Raman profile. The complete information of a cell allows us to identify not only a cell but also monitor its healthy state.

3.3 Materials and Methods

The details of the experiment performed to achieve the objective-2 are explained in this section.

3.3.1 Physical synthesis of plasmonic quantum probes

To synthesize the PQPS, a diode-pumped, Yb-doped fiber amplifier, femtosecond laser system (Clark-MXR, Inc.; IMPULSE Series ultra-short pulse laser) was employed. The target materials were silicon wafers (100) with a thickness of 500 μm (University Wafers, USA) coated with gold (350 nm in thickness). An array of lines of varying spaces in between was a machine at pulse repetition of 8, 12, and 26 MHz in atmospheric condition. The speed at which the laser-irradiated was varied at 1 mm/sec, 0.5 mm/sec and 0.25 mm/sec.

The plasmonic probes were the result of the interaction of the femtosecond laser beam and the gold-silicon wafer due to laser ionization induced phase transformation. These multiple-phased PQPs consisted of different phases of gold, silicon dioxide and amorphous as well as crystalline silicon. In order to increase control over the composition of the quantum probes laser energy was fixed. In this experiment, the laser wavelength was set at 1030 nm laser power at 17 W and the pulse width at 214 fs. It was observed that when pulse repetition, speed, and cycles were varied the size and concentration of different phases of gold and amorphous silicon could be modified.

3.3.2 Material Characterization of PQPs

The morphological analysis of the fabricated multi-phase plasmonic probes was done by using a Scanning Electron Microscope (SEM) (Hitachi S 5200) and a Field Emission electron Microscope (FESEM). A High-Resolution Transmission Electron Microscope (HRTEM) revealed the presence of plasmonic quantum probes inside the silicon. To obtain the elemental concentration of synthesized gold, silicon, silicon dioxide and Energy Dispersive X-ray (EDX) was used. An X-ray Photo-electron Spectroscopy (XPS) was used to determine the chemical composition of different gold and silicon phases that were present in the multi-phase PQPs.

3.3.3 Stability analysis of synthesized PQPs

The PQPs were treated with two different solutions (Phosphate buffer saline (PBS) and cell-culturing medium) for 24 hours and HRTEM was used to determine the dynamic size of treated PQPS. To confirm the material chemistry and state of gold, X-ray photon spectroscopy was performed.

3.3.4 Cell Culture and seeding of cancerous and non-cancerous cell lines

The cancerous cell lines of cervical cancer (HeLa) and breast cancer (MDA-MB-231) (ATCC, American Type Culture Collection) and non-cancerous cell lines of Fibroblast (NIH3T3) were employed in the experiment to accomplish the comparative cell study. MDA-MB 231 and NIH3T3 cells were cultured in a T25 tissue culture flask with Dulbecco's Modified Eagle's Medium (DMEM), 10% fetal bovine serum and 1% antibiotic and antimycotic solution (complete growth medium). HeLa cells were also cultured in a T25 tissue culture flask with Modified Eagle's Medium (MEM), 10% FBS, and 1% antibiotic and antimycotic solution (complete growth

medium) and all the cells line were maintained at 37 °C in 5% CO_2. The cell lines were purchased from the ATCC cell lines.

3.3.5 SEM imaging and EDX analysis

The cells were observed by using the Scanning Electron Microscopy (Hitachi, SU-1500). For this the 3 million cells were seeded on the top of the PQPs for 18 hours. After that the medium was removed, and the cells were fixed with alcohol dehydration and critical freeze point drying process for SEM analysis. Images were acquired at a standard scale bar of 500 μm to 100 μm with an acceleration voltage of 3 kV and probe current of 60 to 70 µA. Adding to this to analyze the presence of PQPs inside the cells, EDX analysis was performed.

3.3.6 SERS sensing for detection of cancer

The cells were seeded on the top of the synthesized multi-phase plasmonic quantum probes by using a complete growth medium. The cells were seeded for 6 and 18 hours. By removing the medium the reaction was stopped followed by washing with Phosphate Saline buffer and fixating the cells by using 4% paraformaldehyde. Multiple cancer surface biomarkers were sensed by using the PQPs present in the plasmonic quantum probes at 6 hours and 18 hours.

3.4. Results and Discussion

This section explains the detailed analysis of the results achieved from the experiments performed.

3.4.1 Gold quantum probe synthesis and Characterization

The synthesis of quantum probes was done by a physical method using an in-house femtosecond pulsed laser with a central wavelength of 1030 nm. Upon irradiation onto the gold-coated silicon

target the laser beam causes electron heating by multiphoton absorption and ionized plasma forms as illustrated in Figure 3.1. The size of this plasma was proportional to the ionization energy of the laser beam. However, for the given pulse width the laser fluence decreased with increasing pulse frequency. When Au^+ and Si^+ ions interacted with the ionized ambient atmosphere it formed complex oxides of gold and silicon. Gold particles condensed before silicon because the ionization threshold of gold was 890.1 kJ/mol, which was higher than that of silicon which was 786.5 kJ/mol [99]. The high pulse frequency enables the newly formed particles to interconnect into the PQPs. These Quantum probes consisted of a heterogeneous composition of polycrystalline and amorphous quantum gold. The size, morphology and composition of gold and silicon could be altered by varying the laser parameters. Unlike nanolithography or wet chemical synthesis that made nanoparticles non-biocompatible and toxic laser synthesis creates new material directly from the bulk target free from chemical residues.
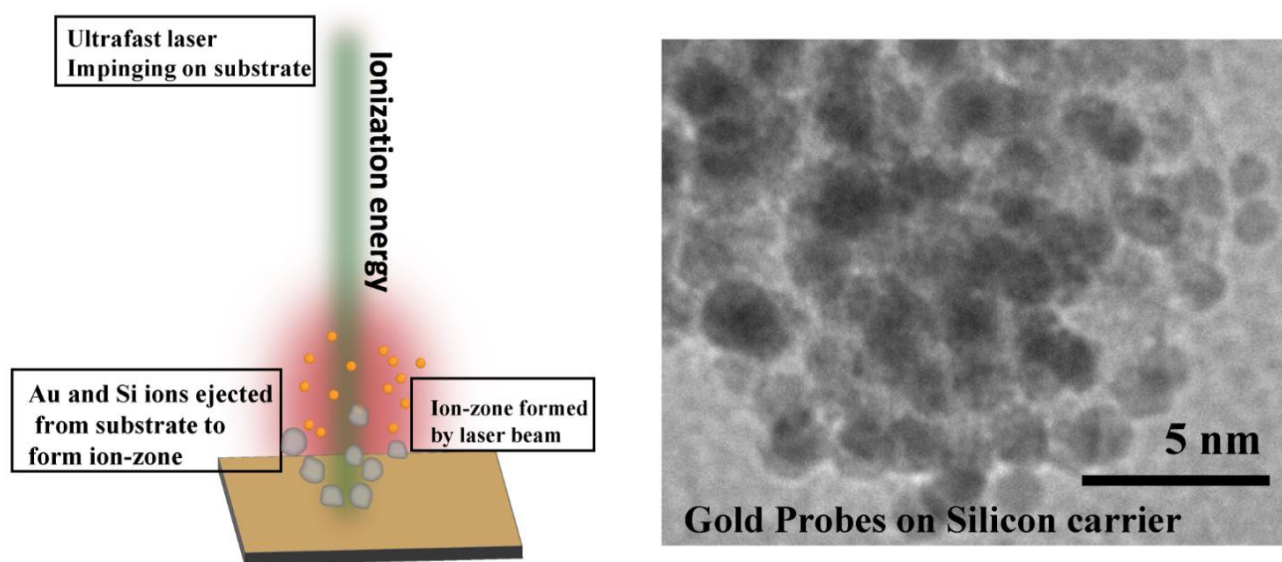
Figure 3.1 Schematic representation of Plasmonic quantum probe (PQPs) synthesis by forming an ion zone and HRTEM image of gold probes on a silicon carrier

Analysis of physical properties of PQPs was established by using a High-Resolution Transmission Electron Microscope (HRTEM), Scanning Electron Microscope (SEM), and Field Emission Scanning Electron Microscopy (FESEM). HRTEM images given in Figure 3.2 show that the PQPs was mostly hexagons and spheres. Figure 3.2 c and d depicts the particle size distribution measured with ImageJ software. The particle size of the PQPs varies from 5.74 nm, with SD ± 2.287 nm to 2.4 nm with SD ± 1.08 nm. Silicon carries are much more significant. The increase in laser ionization energy led to a decrease in the size of gold particles. When laser ionization energy is high, the plasma temperature increases, which leads to the breakdown of gold particles and results in smaller particle size (supporting information (SI)) Table 2). Whereas the particle size of silicon increases with the decrease in ionization energy. This is because the condensation time is longer for silicon, and that is why the silicon carriers are bigger than plasmonic probes. The relative concentration of silicon and gold in biosensors was determined through an EDX analysis (Figure-2.2b)). By adjusting the laser ionization energy, the maximum concentration of gold in the biosensors was 12.29% and the minimum was 0.71%. Whereas the maximum silicon concentration was 32.63%, and the minimum concentration was 27.2% (SI Table 1). Figure 3.3 provides the chemical composition of these plasmonic probes, analyzed by X-ray Power Diffraction (XRD) and X-ray Photon Spectroscopy (XPS). The XPS spectra in Figure 4.3 shows that the synthesized silicon sensor peaks at binding energies of 102 eV (Si2p3) and 103.5 eV (Si2p1), depicting the presence of silicon and silica, respectively. The PQPs peaks at binding energies of 85.05 eV, 87 eV and 89 eV, corresponding to the Au4f7, Au4f5 and Au4f phases, respectively [100]. The SERS active quantum probes consisted of the different phases of silicon and gold (SI Figure 1). The first phase indicated a gold oxide, while the last two phases pointed to the purest form of gold which was chemically stable and biocompatible [37]. Prior

research showed that SERS-active metal and semiconductor oxides could amplify Raman scattering enable the detection of molecules at deficient concentrations and generates the fingerprint of the molecule [101]. The binding energy of Au4f seems to be higher due to the small size of gold. The XRD Figure 3.3 peak confirmed the presence of gold oxides at 38.22°. The XRD spectrum also explains the presence of crystalline silicon (69.21°). The sharp peaks of the XRD gold spectra show that the gold particles mostly have a crystalline structure. On the other hand silicon and silica particles are a combination of crystalline and amorphous structures. For further use of sensing applications all the three sizes and concentrations of gold silicon particles were used.
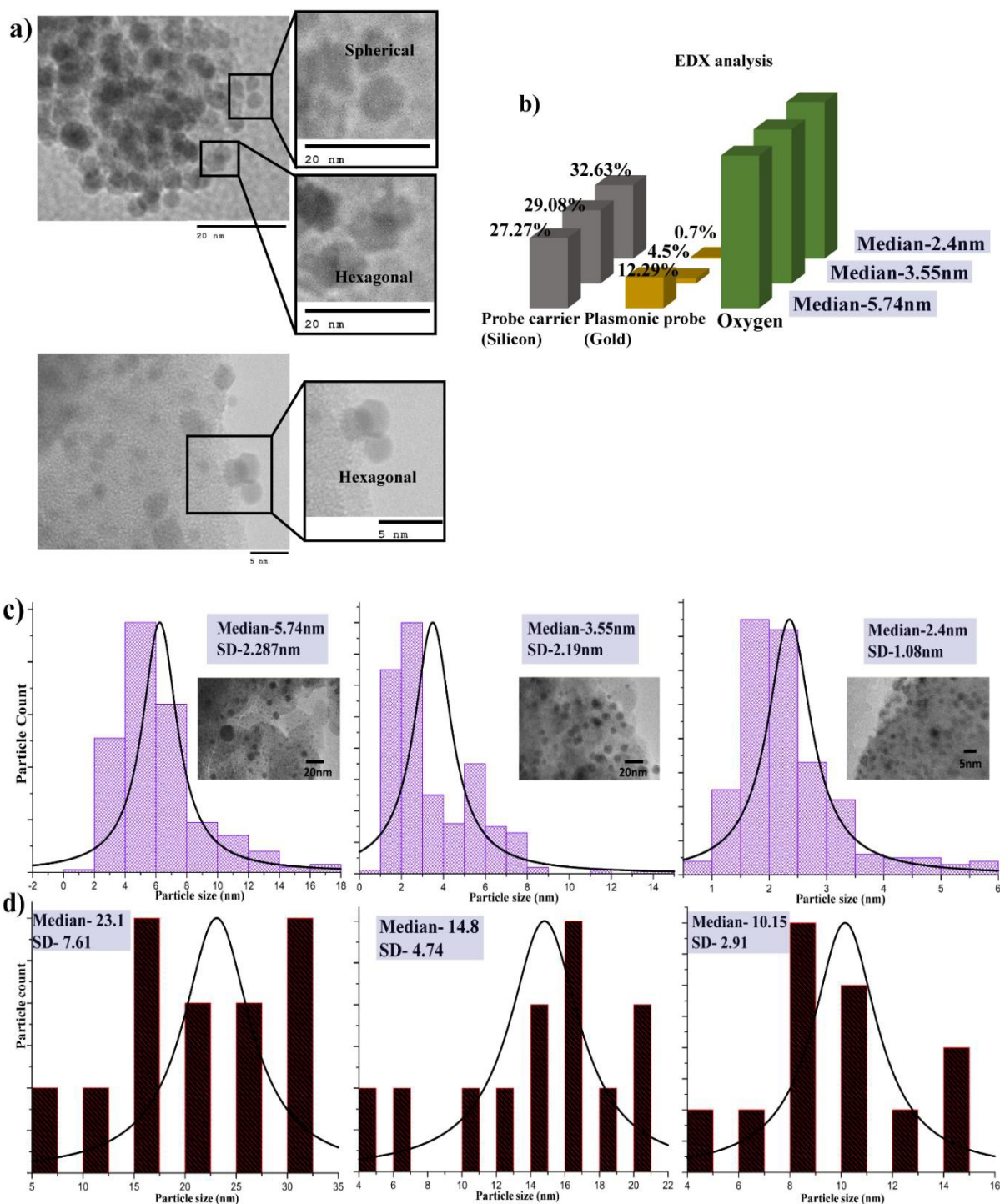
Figure 3.2 a) HRTEM images with a schematic illustration of Plasmonic quantum probes b) Elementary composition of PQPs and silicon for same conditions c) Particle size distribution of PQPs d) Particle distribution of silicon carrier.
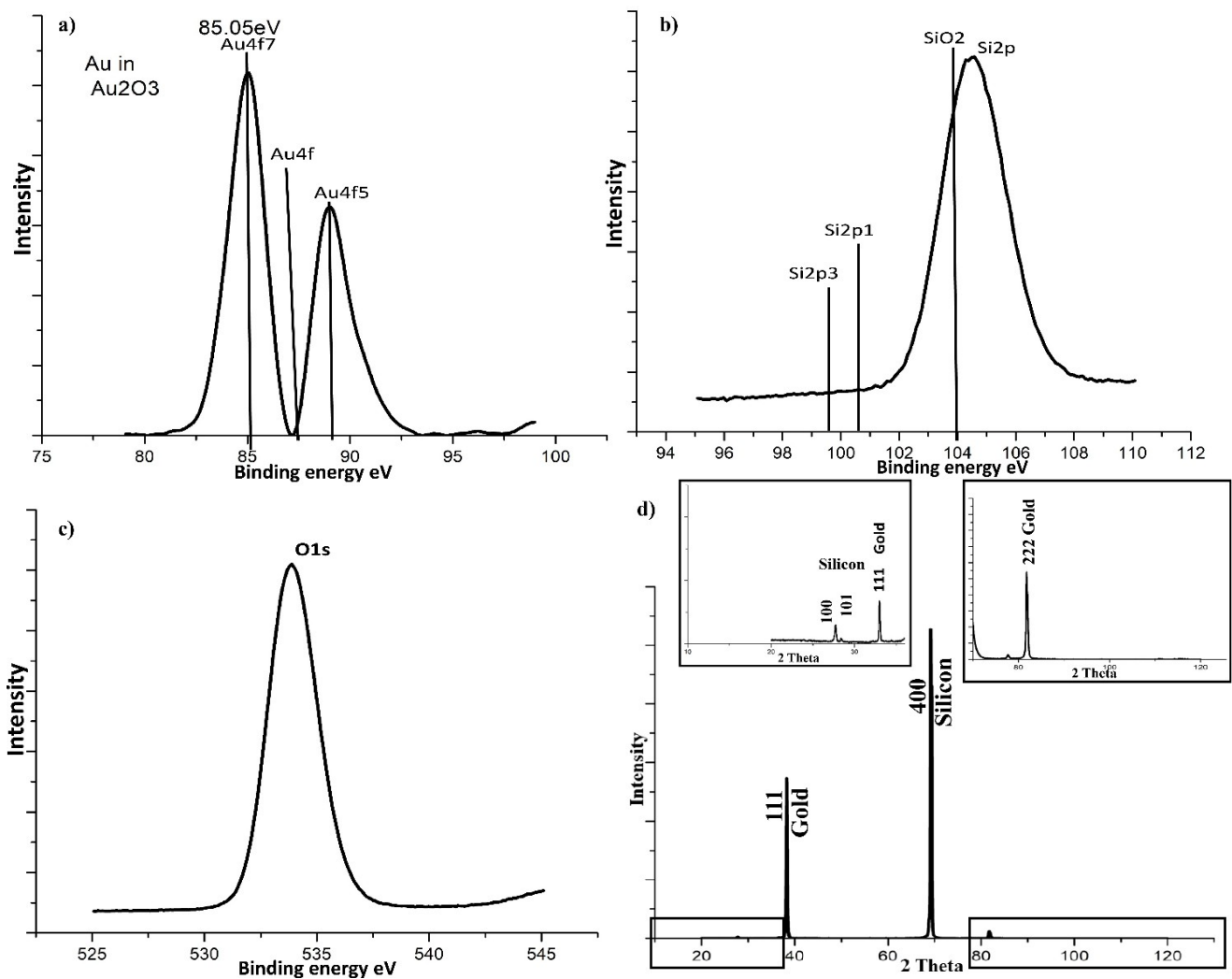
Figure 3.3 a) XPS spectrum for plasmonic probes b) shows the XPS spectrum of silicon carrier

c) shows the presence of oxygen d) XRD spectrum for PQPs and silicon carrier

3.4.2 Passive diffusion Cell uptake of PQPs

3.4.2.1 Number of particles inside a cell

The cellular uptake mechanisms of the PQPs were evaluated by using the Bio-TEM images taken

18 hours after cell seeding. Selected images are given in Figure 3.4.

Earlier research shows that there are two prominent PQPs uptake mechanisms dependent on the

size of the PQPs, endocytosis and energy independent passive mechanism [102]. Figure 3.4 A)

shows the membrane bending of cells towards the PQPs the early stage of membrane

53

encapsulation. Endocytosis is a time-dependent process and may take up to 24 hours to internalize particles [78]. At the 18th hour only encapsulation on the membrane was observed and did not find any vesicles in the cell. Figure 3.4 B) shows the PQPs cross the membrane by the energy-independent passive uptake [91].

Prior investigation of the cellular uptake mechanism mostly focused on large probes of size greater than 5 nm [103], [104]. The uptake pathway starts with endocytosis followed by the formation of early endosome and completed by translocation via the endosome and lysosomes. Due to the engulfing of the early endosome probes condense and demonstrate co-localization. The intensity of co-localization increases with extended cell culture time. The probes used for this research are much smaller. Figures 3.5 shows that the PQPs inside cells are of similar size as those outside cells shown in Figure 3.4 A) & B). This indicates that the endosome did not internalize these plasmonic probes. Individual PQPs can be observed even inside the nuclei as shown in Figure 3.4. As no endosome was found in all three cell lines results conclude that all the PQPs were internalized through an energy-independent passive uptake.

With an energy-independent passive uptake nanoparticles could reach intracellular components and nucleus of the cell after one hour of cell seeding [105]. In this research the PQPs did not cross the membrane until the 6th hour of cell culture. The delayed uptake could be explained by the 3D architecture of the plasmonic quantum probes which was known to hamper diffusion of probes[105]. The interconnected silicon/silica particles formed web and held the PQPs hampering their mobility. After 6 hours of cell culture silicon/silica particles degraded, disintegrated and PQPs are released. Cancer detection is a time-consuming process. Generally it takes a few days after sample collection to reach an accurate diagnosis. The results of this research show that it is possible to detect cancer cells within a few hours.
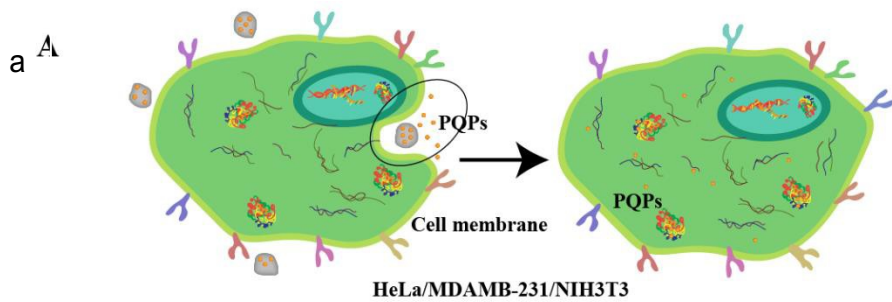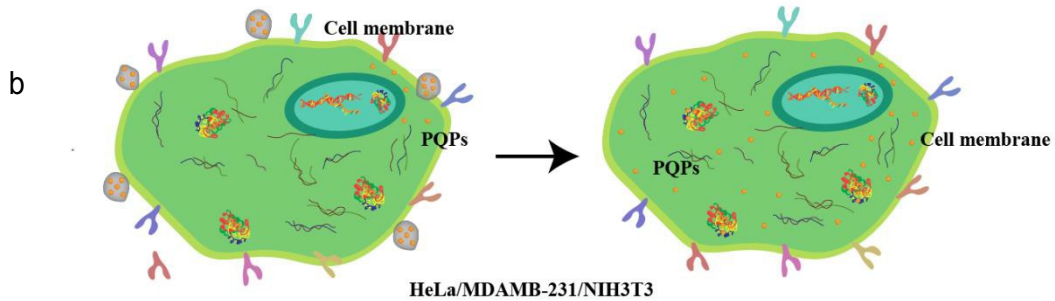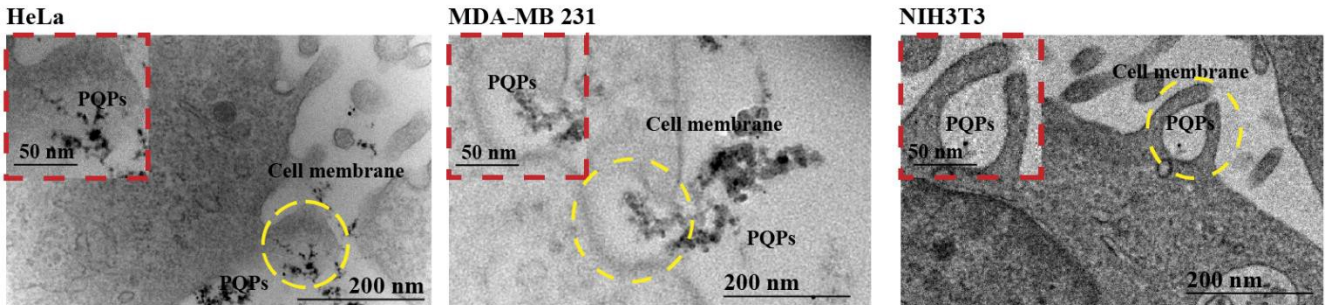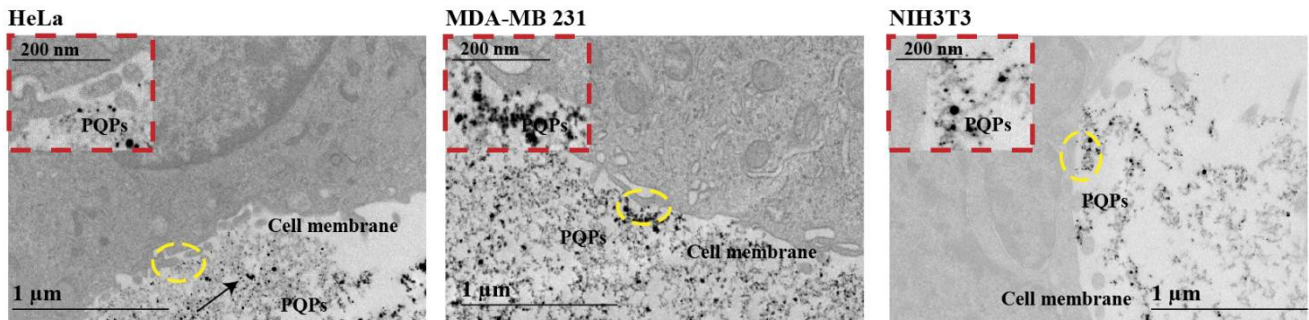
Figure 3.4 a) the uptake of PQPs in cancerous and non-cancerous cells by endocytosis uptake mechanism after 18 hours of cell seeding. b) The uptake of PQPs in cancerous and non- cancerous cells by energy-independent passive uptake mechanism after 18 hours of cell seeding

3.4.2.2 Intercellular Distribution of quantum probes

Bio-TEM images in Figure 3.5 showcase the presence of the label-free PQPs inside the cell and the nucleus. The interaction of the label-free PQPs with intracellular components such as DNA, RNA, proteins and lipids is highlighted.

Figure 3.5 shows the interaction of PQPs with intracellular components like proteins, actins and lipids. The quantum size of plasmonic probes was a driving force for protein and lipid sensor binding. As the quantum size has the highest surface area it was hypothesized that the interaction between biosensors and intracellular components was through electrostatic and hydrophobic interaction. The gold surface forms strong bonds with the thiol groups present in proteins [91], [106]. Figure 3.5 shows the uptake of PQPs in the nucleus and the interactions between PQPs and DNA/RNA. The nuclear envelope comprised of a lipid bilayer and equipped with 9 nm channels. Due to this entry into the nucleus is restricted. Due to quantum size plasmonic probes pass the nuclear envelope quickly.

Based on the data provided by Gunter Schmid the gold particle size of approximately 2 nm attaches to the major grooves of DNA through electrostatic interaction [107].

The Raman spectra given in Figure 3.7 were collected after 6 hours of cell seeding. The signature peaks mostly corresponded to surface receptors (EGFR) and the phospholipids present on the cell membrane. This is evidence that the PQPs are mostly located on the membrane. Whereas the signature peaks in Figure 3.8, which were collected after 18 hours of cell seeding represent the presence of intercellular components including proteins, lipids and DNA/RNA. This is clear that from the 6th hour to the 18th hour the sensor particles mobilized from the membrane to the internal of cells reaching the inside of the nucleus.
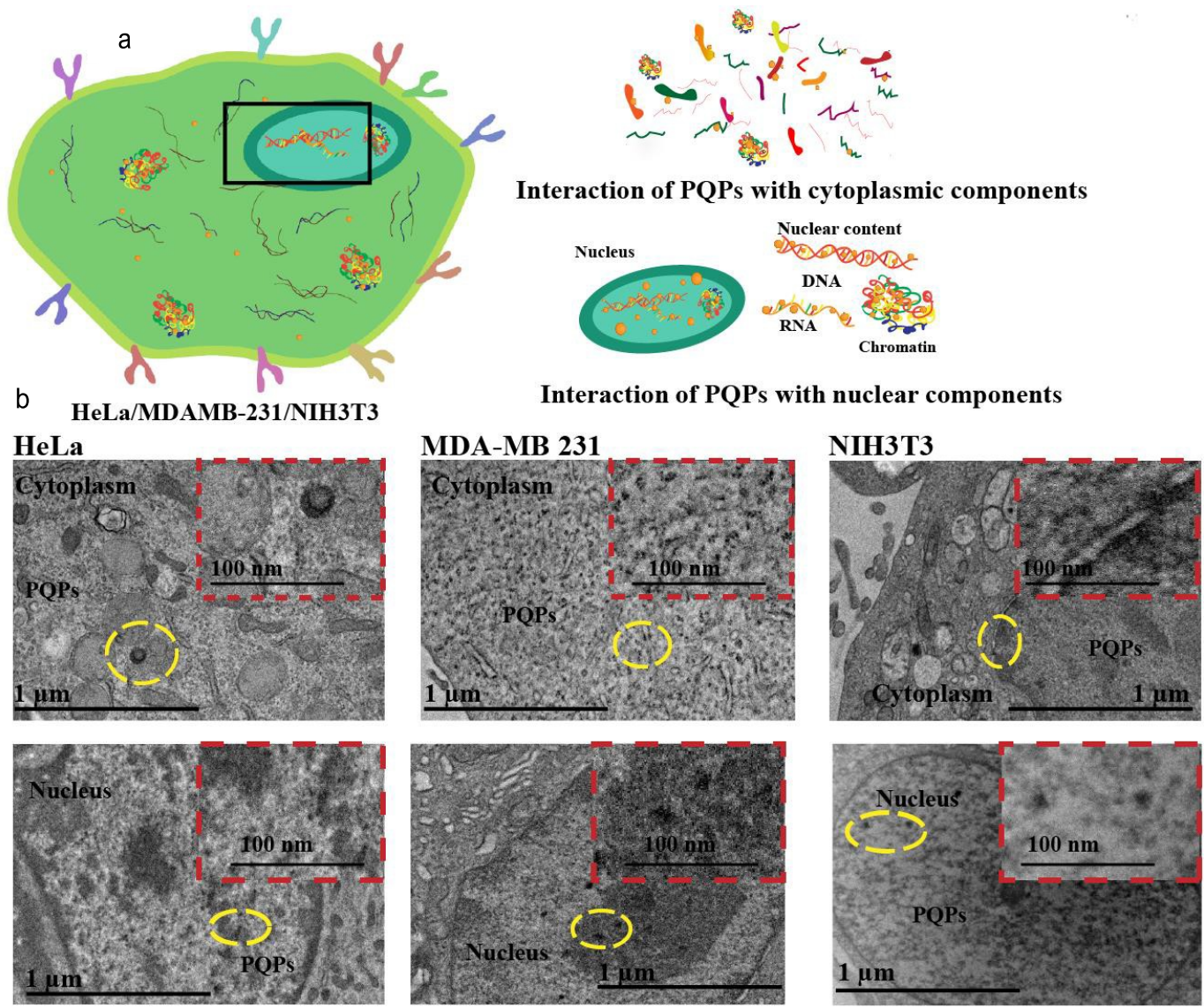
Figure 3.5 a) Schematics illustration for interaction between plasmonic quantum probes and cytoplasmic and nuclear components b) Bio TEM images shows the interaction between PQPs and the cellular components.

3.4.2.3 Classification of cancerous and non-cancerous cells by the uptake of PQPs

Figure 3.6 a) shows the schematics of uptake of PQPs in cancerous and non-cancerous cells, b) & c) shows the presence of PQPs inside the cancerous cells (HeLa and MDA MB-231). Figure 3.6 d) shows the presence of PQPs inside the non- cancerous cells (NIH 3T3) e) shows a comparison between the average number of PQPs inside cancerous and non-cancerous cells,

The different uptake of PQPs can be influenced due to several factors. First, the plasma membrane of different cells has different lipid compositions which determines the physical property of the cell membrane and makes them react to sensors differently. Secondly, different cell types express different membrane receptors. For example, few cells express a large number of scavenger receptors that help assume sensors non-specifically. Lastly, subcellular organelles have a different impact on sensors. It is well understood that cancer cells have an extraordinary ability to alter pathways or modify the protein expressions so that they can survive better [108]. In other words due to the mutated receptors and modified intercellular components the cancerous cells have an aggressive replicative nature and extensive fibrosis which makes them uptake particles more readily than healthy cells.

Table 3.1 gives the average number of particles internalized by the three cell lines. Cancerous cells uptake 6~9 times more PQPs than fibroblast cells. Therefore, SERS output from cancerous cells can be expected.

Table 3.1 Number of PQPs in each cell lines after 18 hours of cell seeding calculated from Bio TEM images of cells presented in Figure 3.6

Cell Lines	Average Number of PQPs Per Cell
MDA-MB 231	37
HeLa	23
NIH3T3	4

The uptake of PQPs is much higher in cancerous a cell which allows the increase in enhancement and sensitivity of SERS fingerprint for cancerous cells. Figures 3.7 and 3.8 show the increased intensity and sensitivity of SERS signals in cancerous cells compared to non-cancerous cells.
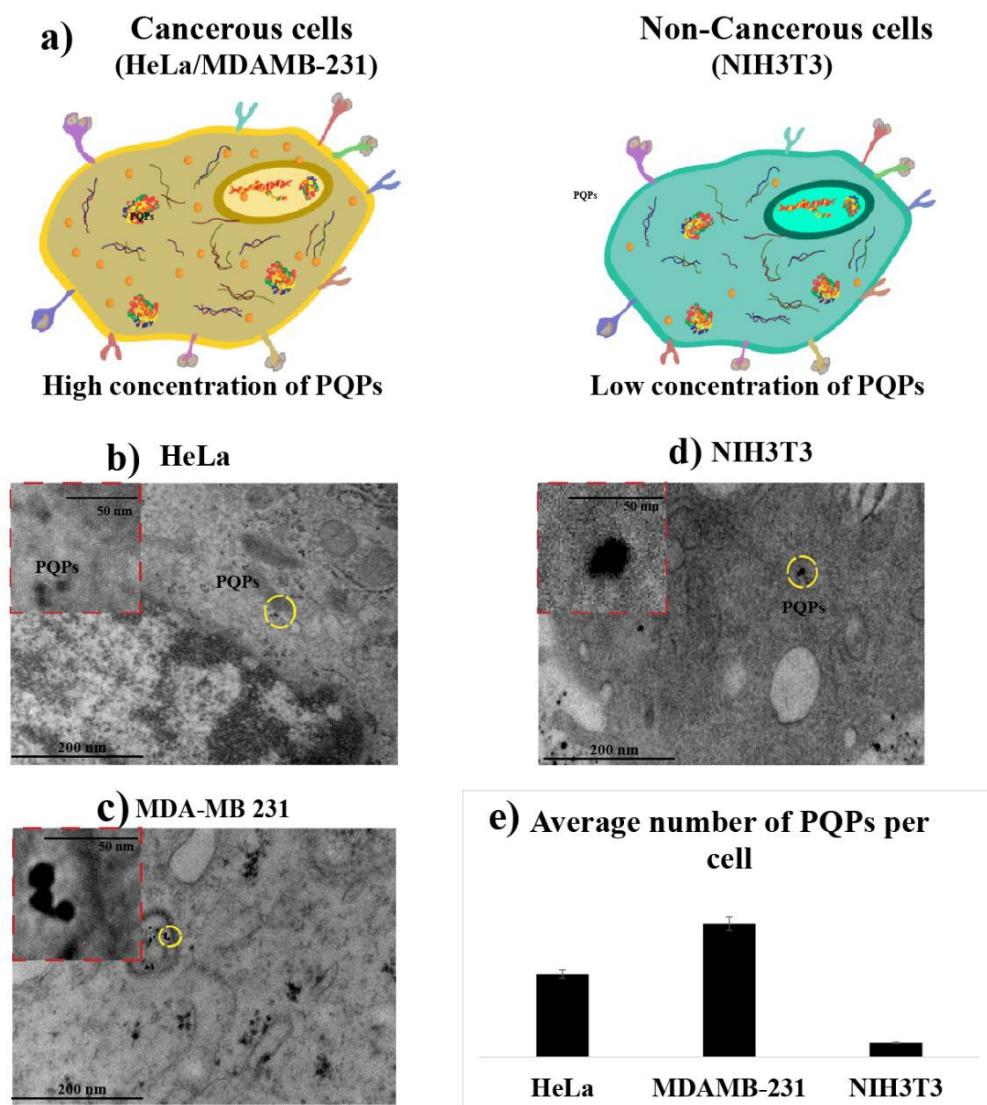
Figure 3.6 Different uptake of PQPs in cancerous and non-cancerous cells a) shows the schematics of uptake of PQPs in cancerous and non-cancerous cells, b) & c) presents the Bio- TEM images showing the presence of PQPs inside the cancerous cells (HeLa and MDA MB-231). Figure 6 d) Bio-TEM shows the presence of PQPs inside the non- cancerous cells (NIH 3T3) e) shows a comparison between the average number of PQPs inside cancerous and non-cancerous cells

3.4.3 SERS sensing of Surface markers: oncoprotein

A portable Raman spectroscopy with a laser wavelength of 785 nm was used. The 785 nm laser wavelength was selected since it can penetrate tissues and can be directly used for *in-vitro* and *in-vivo* applications [109].

Figure 3.7 shows the enhanced plasmonic readout of EGFR in cancerous and non-cancerous cells after 6 hours of seeding. The group of markers used for molecular classification of breast cancer type includes estrogen receptors (ER), progesterone receptor (PR), HER-2, p53 and basal marker like Epidermal Growth Factor Receptor (EGFR). Among these EGFR shows an important role. The activation of EGFR results in uncontrolled cell growth (increased cell proliferation), invasion, metastasis and angiogenesis. The expression of EGFR was found mainly in basal-like carcinoma (triple-negative carcinoma)[110]

Here the breast cancer cell lines (MDA MB-231) were selected as it is highly invasive and retains the ability of stemness and has a mesenchymal-like morphological appearance. It is triple- negative which means the concentration of estrogen hormone, HER2 oncoprotein and progesterone are negligible [111]. In contrast, the transmembrane EGFR is overexpressed in triple-negative breast cancer cells [112]. Therefore, in this study EGFR oncoprotein was used as a marker instead of testing the PQP diagnosis of breast cancer (MDA MB-231).

The obtained Raman spectra contain a large number of signature peaks corresponding to cellular metabolites. For instance, the peaks at 1127 cm^{-1}, 1582 cm^{-1}, and 1660 cm^{-1} were mostly associated with the wild type EGFR [113]. According to the data provided by Jichun, these peaks belong to carotenoids in malignant breast cancer tissues [114].

In addition to EGFR, lipids, protein and nucleic acids associated with EGFR are also present in the spectra peaks. The peaks at 1080 cm^{-1} are related to the C-N, C-C stretch of proteins, and 1447 cm^{-1} showed C-H deformation, nucleic acids, proteins and lipids [115], [116]. These peaks relate to the fingerprint of enhanced expression of pure nucleic acids and proteins which comes from an aggravated synthesis of fatty acids due to the upregulation of EGFR receptors in cells [117]. Therefore, the detection of these peaks can be used as supporting information for the identification of EGFR. The simultaneous detection of oncoprotein and its associated metabolites in a single Raman spectrum improves the accuracy of a breast cancer diagnosis. The detection of a single peak associated with the EGFR oncoprotein is usually insufficient for the cellular diagnosis of breast cancer. Here almost all the peaks associated with EGFR and also the mutated lipids and proteins peaks associated with breast cancer were simultaneously identified in a single Raman spectrum. This is because here the synthesized probe size is close or smaller to the size of cellular metabolites which helps the non-specific binding of PQPs with the complex cellular metabolites and provides almost all the possible peaks associated with the metabolites. With the present data cancer can be detected and can differentiate breast cancer with other cancer types.

Figure 3.7 shows the peaks associated with mutant EGFR are prominent in MDAMB 231, whereas the spectra collected from HeLa cells do not show any significant peaks associated with EGFR. However, the peaks associated with normal fibroblast cells were seen in Raman readout of HeLa cells. Some prominent peaks observed at 1158 cm^{-1}, 1266 cm^{-1}, 1518 cm^{-1} and 1750 cm^{-1} in normal fibroblast cells [118]. These peaks are mostly generated by normal tissues as stated by the previous researchers. For instance, 1158 cm^{-1} and 1266 cm^{-1} are assigned to C-C, C-N stretching mode of protein. The other peaks belong to a mixture of lipids and proteins.

Figure 3.7 B) shows the intensities of the several peaks associated with the mutated EGFR all of them are significantly higher for breast cancer. Figure 3.7 C) shows peak intensity at 1582 cm^{-1} compared to that of control. Breast cancer cells show 700 times higher intensity compared to the control which is distinctively higher than those of HeLa and fibroblast. Since breast cancer uptakes the most number of particles, it is expected that the readout from breast cancer cell has the highest intensity. Figure 3.7 D) shows the peak intensities at 1582 cm^{-1}nominalized by the intensity at 1126 cm^{-1}of the same cells. The results show that breast cancer is characteristically different from Hela and fibroblast. The intensity of EGFR at 1582 cm^{-1} is high for breast cancer and the difference between three types of cells is stable and large enough to be used to differentiate distinct cancer types. Therefore, the analysis of peak positions and intensities of EGFR, differentiation between the healthy cells from the cancerous cells could be accomplished

Figure 3.7 E) shows the schematics of interaction between cell membrane proteins with the plasmonic probes supported with the real-time Bio-TEM images of cancerous and non-cancerous cells.

Table 3.2 Raman spectral peak assignments for Raman spectra shown in Figure 3.7 and 3.8

Raman Shift cm^{-1}	Molecular assignments [116], [119]–[121]
1095	O-P-O symmetric stretching
1125	C-N stretching in protein
1155	C-C and C-N stretching of proteins and lipids
1311	CH$_3$ twisting mode of collagen and lipids
1485	Amide II
1615	C=C tryptophan
1620-1700	Amide I (C=O stretching, and N-H bending, protein)
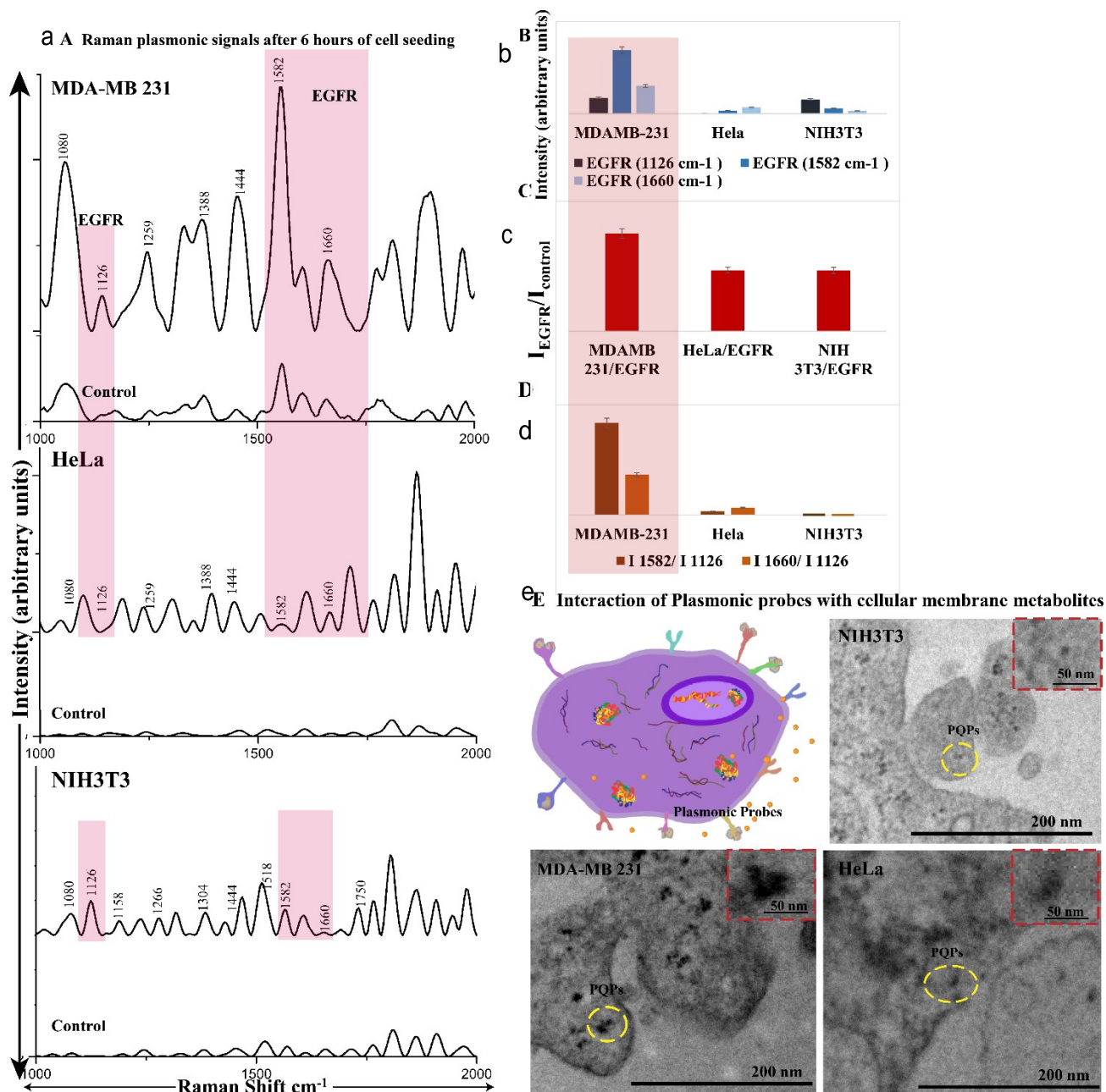
Figure 3.7 a) Plasmonic Raman signals for breast cancer (MDA-MB-231), cervical cancer (HeLa) and healthy fibroblast cells (NIH3T3) were collected after 6 hours of cell seeding, b) comparison between the intensities of mutated surface marker (EGFR), c) Shows the intensity comparison between control and EGFR intensity d) shows the peak intensities at 1582 cm-1 nominalized by the intensity at 1126 cm-1 of the same cells e) schematic illustration for interaction between plasmonic probes and membrane proteins.

3.4.4 SERS analysis of the Intercellular oncoprotein

Figure 3.8 gives the plasmonic readout for intracellular metabolites (Such as HPV E6 and HPV E7) breast cancer, cervical cancer and healthy fibroblast cells after 18 hours of seeding. Cervical cancer cells overexpress human papillomavirus (HPV). Usually, HPV E6 and E7 genes are identified as the essential virus-related oncogenes [122]. The HPV E6 and HPV E7 proteins modulate the cellular metabolites that regulate cellular functions such as cell growth. These oncogenes are associated with tumor suppressor proteins (p53 and pRb). The E6 oncoprotein promotes cell proliferation by stimulating the degradation of tumor suppressor proteins resulting in the perturbing of the cell cycle process leading to angiogenesis [123]. The HPV E6 proteins in cervical cancer interfered with the function of the cellular tumor suppressor protein which indirectly leads to cellular transformation 72,73. The HPV E7 oncoprotein binds with the tumor suppressor protein pRb. E7 disrupts the interaction of pRb and the transcription factor which stimulates the replication and cell division. This results in the cellular transformation and leads to the disruption of the normal physiology of the cellular function of specific tumor suppressor protein [87]. Hence, the detection of HPV genes is frequently used for the screening of cervical cancer.

The selected cervical cancer cell line (HeLa) is highly aggressive and metastatic. Here the peaks selected for the representation of E6 and E7, are mostly used by the researchers for the sensing of cervical cancer. HPV E6 protein (HeLa) had peaks at 1047 cm$^{-1,}$ which showed the carbohydrates with C-O stretching, 1172 cm$^{-1,}$ which showed the presence of C-C stretching in phenylalanine and tyrosine and 1297 cm^{-1} showed CH_2 deformation [119], [120]. HPV E7 (HeLa) had a range of peaks. In the present study the three most highly expressed peaks were selected, the peak at 1340 cm^{-1} showed the polynucleotide chain (DNA bases), 1452 cm^{-1}

showed CH_2 deformation in lipids and peak rose from 1661 cm^{-1} was due to the Amide I: α helix [119], [126]. The HPV E7 proteins interacted with pRb-associated rocket protein which resulted in the release of transcription factors and subsequent activation of genes promoting cell proliferation [127]. These respective peaks were selected due to their higher concentration in cervical cancer cells compared to healthy cells [120].

Here the peaks associated with upregulated HPV are more dominant in HeLa cells as compared to breast cancer cells and healthy fibroblast cells. Few signals such as peaks at 1340 cm^{-1} and 1172 cm^{-1} associated with E7 and E6 proteins are not even visible in other cancer types and healthy fibroblast cells.

Figure 3.8 B) shows the intensities of the two peaks associated with the HPV E6 and E7 both of them are significantly higher for cervical cancer. Figure 3.8 C) shows the peak intensity at 1340 cm^{-1} normalized by that from the control sample. Cervical cancer cells show 850 times higher intensity compared to control which is significantly higher than those from MDA MB 231 and NIH 3T3 cells. Figure 3.8 D) shows the peak intensity at 1340 cm^{-1}and 1172 cm^{-1} normalized by intensity at 1047 cm^{-1} of the same cells. The graphs resulted in that signature peaks from the cervical cancer is characteristically higher than those of MDAMB 231 and NIH 3T3 cells even though cervical cancer cells uptake a fewer number of probes compared to breast cancer cells. Such a difference is repeated for at least two peaks, and the difference is significant enough to be used to differentiate cancer types.

Adding to HPV E6 and E7 Raman readout, the peaks associated with unscheduled DNA synthesis and immortalization of cells were also noticed. For instance, peaks at 1080 cm^{-1} show the PO_2 symmetric stretching for DNA/RNA which is mostly associated with the growth of DNA and peak at 1580 cm^{-1} associated with adenine, guanine, which represents the presence of

DNA/RNA [126]. These peaks relate to the overexpression of phosphate backbone and adenine/guanine, which result in the uncontrolled synthesis of DNA. The uncontrolled growth of DNA is related to the mutation of tumor suppressor proteins. Generally, cervical cancer shows over-expression of DNA as compared to breast cancer and other cell types.

Therefore, the sensing of these peaks can be used a supportive data for the detection of HPV E6 and E7. The simultaneous sensing of oncoproteins and its related intracellular components in a single Raman readout may provide the precise detection of cervical cancer. Usually, the sensing of a single marker peak associated with the specific cancer is not sufficient. Here two most commonly known oncoproteins associated with cervical cancer i.e, HPV E6 and HPV E7 together with the nucleic acid peaks related to cervical cancer simultaneously in a single Raman spectrum were sensed. This is due to the non-specific binding of plasmonic probes with the intracellular metabolites as a result of the quantum size of probes, which is almost similar to the size of cellular metabolites.

Many other peaks can be seen in Figure 3.8 that besides cancer markers because there are other proteins and lipids present on the surface of the cell membrane. Other generated peaks were explained in Table 3.3. Figure 3.8 E) shows the schematics of interaction between intracellular metabolites with the plasmonic probes supported with the real-time Bio-TEM images of cancerous and non-cancerous cells. Images show the unique dispersion of PQPs inside the cells including the nucleus resulting in the non-specific binding of PQPs with the intracellular metabolites. PQPs are capable of sensing multiple proteins and lipids simultaneously and prove the non-specific and ultra-sensitive detection of most of the cellular components.
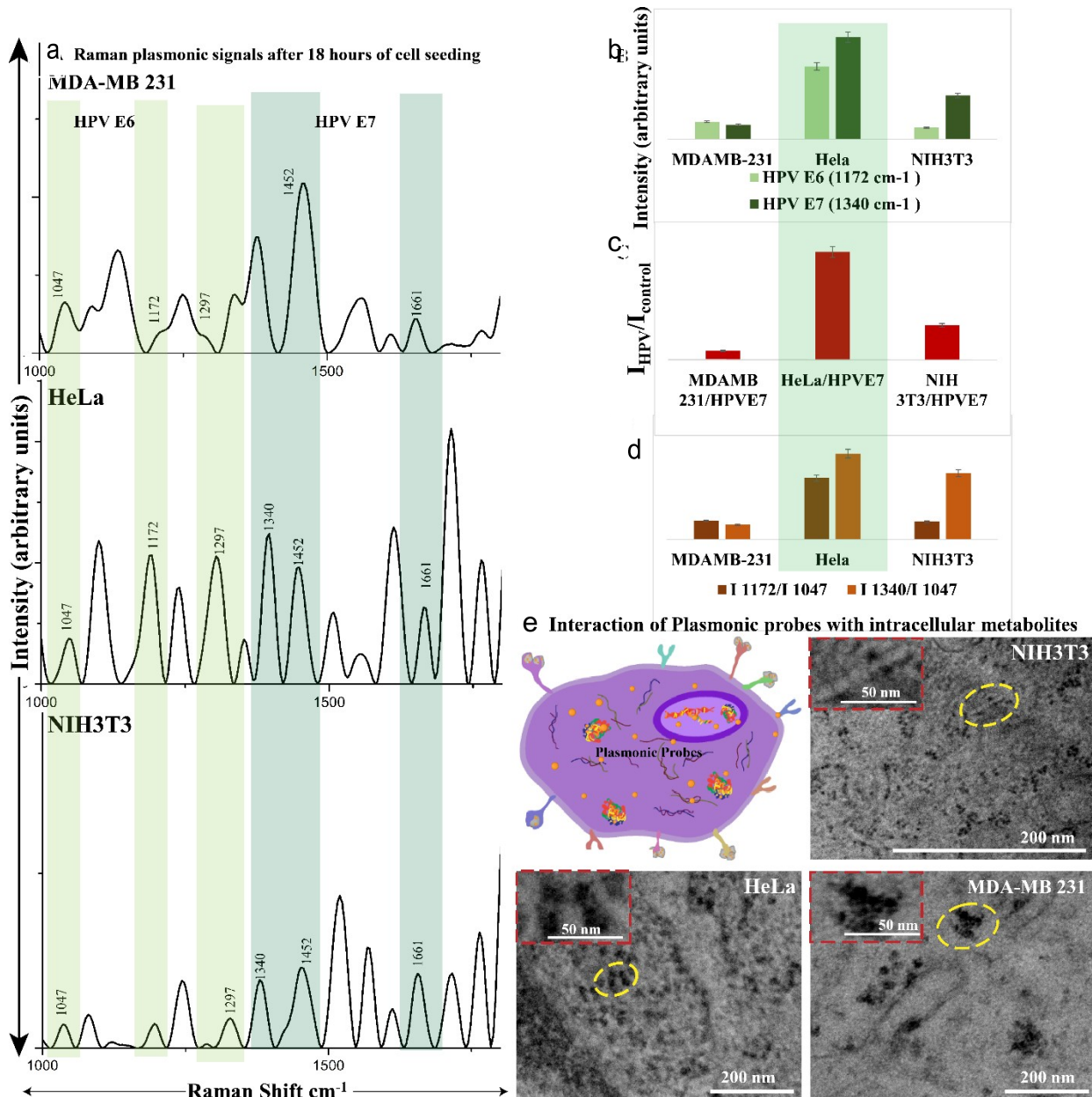
Figure 3.8 a) Plasmonic Raman signals for breast cancer (MDA-MB-231), cervical cancer (HeLa) and healthy fibroblast cells (NIH3T3) were collected after 18 hours of cell seeding b) shows the intensities of the two peaks associated with the HPV E6 and E7, both of them are significantly higher for cervical cancer c) shows the peak intensity at 1340 cm^{-1} normalized by that from control sample d) shows the peak intensity at 1340 cm-1 and 1172 cm^{-1} normalized by intensity at 1047 cm^{-1} of the same cells. e) Schematic illustration for interaction between plasmonic probes and intracellular components.

3.4.5 Monitoring nucleus

Figure 3.9 represents the plasmonic readout of cancerous and non-cancerous cells after 6 and 18 hours of cell seeding presence of plasmonic probes inside the cells and nucleus and it also represents the increase in the intensity of enhanced Raman signals as compared to the native. Figure 3.9 a) shows the plasmonic readout for the healthy fibroblast cells with an increase of seeding time there is an increase in the intensity of signals generated by the cellular components. Figure 3.9 b) gives the interaction between plasmonic probes and cytoplasmic and nuclear components in breast cancer cervical cancer and healthy fibroblast cells.

Few cancer-specific surfaces and intracellular oncoprotein for breast cancer and cervical cancer respectively have been diagnosed (Figure 3.8). Now to monitor the progression of cancer here different phases of the cell cycle (G1 phase, S phase G2 phase, and M phase) were studied which helps to monitor the growth of the tumor. During G1 a phase cell prepares for cell division, at restriction point, the cell moves to S phase for DNA synthesis and replicates the genetic material. Now in the G2 phase, metabolic changes assemble the cytoplasmic material for mitosis and cytokinesis. In the M phase a nuclear division takes place, followed by the cell division [128].

Figure 3.9 shows the plasmonic readout; the bands around 658 cm^{-1}, 844 cm^{-1}, and 1322 cm^{-1} correspond to guanine sugar-phosphate, adenine, guanine and RNA shows the presence of the cells in G1 phase. CH_2 molecule at 1448 cm^{-1}, amide I bond at 1655 cm^{-1} and ester bands at 1750 cm^{-1}. Additionally, the S phase shows the dominance of proteins and nucleic acids were in the range of 1200-1400 cm^{-1} associated with amides III and CH_2, and amide I band at 1651 cm^{-1} [129]–[131]. There is a significant increase in the peak at 1273 cm^{-1} assigned to the G2/M phase from 6 hours to 18 hours of cell seeding [132].

The peak at 1070 cm^{-1} showed the most variation in cancerous and a non-cancerous cell which signifies the symmetric PO$_2$$^-$ stretching for DNA (represented more DNA in the cell). Adding to that not only variation but also presented the growth (G1) of cancerous cells.

Since fibroblast cells internalize a significantly lower number of PQPs (Table 3.1) the Raman spectra profiles obtained from fibroblast cells are not as good as those from the cancerous cell lines mainly there are fewer signature peaks and the intensity is comparatively much lower in the 0~1500 cm^{-1} wave-number region. These results indicate that with the addition of PQPs cancerous cells will be more visible and more comfortable to detect than healthy cells. In the present study, different peaks were identified for different cell lines which indicated that SERS could also be used to differentiate the cell type.

Figure 3.9 a) Plasmonic Raman signals for breast cancer (MDA-MB-231), cervical cancer (HeLa), and healthy fibroblast cells (NIH3T3) were collected after 6 and 18 hours of cell seeding to monitor the growth of cells by studying the G0 G1 and G3 phase of the cell cycle. b) Bio TEM images show the interaction between plasmonic probes and nucleus components.

Table 3.3 Raman peak assignments for the peaks shown in Figure 4.8 and 4.9

Peaks	Peak Assignments
1060-95 cm^{-1}	PO^{2-} stretching (DNA/RNA) [133]
1070 cm^{-1}	Symmetric stretching for PO^{2-} (DNA/RNA) [134]
1180 cm^{-1}	Cytosine and guanine [135]
1257 cm^{-1}	Amide III beta-sheet [136]
1200-1300 cm^{-1}	=CH bending, thymine and adenine (DNA) [133]
1220-84 cm^{-1}	Thymine and adenine (DNA/RNA) [133]
1340 cm^{-1}	Nucleic acid mode
1373 cm^{-1}	Ring mode of DNA/RNA (adenine, thymine, and guanine) [136]
1490 cm^{-1}	DNA [134]
1663 cm^{-1}	DNA [137]

3.4.6 Effect of quantum size on SERS intercellular signaling

The particle size, shape, and surrounding environment affect the excitation of localized surface plasmon resonance. Gold nanoparticles sized from 2 to 100 nm typically enhance the electric field and optical absorption [138]. The unique property of plasmonic material is the distribution of the plasmon field. The vicinity of the active plasmonic zone (plasmonic filed) is inversely proportional to the distance from the surface of the gold probe (r) [139], [140]. The electric field inside the particle is consistent. However, surface plasmonic active zone decreases with an increase in the size of the probe. Showed in the following equation [139]

$$E \propto \frac{1}{r3} \qquad \text{- equation 1}$$

Therefore, when a metabolite is located near the plasmonic probe close to the active localized plasmonic zone it can cause an enhancement of the metabolite's RAMAN signals. When the gold particle size reduces from a typical value of 20 nm to 2.4 nm, the active plasmonic zone increases by 300 times. The comparison of naked 2.7 gold probes used in this study and a typical layered gold particle is illustrated in Figure 3.10 A. With the increase in the size of the plasmonic probe and there was a decrease in the plasmonic zone which results in low RAMAN scattering. With the PEG layer, plasmonic resonance is damped which restricts the plasmonic readout of cellular components.

The minimum size of cellular components (such as markers, proteins, and DNA/RNA) biochemistries is 2-3 nm, comparable to that of the gold probes synthesized with a laser. The previous study about protein corona on nanoparticles indicated that particle size is directly proportional to the thickness of the protein corona [141]. Smaller particles with more significant surface curvature attach less protein. While dense hard corona can be formed on bigger particles it is speculated that only a single layer protein is attached to particle sizes around 5 nm [142]. Using quantum scale plasmonic probes the formation of thick protein corona can be avoided. The ability of a particle to attach to different types of proteins is not related to particle size. Small and big particles are equally attractive to various proteins. Therefore, quantum sized particles are optimal in terms of signing as the protein corona is not too thick to damp the plasmonic resonance on the surface of gold.

Quantum gold works differently from large gold nanoparticles, as stated by the previous researchers [143]. Since the nucleus membrane is equipped with 9 nm channels, bigger particles

74

have to be targeted with nuclear localization signal in order to translocate. In contrast, particles less than 5nm enter the cell nucleus easily. For instance, gold particles of 2.5 nm have been distributed inside the nucleus [144].

To study the intercellular components specific targeting such as cetyltrimethylammonium bromide (CTAB) and other serum protein labeling must be employed for the sensor to be able to penetrate the cell membrane and attached to subcellular components [145]. The PQPs created in this study uses a label-free non-specific approach. PQP binds with surface receptors, intercellular components and nucleus components simultaneously which enables the revealing of the complete signature of the whole cell.

The uniform distribution of plasmonic probes results in non-specific attachment of PQPs with the cellular and nuclear metabolites. Due to the non-specific binding the plasmonic readout reveals a generous amount of information. Multiple cell metabolites can be reflected on one single spectrum simultaneously. Figure 3.10 B shows the Raman spectra after 18 hours of cell seeding containing signatures of surface marker (EGFR), intracellular markers (HPV E6/HPV E7), and different cell cycle phases (G1, G2/M and S phase). The complete information of a cell can be obtained in one single detection. This potentially allows for cells to be identified through multiple markers, surface, intercellular or nuclear all at once leading to a more accurate diagnosis.

Figure 3.11 compares the spectral profile from different sizes of plasmonic probes from 5.7 nm to 2.4 nm. Figure 3.11 B) plots the intensity of peaks from HPV E6, HPV E7, EGFR, G1 phase, G2/M, and S-phase. The average intensity from all peaks decreases with the increase of probe size. The relation is linear, exponential and power for fibroblast, breast cancer and cervical cancer, respectively. No matter what the cell type the probe size is inversely related to the plasmonic readout. Based on Equation 1, here, the active plasmonic zone for all the different sizes

75

of probes was calculated. The plasmonic zone was 11 times higher for 2.4 nm probes than 5.7 nm probes, and it resulted in an intensity increment of 2-3 times.
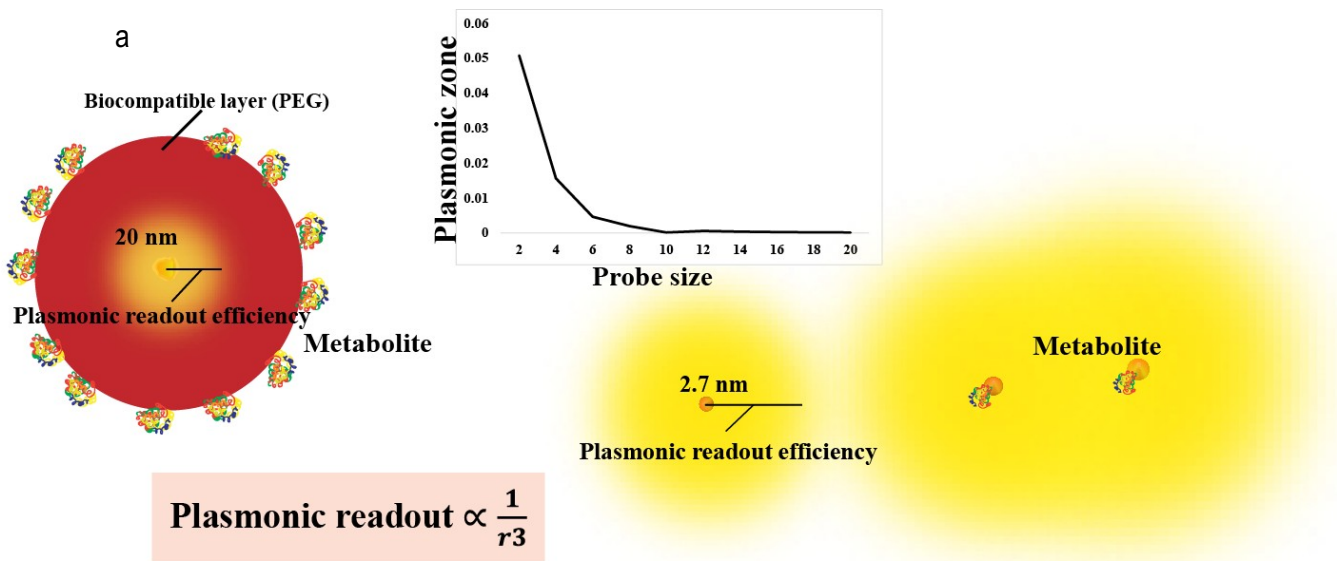
Figure 3.10 a) Concept for the generation of a plasmonic signal by the interaction between plasmonic probes and cellular metabolites b) Plasmonic signals of multiple cell metabolites simultaneously.
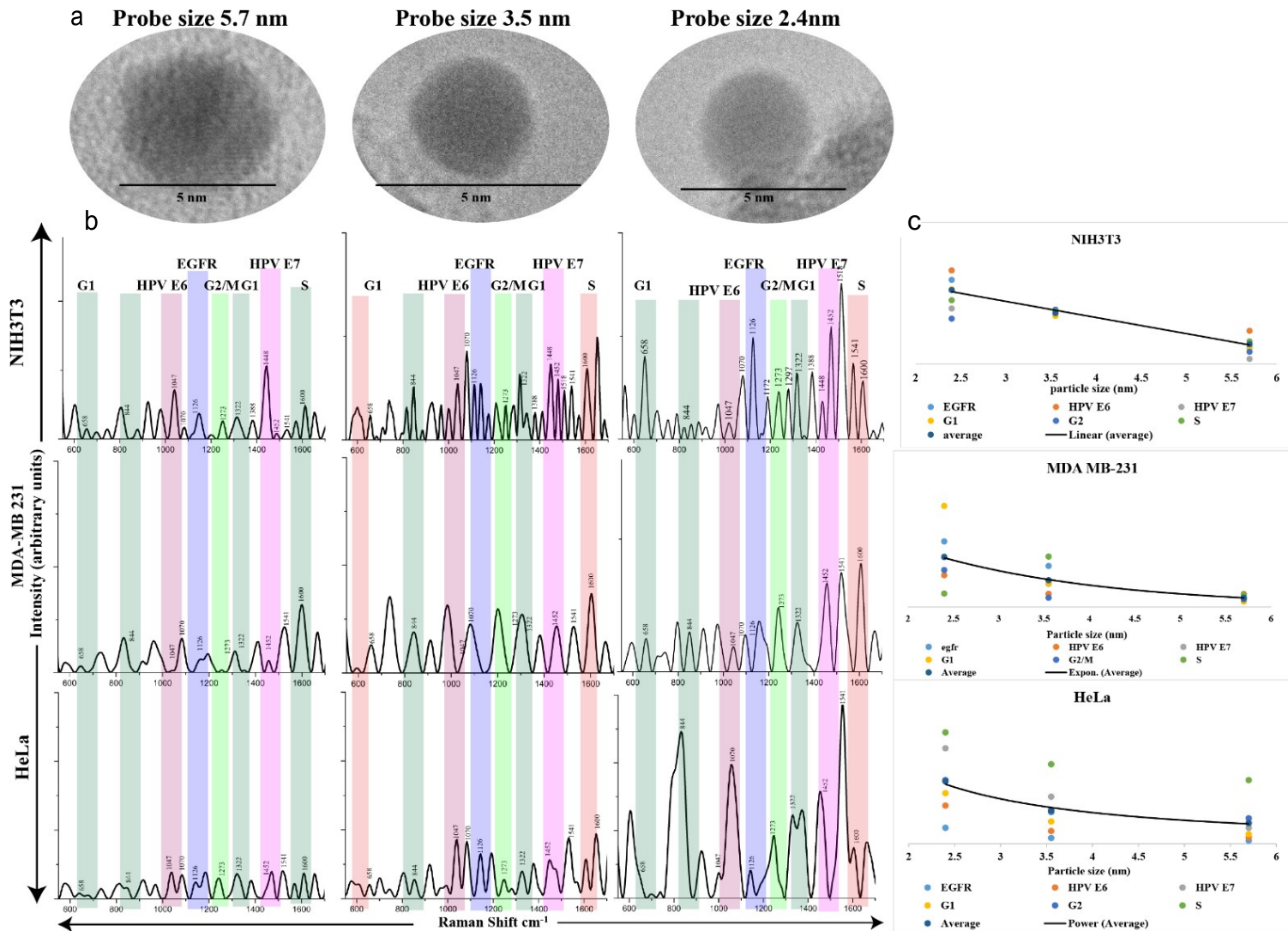
Figure 3.11 Exponential increase in the Raman intensity and signals with the decrease in probe size

3.5 Conclusion

In this study, the label-free and tag-free SERS detection of cancer was achieved. By using a physical method (laser-based synthesis), biocompatible PQPs were synthesized without chemical adulteration. The quantum-sized plasmonic probes showed unique self-internalization and

uniform dispersion inside the cells into the nucleus. The cellular images witnessed that Breast cancer (MDA-MB-231) and cervical; cancer (HeLa) cells internalized at least six times more PQPs than the normal fibroblast (NIH3T3) cells, which lead to more sensitivity and enhancement in SERS signals. MDA-MB-231 and HeLa cells can be differentiated without ambiguity from NIH3T3 through the signature peaks and their intensity. The probe size close to the size of cellular metabolites (~2-3nm) was achieved which successfully lead to the sensing of multiple mutated cancer receptors and oncoprotein (such as EGFR, HPV E6, and HPV E7) simultaneously, which could also be used to distinguish different cancer types (cervical and breast cancer). From the Raman readout it was observed that there was a 1000-fold increase in the intensity of cellular metabolites compared to control. The complete biochemistry information of a cell from the surface to the nucleus is revealed by a single detection which could be used for rapid and accurate identification of cell types. Our research may lead to a new type of platform for point-of-care sensing for reliable early cancer diagnosis. This approach could also be used for *in-vivo* diagnosis and clinical research in the future.

Chapter 4

Cellular DNA based Cancer diagnosis using Self-internalized plasmonic sensors

Submitted to Sensors and Actuators B

4.1 Abstract

The sensing of nucleic acids (DNA) by using distinctive properties of plasmonic materials has developed an entire stimulating area in biomedical applications specifically for the diagnosis of malignant diseases. Still regardless of many kinds of research the sensing of the complete conformation of DNA is restricted to labeled sensing, which is a laborious process and poorly sensitive traditional methods. Generally, the Surface-Enhanced Raman Scattering (SERS) technique has been used for sensing the DNA molecules by coating the plasmonic nanostructure with a biocompatible layer and complementary DNA strands. The labels and coating increase the overall hydrodynamic size of the probe which restricts the internalization inside the nucleus and DNA sensing stay limited to the sensing of cytoplasmic DNA or isolated DNA strands. Physically synthesized and self-functionalized small quantum probes are used for the intracellular sensing of DNA molecules without the need for labels and coatings. The presence of small quantum probes inside the nucleus increases the SERS enhancement yield by a minimum of 700 folds. The SERS signals resulted in the simultaneous sensing of multiple cellular components, including DNA and proteins which can be used for the analysis of cancer. Raman spectra present the different signal configuration because of the different molecular composition and different cell phases. Therefore, by using Principal Component Analysis (PCA) and Hierarchical Clustering analysis a significant difference between malignant (lung cancer and pancreatic cancer) and non-cancerous cells was achieved.

By using the same analysis lung cancer cells from pancreatic cancer cells were differentiated. This indicates that the un-tamped small quantum probes internalize inside the nucleus without altering the cellular metabolism and are capable of sensing genomic DNA molecules more accurately. The present study holds a promising potential for developing a new technique for accurate diagnosis of cancer-based on cell DNA diagnosis.

4.2 Introduction

It is well known that nucleic acid is the most important biological molecule. Nucleic acid amplification is a benefit for the diagnosis and management of a variety of different diseases [146]. Cancer poses significant genetic and morphological heterogeneity which is critical to understand the multiple aspects of a tumor in a given state [147]. Single tumor biomarker sensing judgment mostly fails to deliver an accurate diagnosis of the disease as required by clinicians [148], [149]. Cancer biomarkers are usually of low sensitivity and apply to only a small subset of patients with cancer. Quite a few biomarkers such as EGFR, are overexpressed in several malignancies such as lung cancer, colorectal cancer, breast cancer and glioblastoma multiform. Therefore, the detection of overexpressed EGFR will not clarify the diagnosis of a particular cancer type [150]. Therefore, biomarkers are not useful for the general screening of cancer. Thus extensive research has been done in the sensing of bigger panels of specific and quantifiable cancer biomarker diagnoses [149]. The simultaneous detection of intracellular biological components, including proteins and DNA hold the key to revealing the complete molecular signature of the malignancy thus accurate diagnosis [151], [152].

The importance of DNA sensing is steadily increasing in biomedical research. Recently, it starts to enter clinical diagnostics. A few techniques have been developed for the analysis of cell DNA.

Regardless of the working principle of the technique all of them must demonstrate selectivity and specificity when applied to cell signing. In other words, the technique should be able to identify DNA signals from a large number of background signals generated from various cell components [153]. There are two ways to accomplish this roadblock: analyzing isolated DNA, or using labels to tag the DNA inside a cell selectively [154].

For the analysis of isolated DNA, polymerase chain reaction and microarray techniques were used. These techniques mostly require fluorescent reports, multiple processes, complex analytical analysis, and a loss of conformal DNA structure[146]. Present DNA sensing analysis involves the application of fluorescent sensing wherewith fluorescent labeling of specific nucleic acid base generates the fluorescence response [155]. However, there are several drawbacks of using fluorescence sensing and it provides the limited characteristic information about the targeted DNA molecules.

Surface-Enhanced Raman Scattering (SERS) is an alternative method to the fluorescence diagnosis which is highly sensitive with single-molecule detection [156]. It is advantageous in capturing the detailed molecular signals of cellular components. SERS has lately appeared as an influential analytical device for quick detection and structural analysis of DNA by showing high sensitivity and compositional fingerprint signals. It has been used for the analysis of isolated DNA as well as intracellular DNA.

For the analysis of isolated DNA SERS are performed in two categories, label-free method and labeled method. The label-free method does not modify the DNA molecule. Instead, DNA molecules are directly mixed and bind with the plasmonic materials such as nanoparticles of noble metals. The significant advantage of the label-free method is that DNA information obtained is direct and original. However, the reproducibility and reliability of signals are usually

poor which is usually attributed to two factors. First, the manufactured nanoparticles generally have a coating of chemical molecules or functional groups adopted from synthesis processes which are wobbly and frequently which leads to the variation and noise of SERS signals [68]. Secondly, the contact of negatively charged DNA with the plasmonic material of a similar charge is usually brittle which avoids the actual electrostatic interaction with the plasmonic material needed for enhancement [146]. The labeled method then allows for the plasmonic nanoparticle to firmly adhere to the DNA and give rise to amplified signal strength[11] consequently better detections sensitivity. However, this technique needs the alteration of DNA. Moreover, the Raman labels are specific and do not amplify the full sequence of DNA equally [68]. To overcome this shortcoming hybridization can be used for in-direct labeling. Hybridization attaches the sample DNA to a complementary DNA target strand that is tagged with the Raman label. This method does not modify the DNA, but collected signals are from the complementary DNA molecules. The main drawbacks in the labeled sensing method include that enhanced sensitivity is essential to detect the nucleotide signals [157], high signal noise due to the adsorption of DNA targeted bases [158] and the covalent bonding of the DNA molecule during the immobilization or hybridization process may modify the DNA structure which may affect the accuracy of detection.

The labeled method is also used for SERS intracellular DNA detection. However, it is limited to the sensing of DNA molecules inside the cell cytoplasm. The detection of genomic DNA molecules inside the nucleus is scarce. This is because the channels on the nuclear membrane are as small as 9 nm, smaller than most of the nanoparticles employed for SERS, preventing the amplification of information inside the nucleus. The label-free method has never been reported for the SERS detection of nucleus DNA.

The SERS profile of intracellular DNA molecules for lung and pancreatic cancer and healthy fibroblast cells potentially can be used for differentiating the different types of cells and different cancer types. For SERS characterization un-tamped DNA quantum sensors (DNA quantum sensors) were synthesized by using the physical synthesis method. The physical synthesis eliminates the need for labels and biocompatible coatings as the synthesized DNA quantum sensors are without chemical adulteration and biocompatible. Here the SERS spectra from the intact cells treated with the DNA quantum sensors were obtained to study the DNA molecule in the *in vivo* environment. Therefore, all three different types of cells were incubated with the DNA quantum sensors, and BioTEM observation found that the DNA quantum sensors localize inside the cells into the nucleus through the endocytosis mechanism. The presence of DNA quantum sensors inside the cells enhances the yield of SERS signals by 700 folds. The Raman excitation resulted in the simultaneous sensing of multiple biomolecules including DNA and proteins associated with the malignant disease. However, each SERS spectra can show different signal compositions even in the situation of the same origin cells because the biomolecular composition and phase of the cells are distinguished. Hence, Principal Component Analysis (PCA) and hierarchical clustering analysis (dendrogram analysis) were used to identify the significant difference in the SERS spectra of the intracellular DNA molecules of different cell types [159]. This indicates that the un-tamped DNA quantum sensors are capable of accurately sensing genomic DNA molecules in the intracellular environment without signal loss or distortion.

4.3 Materials and method

The details of the experiment performed to achieve the objective-3 are explained in this section.

4.3.1 Synthesis of gold probes

An ultra-short pulse laser (Clark-MXR, Inc; IMPULSE Series femtosecond laser) was used to fabricate the gold probes. In the current experiments the 10303 nm wavelength laser was used circularly polarized with 17 W laser power. The gold probes were synthesized by using silicon wafers (100) with a thickness of 500 μm (University Wafers, USA) coated with gold (350 nm in thickness). The protocol was followed as described earlier [160].

4.3.2 Material characterization of gold probes

The physical characterization of synthesized gold probes was done by using a High-Resolution Transmission Electron Microscope (HRTEM), which reveals the size and morphology of quantum probes. To analyze the chemical composition of the synthesized gold probes, an Energy Dispersive X-ray (EDX) was used. X-ray Photo-electron Spectroscopy (XPS) was used to validate the altered gold phase in the gold probes. X-Ray Diffraction was performed to study the crystallinity of the gold probes.

4.3.3 Cell culture of cancerous and non-cancerous cells.

The cancerous cell lines of pancreatic cancer (ASPC-1) and lung cancer (H69) (ATCC, American Type Culture Collection) and non-cancerous cells of fibroblast (NIH3T3) were used for the successful study of DNA diagnosis. ASPC-1 and NIH3T3 cells were cultured in a similar manner, as explained earlier [160], [161]. H 69 cells were also cultured in T25 tissue culture flask, and the same protocol was followed, as explained by [162]. The cells were divided in the

ratio of 1:4 on reaching the 80% confluence. The cells were collected using Trypsin –EDTA solution, centrifuged at 800 rpm for 5 minutes to separate the cell pellet. The cell pellet was then re-suspended in the complete growth medium of respective cell lines. Cells were treated with the DNA quantum sensors in a petri dish with 3 ml of medium. The cell seeding density was maintained at 10^6 cells/mL.

The cellular uptake of gold sensors was analyzed using a Bio Transmission Electron Microscope (BioTEM). The cells were treated with quantum sensors for 24 hours. Further protocol was followed as described [162].

4.3.4 SERS sensing for detection of cancer

The cells were seeded with the gold probes with a complete growth medium for 24 hours. The treatment was stopped by removing the complete growth medium followed by the procedure explained [160], [162]. All the tests were achieved four times. The raw data were processed by using Spectrogryph 1.2 software. The processed spectra were then used to provide a comparison between SERS spectra of different cell types. All the statistical analysis was performed with an in-built set of the XLSTAT software ("Addinsoft (2019). XLSTAT statistical.). The PCA method provides an efficient way to represent the difference between the different cell types which are otherwise not significantly distinct from the raw SERS spectra. Later attaining the principal components (PC) the statistically different (P< 0.05) PCs were determined using a t-test [162].

4.4 Result and Discussion

This section explains the detailed analysis of the results achieved from the experiments performed.

4.4.1 Physical synthesis and material characterization of DNA Sensors

The quantum sensors were synthesized by a physical method using an ionic condensation process. Here tunable Yb diode fiber laser with a wavelength of 1030 nm under the nitrogen environment was used. The synthesis of the quantum DNA sensors follows the mechanism which previously has been explained by using different materials such as silicon [163]–[166].

Previous studies have used wet chemical synthesis or nanolithography for the synthesis of gold nanomaterial in the presence of different chemicals which results in the chemical toxicity. However, by using the physical laser synthesis method, quantum DNA sensors were synthesized right from the target eliminating toxic adulterations. The physical characterization of gold sensors by using the High-Resolution Transmission Electron Microscope (HRTEM) were evaluated. The synthesized gold sensors as shown in HRTEM images in Figure 4.1 are in a spherical morphology. The particle size distribution curve analyzed the size of synthesized spherical gold sensors shown in Figure 4.1 B. Figure 4.1 B shows the broader size distribution curve for particles synthesized in the nitrogen filed atmosphere. With this result, it was concluded that the synthesized particles are extremely small in size (2.3 nm). The HRTEM images presented in Figure 4.1 shows the presence of extremely small gold sensors.

Next evaluated the material chemistry of synthesized quantum DNA sensors by using X-ray diffraction (XRD), X-ray photoelectron spectroscopy (XPS) and Energy Dispersive X-ray (EDX). EDX analysis showed the comparative composition of gold, silicon, oxygen, carbon, and nitrogen in the synthesized quantum DNA sensors. By controlling the laser ionization energy, 5.7 % of gold concentration was achieved. The crystallinity of synthesized gold sensors was studied

by XRD spectra, shown in Figure 4.1 D. Quantum DNA sensors exhibited two major distinct peaks at 38.2 and 81, both the peaks correspond to Bragg reflection (111) and (222) of the lattice. The significant peak at 38.2 shows the ideal advance orientation of gold in (111) direction. Adding to this, the presented XRD pattern shows the pure form of gold sensors [167], [168]. Next, to confirm the presence of pure gold in the synthesized gold sensors the XPS analysis was performed. The XPS spectra presented in Figure 4.1 show the significant peaks at binding energies ~84 eV and 88 eV, which are associated with the purest form of gold [37]. Next to understand the stability of the physically synthesized DNA quantum sensors here sensors were treated with a growth medium with 10% fetal bovine serum (FBS) for 24 hours. To analyze the physical properties of DNA quantum sensors in CGM here the HRTEM images were studied and the hydrodynamic size was calculated. HRTEM images in Figure 4.1 F show that the treated DNA quantum sensors remain in the same size as the untreated sensors (~ 2.3 nm). Here the hydrodynamic diameter was calculated of the sensors by using the particle size distribution curve (Figure 4.1 B).
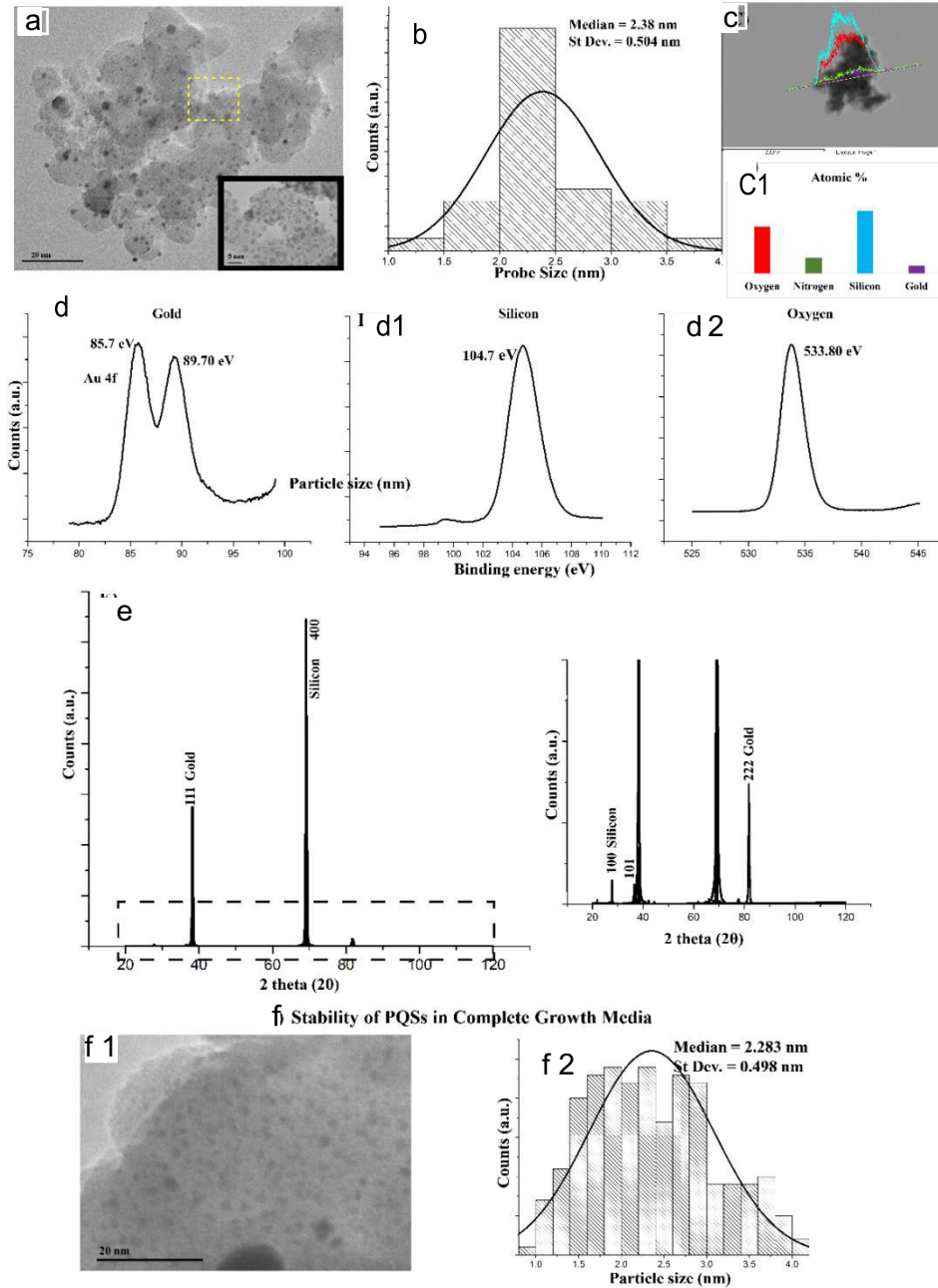
Figure 4.1 Physically synthesized DNA sensors characterization a) HRTEM images of 2.3 nm

sensors b) Size distribution of DNA quantum sensors c)-c1) Elemental composition of synthesized

DNA quantum sensors d)-d2) XPS analysis of physically synthesized DNA quantum sensors e)

XRD analysis of different plasmonic material phase f)-f2) Stability of physically synthesized DNA

quantum sensors after treating with complete growth medium

4.4.2 Nuclear uptake of DNA sensors

The internalization of nanoparticles inside the nucleus plays a vital role in medical applications, so it is crucial to study nanoparticle internalization and interaction with the cellular components in the live cell environment before consuming them for possible *iv-vivo* biomedical applications in the future. Nuclear internalization of gold sensors is a prerequisite for the sensing of nucleic acids in the cellular environment. The gold sensors must penetrate through the nuclear envelope to reach nuclear components. However, there is a significant barrier to the delivery of nanoparticle into the nucleus. The nuclear membrane has a double-layered nuclear envelope and contains biomolecules which have separate protein composition [169]. To quantum DNA sensors internalize into the nucleus (near DNA/RNA), the sensors must pass through the double-layered nuclear envelope [170]. The exclusive penetrability barrier of the nuclear membrane limits the dispersion of foreign biomolecules based on their molecular size [171]. Particles less than 5 nm can penetrate the nucleus, whereas particle larger than 5 nm must be engineered with nuclear targeting molecules in order to transmit the nuclear membrane [43], [172], [173].

Earlier researches have shown that there are two best-known pathways envisioned a) nanoparticles complexes labeled with lipid layers could react with the nuclear envelope and be internalized into the nucleus [174], b) nanoparticles penetrate the nuclear envelope through the nuclear pore that typically transports nuclear proteins [175]. Prior studies show particles less than 9 nm or coated with nuclear targeting molecules can enter and exit the nucleus through the nuclear pore complex by diffusion mechanism [43], [44], [171], [176]. Nanoparticles, such as PEG-modified gold nanoparticles (3.7 nm), can pass through the nuclear pore complex upon 24 hours exposure [170]. However, the toxicity of gold nanoparticles toward various healthy cell lines is high. The localization of gold nanoparticles (16-20 nm) within the nucleus increases the

DNA damage and leads to the double-strand breaks [130], [177]–[180]. In contrast, smaller gold nanoparticles (such as 3-5 nm)) are non-toxic [181]. It is desirable to synthesize gold sensors that penetrate the nuclear pore complexes and adhere to the nuclear component so that it enhances detection without causing cellular cytotoxicity. The sensors used for this study are physically synthesized by using laser ionization. They retain their quantum size and are non- toxic because they are free from the chemical residues.

Primarily the toxicity of physically synthesized gold sensors using two different cancer types, namely lung cancer (H69) and pancreatic cancer (ASPC-1), was evaluated. MTT analysis was performed to evaluate the effect of quantum DNA sensors on cell viability. Both cell types were treated to quantum DNA sensors for 24 hours. Untreated cells were used as control. Lung cancer cells exhibited no significant decrease in the cell viability as compared to the control after 24 hours of gold probe treatment. ASPC-1 cells did not show any significant decrease in cell viability either, as determined by the MTT assay [182].

The nuclear internalization of gold sensors inside the two different cancer types was studied, namely lung cancer (H69) and pancreatic cancer (ASPC-1). The results are presented in Figure 4.2. The extremely small size of the gold sensors (2.3 nm) allowed them to pierce inside the cell and through the bi-layered nuclear membrane easily. The average number of sensors internalized inside the nucleus is 162 in healthy cells, 123 in pancreatic cancer cells, and 154 in lung cancer cells. The gold sensors internalize inside the nuclear membrane by diffusion through the nuclear pore.
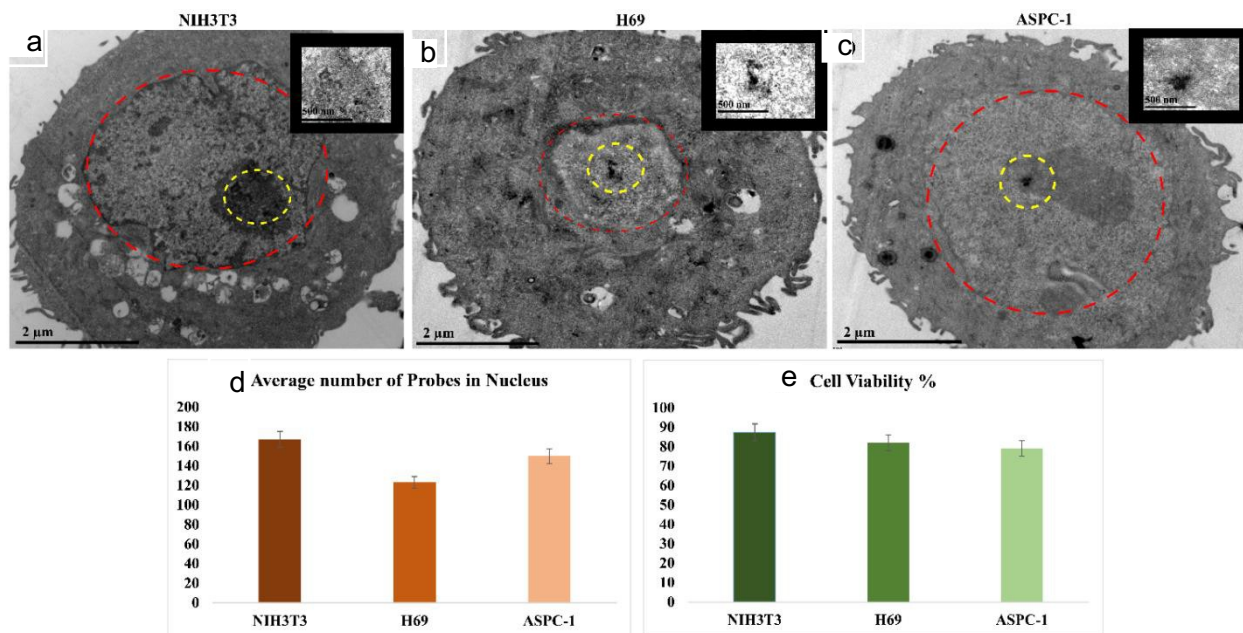
Figure 4.2 Biocompatible DNA sensors are internalized inside the nucleus a)-c) BioTEM images of NIH3T3, H69, and ASPC-1 respectively show the presence of DNA quantum sensors inside the cell and the nucleus d) the bar graph shows the presence of an average number of sensors inside the nucleus e) MTT analysis of NIH3T3, H69, and ASPC-1 to the study the biocompatible and non-toxic nature of DNA quantum sensors.

4.4.3 Intracellular SERS sensing of DNA

Existing SERS diagnosis method for DNA sensing requires DNA binding to functionalize nanoparticles [183]–[185]. Upon binding with an opposite strand of DNA, characteristically bound to other metal surfaces, the SERS fingerprint was collected [185]. The large size of the probe and complementary DNA molecules quickly get covered by the external protein layer, which weakens the formed DNA bonds with the metallic surface [186]. In other words, these probes lose their sensibility soon after feeding into the cell environment. Besides these probes

cannot pass through the nucleus membrane. Therefore, the genomic information is invisible to those traditional probes. Most of the Raman spectral features reported by earlier studies have been assigned to protein components and do not include features associated with DNA molecules.

In this work, the probes can reach into the nucleus and bind to DNA due to a very small size. Therefore, the Raman profiles obtained from this study include the complete information of genomic DNA. In other words the Raman spectra contain many signature fingerprints that can be specified to DNA molecular. This the first time DNA SERS fingerprints are observed in an intracellular environment without any labels and coatings.

A Raman with a laser wavelength of 785 nm was used for this study because it can easily penetrate the biological samples [109]. The SERS spectra obtained from this study are much more productive and more complicated compared to those obtained from prior research. SERS spectra contain information from multiple intracellular biomolecules and the nucleic acid. The rich information helps to understand the complete cellular mechanism.

Figure 4.3, the peak positions can be assigned to DNA and other intracellular biomolecules. Representative SERS spectra of genomic DNA from the lung cancer cell shows significant peaks at the wavelengths of about 732 cm^{-1}, 793 cm^{-1}, 1335 cm^{-1}, 1559 cm^{-1}, 1579 cm^{-1}, and 1647 cm^{-1} which are associated with poly adenine, poly cytosine/poly thymine, poly adenine vibrations, adenine bands, poly guanine and poly cytosine respectively [187]–[190]. Adding to this the DNA isolated from pancreatic cancer shows the strong signals at 1248/1285 cm^{-1}, 133 cm^{-1}, 1370 cm^{-1}, 1463 cm^{-1}, 1567 cm^{-1}, and 1635 cm^{-1} which are featured with cytosine, adenine/guanine, thymine, guanine, adenine and guanine respectively [183]. According to the SERS signals represented in Figure 3, the SERS signals of normal DNA showed strong signals for guanine

[155], [191], [192] whereas lung cancer DNA exhibited strong signals of adenine vibrations. Adding to this, the pancreatic cancer cells show a strong signal for thymine. The standard DNA mostly generates the peaks stated in Figure 3 for normal fibroblast DNA. The presented results in Figure 3 show that the H69 DNA is characteristically different from the NIH3T3 DNA. The peak associations and intensity of peaks are different for the different DNA molecules

The efficiency of DNA quantum sensors to enhance the intracellular SERS signals are presented in Figure 4.3. Figure 4.3 represents that all three distinct types of treated cells show the enhanced SERS signals of multiple cellular components. Significantly, protein enhancement such as peaks at 1330 cm^{-1} represents the CH deformation, 1546 cm^{-1} shows the sharp peak for tryptophan (Supplementary Table 1,2,3,4 and 5) is amplified when associated to DNA and RNA. This enhanced enhancement is attributed to the complex conformation of the protein molecules. However, the real challenge to sense the DNA molecules in the intracellular environment and the reason behind this difficulty is their minimal concentration. In this present study, it is evident that the pristine DNA quantum sensors internalize inside the nucleus without changing the cellular metabolism to amplify DNA with the single molecule sensitivity. The treated cells show a minimum of 700 folds of enhancement.

Previous researches have used multiple biomarkers for the SERS diagnosis of cancer to increase the accuracy of diagnosis. Each biomarker must be detected separately. To conduct a general diagnosis, multiple tests are required. Also these tests are mostly based on surface or cell biomarkers. Genomic information is less tapped due to the limitation of the detection method. Therefore, the accuracy of diagnosis is limited. Using quantum sized sensors sensing of multiple biomolecules can be done simultaneously. Results present the complete information of DNA molecules, biomarkers and the proteins in the intracellular environment. The present research is a

holistic approach for a diagnosis of the cancer cell, using genomic and biomarkers concurrently.

Therefore, a much more accurate diagnosis can be expected.
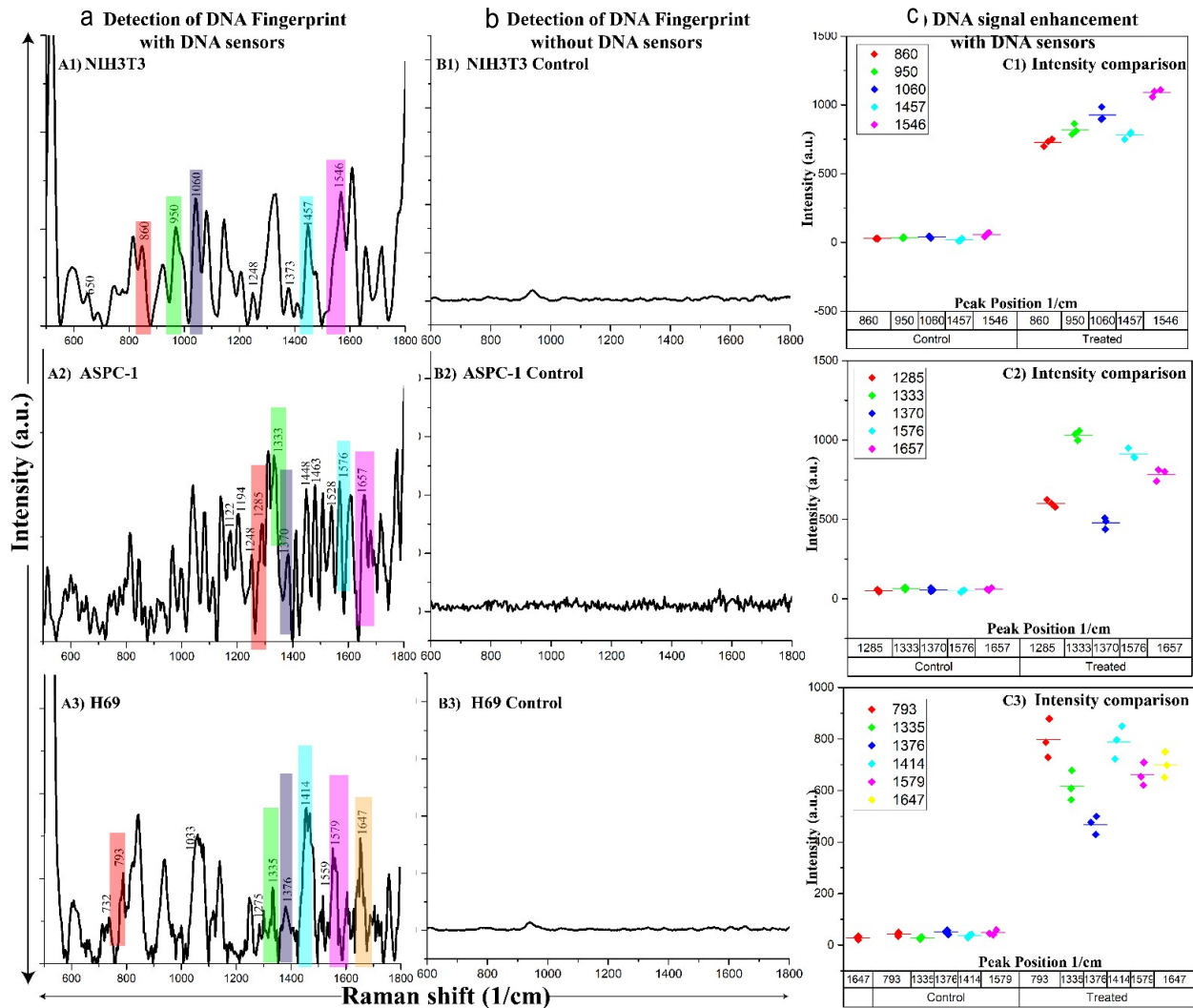
Figure 4.3 Intracellular sensing of DNA molecules in different cell types a) Detection of DNA Fingerprints with DNA sensors in the intracellular environment a1-3) Detection of intracellular DNA molecules in the presence of DNA sensors in three different cell types healthy fibroblast cells (NIH3T3), pancreatic cancer cells (ASPC-1) and lung cancer cells (H69) respectively. b) SERS detection of DNA fingerprint without DNA sensors in the intracellular

environment, b1-3) Detection of DNA molecules in the absence of DNA sensors in NIH3T3 cells, ASPC-1 cells, and H 69 cells, respectively. c) DNA signals based enhancement comparison of SERS signals to calculate the fold increase in the SERS enhancement, c1-3) NIH3T3 cell showed the minimum of 700 fold and a maximum of 1280 fold increase in the SERS enhancement, ASPC-1 cells showed a minimum of 500 fold and a maximum of 1150 fold increase in the SERS enhancement and H 69 cells showed a minimum of 700 fold and a maximum of 950 fold increase in the SERS enhancement of DNA molecules.

4.4.4 DNA based cell differentiation

Principal components analysis is the most frequently used analysis to understand the essential aspects of the collected data set. PCA creates loadings and score plots from the principal components of raw data. PCA signifies each SERS bands as a factor component of the intensity corresponding to each wavelength. The differentiation of cancerous and non-cancerous cells can be studied by using PCA and dendrogram analysis [159].

Figure 4.4 represents a PCA plot graph. Here 4 data points were applied for each of the ASPC-1, NIH3T3, and H 69 cells. Every dot in the plot shows one spectrum. The first-factor component (FC1) and second-factor component (FC2) disclose the pattern of the signals in each data set. The PCA analysis of ASPC-1, H69, and NIH3T3 cells shows a change of 64.79 % for FC1 and a 15.05 % change for FC2. The Scatter plot generated based on the FC scores shows three distinct clusters, corresponding to NIH3T3, ASPC-1, and H69 cells (Figure 4.4). Therefore, different cell types can be analyzed based on FC1 loading data. With the PCA plot, it can be interpreted that even though all the cell lines group to a certain extent, they act significantly different as the different type cancers are the opposite side of the quadrants shown in Figure 4.4 A. All the FCs obtained by decreasing the SERS signals presented to be statistically significant (P<0.0001) for

the differentiation of different cancer types. The data graph presented in Figure 4.4 A1 for FC1 shows the Raman shifts corresponding to the variations that result in the differentiation of different cell types shown in Figure 4.4 A1. Peak positions of factor loading represent the SERS signals. Figure 4.4 A1 shows the several slender peaks with positive values that presented the variance amongst the cell lines. FC loadings show significant peaks at 1060 cm^{-1}, 1257 cm^{-1}, 1285 cm^{-1}, 1370 cm^{-1}, 1463 cm$^{-1,}$ and 1647 cm^{-1} corresponds to guanine, Amide III, thymine, Ring Stretching, CN stretching (Thymine), CN s e CH b (Guanine) and Carbonyl stretching mode of poly C respectively. The difference in variance and signal position allows an evident dissimilarity among the different cell types. To validate the productivity of plasmonic DNA sensors to differentiate cell types, hierarchical clustering analysis was studied using the average spectra. The hierarchical clustering presented in Figure 4.4 B shows three well-parted clusters associated with fibroblast, lung cancer, and pancreatic cancer cells.
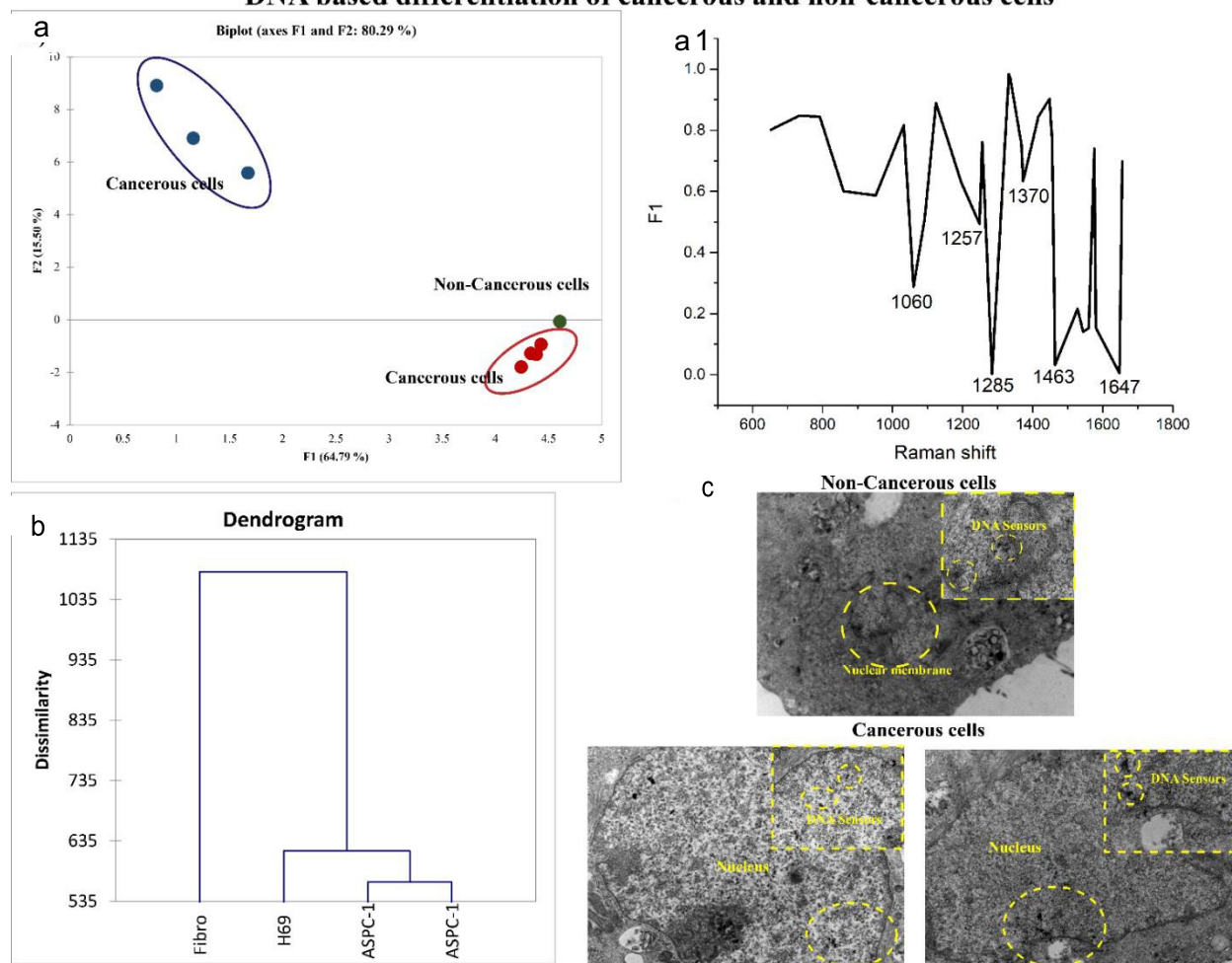
Figure 4.4 DNA based differentiation of cancerous and non-cancerous cells a) PCA analysis to differentiate different types of cells blue and red clustered dots shows the cancerous cells and green clustered dots presents the healthy fibroblast cells, a1) Factor component loading showing the SERS peak differences between cancerous and non-cancerous b) Hierarchical clustering analysis to differentiate cancerous and non-cancerous cells.

PCA analysis of pancreatic and lung cancer shows a variance of 55.10 % for FC1 and 24.35 % FC2. PCA graph in Figure 4.5 A infers that both the cancerous cells clusters act significantly differently. All the FCs attained from the SERS spectra revealed to be statistically significant (P < 0.05) for differentiating different cancer types. Figure 4.5 shows the factor loading of the two

main principal components that showed change between the cell lines. The data graph for FC1 shows many slender peaks with positive values (Figure 4.5, A1). As of Figure 4.5, it can be witnessed that the presence of at 950 cm^{-1}, 1090 cm^{-1}, 1248 cm^{-1}, 1285 cm^{-1}, 1370 cm^{-1}, 1559 cm^{-1}, and 1576 cm^{-1} corresponding guanine, PO$_2$ backbone, cytosine ring stretching, thymine, CN stretching of thymine, adenine bands and ploy guanine respectively. The dendrogram analysis for the diverse cell types to account for the dissimilarities of the different cell types was also studied. All three types of cells significantly form a distinct branch in the dendrogram (Figure 4.5 B).

By applying the dendrogram analysis, the variance between cell types and within the different cancer types was calculated. The percentage of the change between different cell types was found to be 19.49%, and the proportion of variance within the cancer cells was found to be 80.51%. Hence, it can be determined that the DNA quantum sensors can efficiently differentiate different cell types considering the diverse nature of the different cell types. The PCA analysis sheds light on the discrimination of the different types of cells down to the level of specific DNA peaks.

DNA based differentiation of Different cancer types
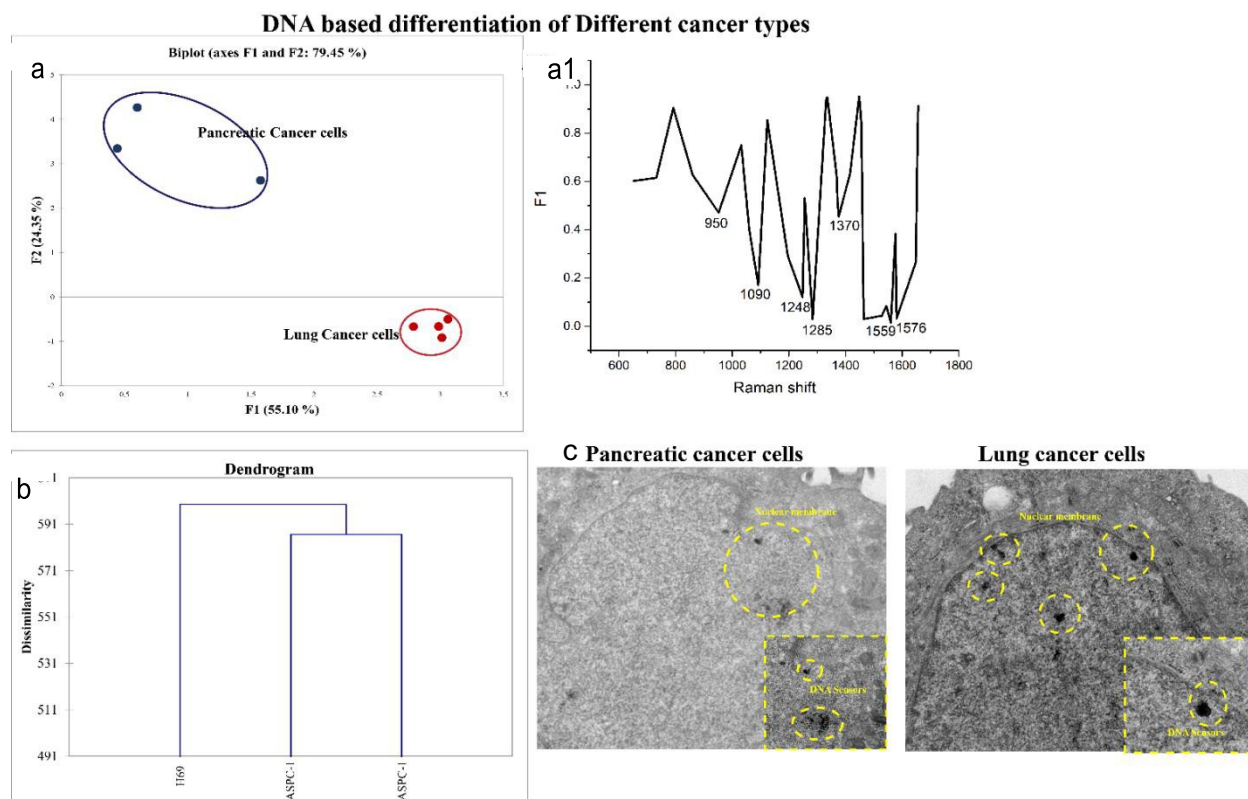
Figure 4.5 Statistical analysis to distinguish different cancer types. a) PCA scatter plot demonstrates the different clustering patterns for different cancer types, a1) Factor component loading showing the difference between different cancer types. b) Hierarchical clustering analysis (dendrogram) of different cancer types. c) BioTEM images show the internalized DNA sensors inside the nucleus.

4.5 Conclusion

The sensing of DNA molecules in the intracellular environment enhances the ability to detect and identify cell types. Till date the existing SERS sensing method is limited to the detection of extracellular DNA molecule or non-nuclear cell DNA with coated or ladled sensors. This study introduces a novel probe capable of sensing of intracellular DNA molecules. For the first time, un-tamped DNA sensors were used for the sensing of DNA molecules in the intracellular environment. The DNA quantum sensors internalize inside the cell by the endocytosis mechanism and inside the nucleus by diffusion mechanism. The presence of DNA quantum sensors inside the nucleus enhances the SERS signals by at least 700 folds and maximum by 1300 folds as compared to control. The probes were able to reveal the Raman fingerprint of DNA molecule in the complex intracellular/nucleus environment. Further, by using PCA and Hierarchical Clustering analysis, cancerous (pancreatic and lung cancer) and non-cancerous (healthy fibroblast) cells were differentiated. Adding to this, different types of cancerous cells (pancreatic and lung cancer) were also distinguished by using PCA and hierarchical clustering analysis. The presented method is a step forward in sensing the DNA molecule in the intracellular environment. This study holds promising potential for developing a new technique for accurate diagnosis of cancer-based on cell DNA detection.

Chapter 5

Small Gold Quantum Probes for drug-free Cancer Theranostics

5.1 Abstract

Gold quantum dots emerged as a distinct approach for cancer theranostics by using labeled and functionalized chemotherapeutic drugs to realize its detection and chemotherapeutic functions. However, the toxicity induced by chemical-based synthesis, their nonspecific accumulation in healthy tissues, and organs hamper its translation to clinical applications. Gold quantum dots (QDs) are functionalized/labeled with a layer of anti-fouling agents or bio-recognition ligands to reduce their toxicity and helps the QDs' cellular uptake. Besides this, labeling increases the overall hydrodynamic size of gold QDs, which limits the dispersion, impedes efficient renal clearance, and causes the accumulation of gold QDs in organs. Therefore, the unique properties that arise from gold quantum size (less than 5nm) are lost. By far, reports on the effect of real gold quantum size on cell interaction are limited, if any. Small-sized label-free pristine gold quantum dots may hold the solution to break this roadblock. In this study, the concept of small- sized self-functionalized pristine, bright quantum gold probes (BQGPs) for cancer theranostics is presented. To the finest of our understanding, it is the first time cell interaction of pristine quantum gold was investigated, and the results suggest that it can be used for inorganic (label- free drug-free) cancer quantum-theranostics. Here, by using multiphoton ionization (physical synthesis), non-toxic BQGPs were synthesized without chemical contamination and eradicated the requirement of labeling. Since the BQGPs are free from labels, they remained in small quantum size in theranostics application, enabling the investigation of the exact quantum effect

in cell interaction. The pristine BQGPs demonstrated cancer-selective cell uptake, enabling dosage-dependent fluorescent detection/differentiation of cancerous cells and cancer-selective cytotoxicity. The small quantum-sized BQGPs facilitate a new concept of inorganic cancer quantum-theranostics. The fabricated BQGPs demonstrated fluorophore-free fluorescence illuminance at a broad range of excitation wavelengths and drug-free cancer-specific treatment. According to this study, the as-fabricated BQGPs have dual functions of fluorescent diagnosis and treatment of cancerous cells. Moreover, the drug-free gold quantum dots may find advantages in fighting drug-resistant cancers.

5.2 Introduction

Nano-theranostics is a new concept of cancer drugs. It refers to an all-in-one medicine that can perform therapy and diagnosis simultaneously. In other words, using a single nano-material to target, image, diagnose, and treat cancer cells. Gold nanoparticles, due to their excellent optoelectrical and biological properties, have gained particular attention for theranostics application purposes [3], [193]–[195]. Gold nanoparticles of various forms and compositions have been investigated for spectroscopic imaging, fluorescent imaging, computed tomography (CT), photoacoustic imaging and photodynamic therapy[4], [6], [194], [196]–[199]. To improve cell-specific targeting, the sensitivity of detection, and reduce cytotoxicity, the gold nanoparticles are coated with molecules of functional groups[97], [200].

In the last decade, gold quantum dots attracted tremendous research interest since their excellent physicochemical and optoelectrical properties hold the potentials of improving specificity, accuracy, and sensitivity of early cancer detection[8]. Gold quantum dots, having a size comparable to biomolecules, are capable of deciphering the mechanism of cancer invasion and progress at the molecular level. Also, multiple different labels, ligands, and a biomarker can be

attached to a single gold quantum dot simultaneously, making multiplex molecular detection possible[97], [177], [201]–[203].

So far, within the applications of theranostics, quantum dots are mostly playing the role of vehicles for drug transportation [204]–[206] and dispersion. Gold QDs themselves have no or minimal function in detection and treatment, except in photothermal therapy[198] where gold particles are used for photo-thermal energy conversion. Fluorescence imaging is mostly used to monitor the uniformity of drug release and drug effects and is significant for visualizing the cellular activity and expression of cancerous tissues and markers[207], [208], by using specific fluorophore dye labels. In recent years, labeled and functionalized gold quantum dots have been employed to enhance fluorescence imaging cancer detection. [209]. The quantum dots are conjugated with specific fluorophores to increase the life span of the dye as well as reduce fluorescence quenching [210]. The gold quantum dots are used to carry and disperse the fluorophores, and itself does not contribute to the fluorescent emission. The significant challenges of using fluorophore have not been addressed with the addition of gold quantum dots. For instance, fluorophores degrade over time in the presence of biochemical molecules in the tissue, leading to reduced signal intensity, and fluorophores are only sensitive to specific wavelengths, limiting their clinical applicability.

Due to their small size, gold quantum dots have better access to tumor sites as compared to conventional drug carriers. The gold quantum dots have a unique ability to permeate and accumulate within the tumor. Gold quantum dots employed in most cancer research have a size of around 20 nm [104]. Recent research indicates that small-sized gold quantum dots (less than 5 nm) behave distinctively different from that of larger sizes, providing more exciting new possibilities than the larger ones[97]. Gold quantum dots show size-dependent permeation within

biological systems, especially concerning cellular and organ uptake [10], [26], [92]–[96]. For instance, brain microvasculature permeation of PEG-AuNPs shows that 4nm core SIZE led to the optimum result. The transport and kinetic profile of a 4 nm gold core is substantially different from those of its large-sized (>15nm) counterparts[97]. Gold quantum dots usually more readily cross barriers[92]. It is particularly true for small gold quantum dots. Hillyer showed that particles smaller than 5 nm have density several times higher inside tissue than those larger ones[143].

Gold quantum dots offer unprecedented opportunities in cancer theranostics. However, the toxicity induced by their nonspecific accumulation in healthy tissues and organs hampers its translation to clinical applications. Small-sized gold quantum dots may hold the solution to break this roadblock. Multiple research has demonstrated that the renal clearance of hard inorganic nanoparticles is closely affected by the size and surface charge of nanoparticles [211], [212]. Quantum dots with a size smaller than 6 nm can be cleared into the urine with much higher efficiency than the ones larger than 8 nm. However, current research in this front is quite limited because gold quantum dots are functionalized with a layer of anti-fouling agents (like PEG) or bio-recognition ligands (e.g., peptides, antibodies or markers) to increase the specificity of nanoparticles to cancer cells for better dispersion. The addition of a layer increases the hydrodynamic size of nanoparticles and prevents the retention of nanoparticles by excretory organs, which potentially leads to organ failure due to the high-level accumulation of gold nanoparticles in the liver and spleen.

In addition to the above-mentioned biological properties, small-sized quantum dots offer better optical and electrical properties than large ones due to the quantum confinement effect, leading to molecular level accuracy, unprecedented sensitivity, stronger signal, better image contrast, and

multimode detection. Few existing pieces of research showed that small-size quantum dots enabled a new detection function [164].

In short, small-sized quantum dots behave very differently than their larger counterparts and are worthwhile to be investigated separately. Although *in vivo* targeting, imaging and treating are rapidly growing, the use of gold quantum dots is still challenging because of the comparatively large overall size due to labeling. The gold particles at the quantum scale can act as a chemical catalyst, which can source unwanted chemical reactions/side effects in the biological system, such as oxidative stress and mitochondrial damage [6], [213]–[215]. The toxicity of gold quantum dots majorly comes from wet-chemical synthesis. During the wet-chemical synthesis, such as cetyltrimethylammonium bromide (CTAB) synthesis, there is a formation of CTAB bilayer on the surface of gold quantum dots which induce cytotoxicity[216], [217]. Almost all the researchers and clinicians use a layer of polyethylene glycol (PEG)[97] to formulate the gold quantum dots to control the toxicity and improve specific cell uptake, thus increases the overall size of quantum dots and results in reduced internalization and permeation. Therefore, the unique properties that arise from quantum size (less than 5nm) are lost. By far, reports on the effect of real quantum size on cell interaction are limited, if any.

In this work, small-sized bright quantum gold probes (BQGPs) are synthesized by physical means, which leaves no residual chemicals and eradicates the requirement of PEG labeling. The pristine BQGPs demonstrated cancer-selective cell uptake, enabling dosage-dependent fluorescent detection/differentiation of cancerous cells and cancer-selective cytotoxicity. The small quantum-sized BQGPs facilitate a new concept of label-free drug-free cancer theranostics.

As BQGPs reach the small quantum scale, they exhibit a unique self-mobilization phenomenon by an energy-independent passive uptake pathway. Also, unlike traditional aggregation of gold

quantum dots, unique dispersion of BQGPs all over the cells, including the nucleus was seen. In the present study, lung, pancreas, breast, and cervical cancer cell lines were selected due to their metastatic and multidrug resistance ability. Different cancerous and non-cancerous cells have shown distinct internalization of BQGPs based on different probe sizes and thereby exhibiting the different fluorescence excitation wavelengths (525-655 nm). Besides, the unique internalization of BQGPs, not only distinguish between cancerous and non-cancerous cells but can also differentiate cancer types due to distinguishable fluorescent intensity. Additionally, the as-made BQGPs act as a drug without conjugation/functionalized chemotherapeutic drugs. At a specific concentration, cancerous cells internalize several times more BQGPs than non- cancerous cells. This result implies dose-dependent cancer-selective cytotoxicity of BQGPs. Therefore, the self-functionalized BQGP is a single quantum material that can diagnose and treat the cancerous cells simultaneously *in vitro*. Furthermore, the as-made BQGP, free of coatings, could allow us to treat drug-resistant cancers and minimize the side effect of overdose.

5.3 Material and Methods

The details of the experiment performed to achieve the objective-4 are explained in this section.

5.3.1 Synthesis of pure quantum Gold probes by using ultra-short femtosecond laser

High-quality undoped silicon wafer with a crystallographic orientation of 100 with a thickness of 500 μm coated with 350 nm thick layer of gold (University Wafers, USA) was used. After cutting the wafer into 1.5 cm^2 square-shaped samples, the samples were cleaned with 100% ethanol. To synthesize the quantum Gold probe, the samples were irradiated by ultrashort femtosecond pulse laser (Clark-MXR, Inc.; IMPULSE Series ultrashort pulse laser). This laser system is proficient in generating the central wavelength of 1040 nm with varied pulse width

ranging from 214 to 1428 fs and with different laser beam ionization, which varies from 4 MHz (highest ionization energy) to 26 MHz (lowest ionization energy). The gold-silicon samples were therefore exposed at the laser's focal point, and a Galvano scanner was used to control the synthesis process. A single-step femtosecond laser ablation process synthesized the quantum Gold probe. For the present study, the laser parameters were standardized to the pulse width of 214 fs with the highest ionization energy (4MHz) to achieve the quantum size structure to maximize the concentration of gold.

5.3.2 Characterization of the synthesized quantum Gold probe

A High Resolution Transmission Electron Microscopy (HRTEM) (JEOL JEM-2010) was used to determine the morphology and size of the synthesized quantum Gold probe. To confirm the quantum size of the synthesized quantum Gold probe, UV-vis spectroscopy was done. Energy-dispersive X-ray spectroscopy (EDX) (Hitachi SU8200) was performed to evaluate the elemental composition of gold, silicon, and oxygen in the synthesized quantum Gold probe. To confirm the relative quantities and chemical state of gold, silicon, and oxygen X-ray, photon spectroscopy was performed. Photoluminescence spectroscopy (PL spectra) was performed to extrapolate the fluorescent nature of the quantum Gold probe.

5.3.3 Stability analysis of synthesized Gold probes

The gold probes were treated with three different solutions (serum, Phosphate buffer saline (PBS) and cell-culturing medium) for 24 hours, and HRTEM was used to determine the morphology and size of treated gold probes. To confirm the material chemistry and state of gold, X-ray photon spectroscopy was performed.

5.3.4 Cell culture cell seeding on a quantum Gold probe

All four cancerous cell lines, MDA-MB 231, HeLa, H69, and ASPC-1, and one non-cancerous cell line, NIH3T3 (ATCC, American Type Culture Collection) were used to achieve the relative therapeutic study. H69 cells were cultured in a T25 culture with Roswell Park Memorial Institutes (RPMI) 1640, 20% Fetal Bovine Serum (FBS), 1% antibiotic, and antimycotic solution (complete growth medium). HeLa and ASPC-1 were cultured in a T25 flask with RPMI 1640 with 10% FBS, 1% antibiotic and antimycotic solution. MDA-MB 231 and NIH3T3 cells were cultured with Dulbecco's Modified Eagle's Medium (DMEM) with 10% FBS, 1% antibiotic, and antimycotic solution. The flasks were maintained in a sterile incubator with 5% CO_2. The synthesized quantum Gold probe was sterilized under UV light for 15 min before seeding the cells. The cells were seeded on top of the tag-free quantum Gold probe for fluorescence microscopy and Bio TEM samples.

5.3.5 ROS quantification inside cancerous cells by flow cytometry

After 24 hours of cancerous and non-cancerous cell seeding on top of the tag-free quantum Gold probe, cells were collected and stained with 2', 7'- dichlorofluorescein diacetate (DCF-DA), followed by the flow cytometry analysis by using FACS Calibur flow cytometer (BD Sciences). Here the ROS generation was measured by using DCFH-DA, a non-fluorescent dye. Upon cell treatment with DCFH-DA, intracellular esterase cleaved it to dichlorofluorescein (DCF), which on oxidation emits fluorescence by free radicals.

5.3.6 Measurement of mitochondrial membrane potential disruption

The cancerous and non-cancerous cells were seeded with the bare tag-free quantum Gold probe for 24 hours. Cells were pelleted and tainted with JC-1 dye, as instructed in the Abnova procedure. The MMP was quantified by flow cytometry analysis.

5.3.7 Annexin-V and PI double staining apoptosis assay

The cancerous and non-cancerous cells were collected after 24 hours of drug-free BQGPs treatment and were used for apoptosis analysis using FACS. The cells were prepared for FACS analysis by following the instructions provided by BD Biosciences.

5.3.7 Cell adhesion study by SEM imaging and EDX analysis

The cell adhesion was observed by using the Scanning Electron Microscopy (Hitachi, SU-1500). For this, the 3 million cells were seeded on the top of the 3D Janus biosensors chip for 6 and 18 hours. After that, the medium was removed, and the cells were fixed with alcohol dehydration and critical freeze point drying process for SEM analysis. Images were acquired at a standard scale bar of 500 µm to 100 µm with an acceleration voltage of 3 kV and probe current of 60 to 70 µA.

5.3.8 Statistical analysis: Data presented as ±SD HRTEM. All the experiment was performed three times for each statistical analysis. The presented data were analyzed by using one-way ANOVA. In all the experiments, significance was defined as $p \leq 0.05$. Statistical analysis was conceded using Microsoft excel and origin 2016.

5.4 Results and Discussion

This section explains the detailed analysis of the results achieved from the experiments performed.

5.4.1 Physical characterization of synthesized pristine Bright Quantum Gold probes

The laser synthesis of pristine BQGPs was explained in detail in the supporting information (Note 1). The synthesized structures show the presence of BQGPs and a rough silicon substrate, where BQGPs are used for drug-free cancer theranostics, and the nano silicon substrate provides the structural support of the cells to proliferate.

Physical characterization of synthesized Quantum gold probes was carried out by using a Scanning Electron Microscope (SEM) and High-Resolution Transmission Electron Microscope (HRTEM). HRTEM imaging was performed to study individual BQGPs. The quantum gold probes synthesized by an ultrashort femtosecond laser vary in size, depending on the ionization energy of the laser beam. Figure 5.1) reveals the different sizes of BQGPs within the silicon structures. The BQGPs size distribution curve of BQGPs was studied by ImageJ software, which shows the median size of 3.28 nm with a standard deviation of ± 1.7nm. It was observed that at high laser ionization energy (low repetition rate of the laser beam), the probe size of BQGPs was reduced whereas, at low ionization energy (high repetition rate of the laser beam), the probe size was increased. Also, for morphological analysis of gold quantum probes, high-resolution TEM images show the spherical and hexagonal morphology of the probes. However, the nano silicon particles which act as a rough substrate where gold quantum probes are loosely attached and show distorted morphology showed in Figure 5.1(c & d).
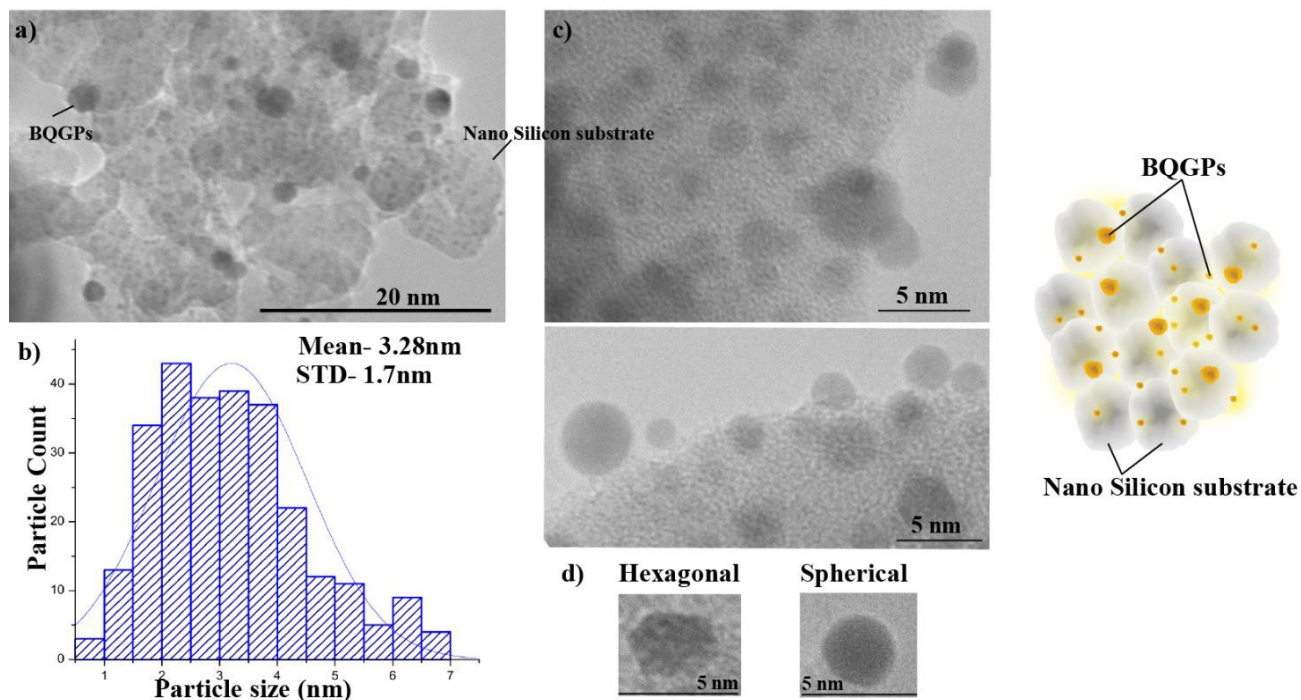
Figure 5.1 a) HRTEM images illustrating the presence of quantum gold probes and their morphology b) Particle distribution curve for the quantum probes c) & d) Shows the morphology of the synthesized quantum gold probes

5.4.2 Chemical analysis of synthesized pristine BQGPs

Furthermore, to determine the chemical characterization of quantum probes, here, EDX analysis, XPS analysis, and UV-vis and PL-spectroscopy were used. The relative proportion of silicon, gold, and oxygen present in the Quantum Janus probe was tested by the Energy Dispersive X-ray spectroscopy (EDX). By tuning the frequency of the laser beam, the maximum concentration of silicon was 32%, whereas the maximum concentration of gold was 12.29%. Characterization was done by using X-ray Photon Spectroscopy (XPS) presented in Figure 5.2. The XPS spectra show that the synthesized silicon sensor peaks at binding energies of 102 eV (Si2p3) and 103.5

111

eV (Si2p1), which depicts the presence of silicon and silica, respectively. The BQGPs peaks at binding energies of 85.05 eV, 87 eV and 89 eV, corresponding to the Au4f7, Au4f5 and Au4f phases respectively [218]. The first phase indicated a gold oxide of Au_2O_3, while the last two phases pointed to the purest form of gold, which was chemically stable and biocompatible [37]. Also, the optical characterization was done by using Photoluminescence (PL) spectroscopy, and UV-Visible Spectroscopy represented in Figure 5.2. The UV-vis spectra in Figure 5.2 reveals the active absorption attribute of BQGPs. The synthesized BQGPs show the multiplex emission due to their different quantum sizes at multiple wavelengths (310nm, 460 nm, 565nm, and 615nm). When the BQGP absorbs a photon, it enters an excited state and returns to the ground state by emitting a lower energy photon, with the difference in energy of the absorbed and emitted photon. This generates the fluorescence (Figure 3.2). Figure 5.2 presents the photoluminescence (PL) spectra of the BQGPs. The BQGPs showed strong PL with respect to the excitation wavelength. The emission at a longer wavelength and hence lower intensity demonstrated the fluorescence excitation of the BQGPs; notable broad absorption and narrow emission. As the excitation wavelength increased, the emission shifted towards a longer wavelength. The Quantum Janus probe consists of fused BQGPs with size variation of 2 nm - 5 nm, broader absorption and a subsequent wider range of emission were achieved. Adding to that, because of the unique size variation of BQGPs and a broad range of fluorescence excitation, BQGPs for the fluorescence excitation and differentiation were focused.

Adding to that, BQGPs in different solutions (Cell-culturing medium, Phosphate Buffer Saline (PBS), and serum) were also studied. The HRTEM images and particle distribution curve (supporting Figure S3 and S4) show that the BQGPs are stable and retain their hydrodynamic

size (3.2 nm) in a different solution. Detailed discussion was provided in supporting information Note 2.
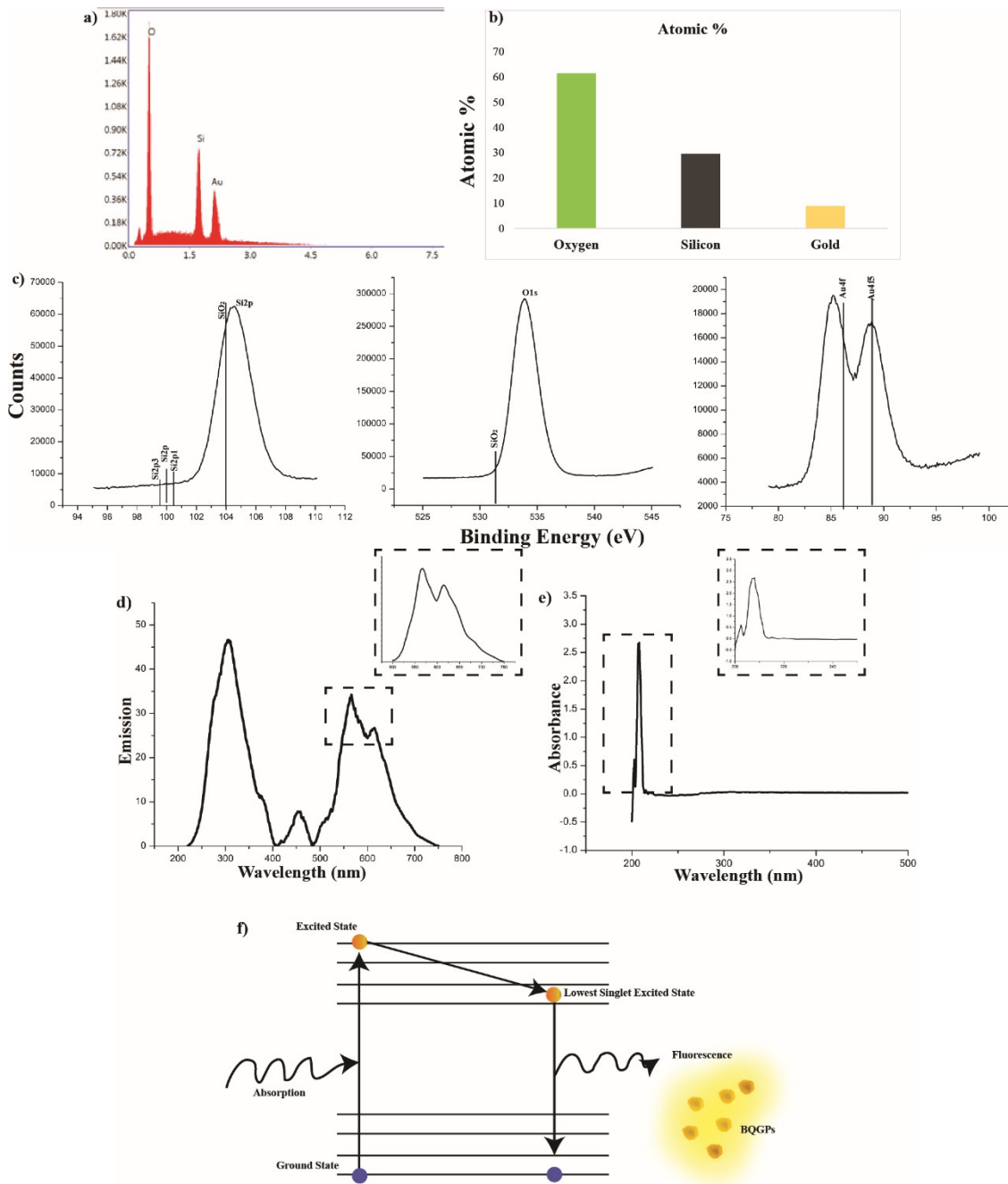
Figure 5.2 a) Elementary analysis of synthesized quantum gold probe b) Quantification of quantum gold elementary composition c) XPS analysis of synthesized Quantum gold d)

Photoluminescence spectra (excitation) shows the excitation of BQGPs at 310nm, 460 nm, 565nm, and 615nm e) the UV spectra (emission) shows the emission of BQGPs f) Schematic illustration of fluorescence mechanism of BQGPs

5.4.3 Variation in fluorescence intensities of label-free quantum gold in cancer and non-cancerous cells

Previous researches have shown that QDs demonstrate its increased stability and excellent optical properties on its own[219]–[222]. Gold QDs are highly photostable due to their inorganic composition, rendering them less susceptible to photobleaching and providing them with significantly longer fluorescent lifetimes compared to traditional fluorophores. This ultimately allows for the long term, repeated imaging [223]. However, the previously used QDs are toxic and require the labeling, which increases the overall hydrodynamic size and hinders the fluorescence and uptake of QDs [224]. So to overcome these issues here synthesized pristine BQGPs, it shows unique internalization inside the cells and emits the fluorescence at a broad range of wavelengths (310nm, 460 nm, 565nm, and 615nm) because of the unique series of different sizes.

The unique internalization of the BQGPs was explained in detail in supporting information (Note 2 and Supporting Figure S7).

Here the pristine BQGPs internalize inside the cells and electrostatically interact with the cellular components, which emits the fluorescence under a broad range of wavelengths [225]–[227]. The fluorescence intensity generated by the interaction between quantum gold and cellular components is directly proportional to the average number of quantum gold internalizes inside the cells as the number of quantum gold increases the fluorescence intensity increases. By using

this concept, cancerous and non-cancerous cells were differentiated, shown in Figure 5.3. The BQGPs show the increased internalization in the cancerous cells as compared to the non- cancerous cells, which results in the differentiation of cancer and non-cancer type based on generated fluorescence intensity. Figure 5.3 shows that the fluorescence of tag-free quantum gold is lightened up only in a tumorous microenvironment. However, the intensity of fluorescence generated inside the cells depends on the presence of an average number of pristine BQGPs.

The unique internalization of BQGPs not only distinguish between cancerous and non-cancerous cells but also differentiate cancer types due to distinguishable fluorescent intensity. With the unique cell-selective uptake, pristine BQGPs also show the size-dependent internalization inside the different types of cancerous cells. Results show that the tag-free quantum gold demonstrates fluorescence under different wavelengths. Figure 5.4 displays the fluorescence intensity of cancerous cells under four different wavelengths (310nm, 460 nm, 565nm, and 615nm), which then shows the broadband fluorescence property of the synthesized tag-free quantum gold. The synthesized quantum gold displays the fluorescence at different wavelengths simultaneously, which is consequently due to the different quantum sizes of gold present in the same condition. Figure 5.3 shows the particle distribution curve for the different cancerous cells, where breast cancer cells show the uptake of BQGPs of 2.3 nm, cervical cancer cells show the maximum uptake with 3.5 nm BQGPs and BQGPs of 3.7 nm shows the maximum uptake in pancreatic cancer cells. Due to the different size uptake mechanisms, different fluorescence intensities in different cancer types were seen, which result in the differentiation of distinct cancer cells.

Until now, different fluorophore was required for each different wavelength, however here, the synthesized tag-free gold probes that have different size variation results in different fluorescence excitation. It makes it more convenient to detect and distinguish the cells under

different fluorescence wavelengths without the need for multiple fluorophores. Thus, synthesized quantum gold, exhibit properties well-suited for the classification of cancerous and non- cancerous cells without the requirement of tags and functional groups attached. The high brightness and photostability of synthesized tag-free quantum gold enable the sensitive and robust classification of cancer and non-cancer cells.
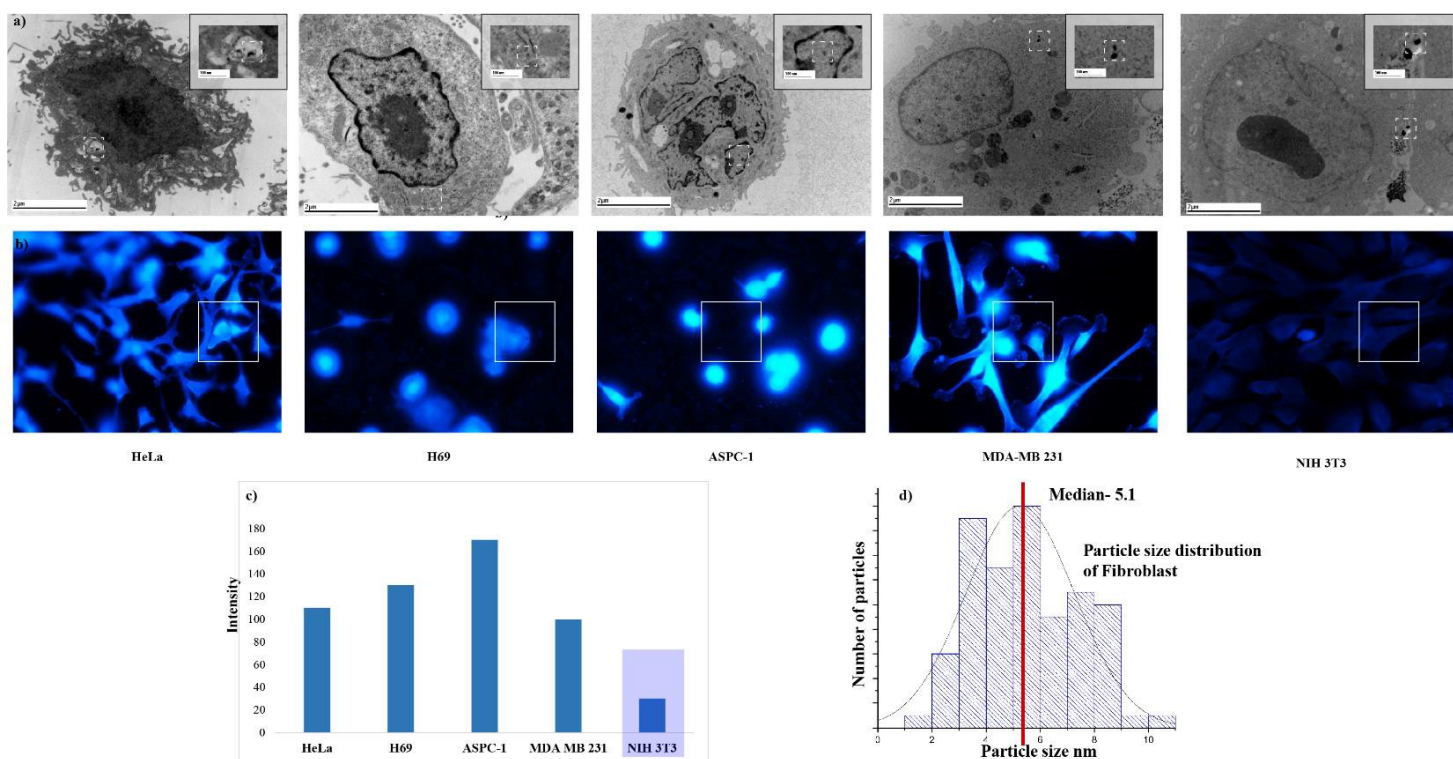
Figure 5.3 Differentiating cancerous and non-cancerous cells based on fluorescence intensity generated by bright quantum gold probe a) Bio-TEM images of cancerous and non-cancerous cells after 24hours of cells seeding which shows the presence of bright quantum gold probe inside the cancerous cells and outside the non-cancerous cells b) Fluorescence images of cancerous and non-cancerous cells treated with bright quantum gold probe c) Quantified fluorescence intensity for different cancerous and non-cancerous cells d) Probe distribution curve of bright quantum gold probe present inside fibroblast cells
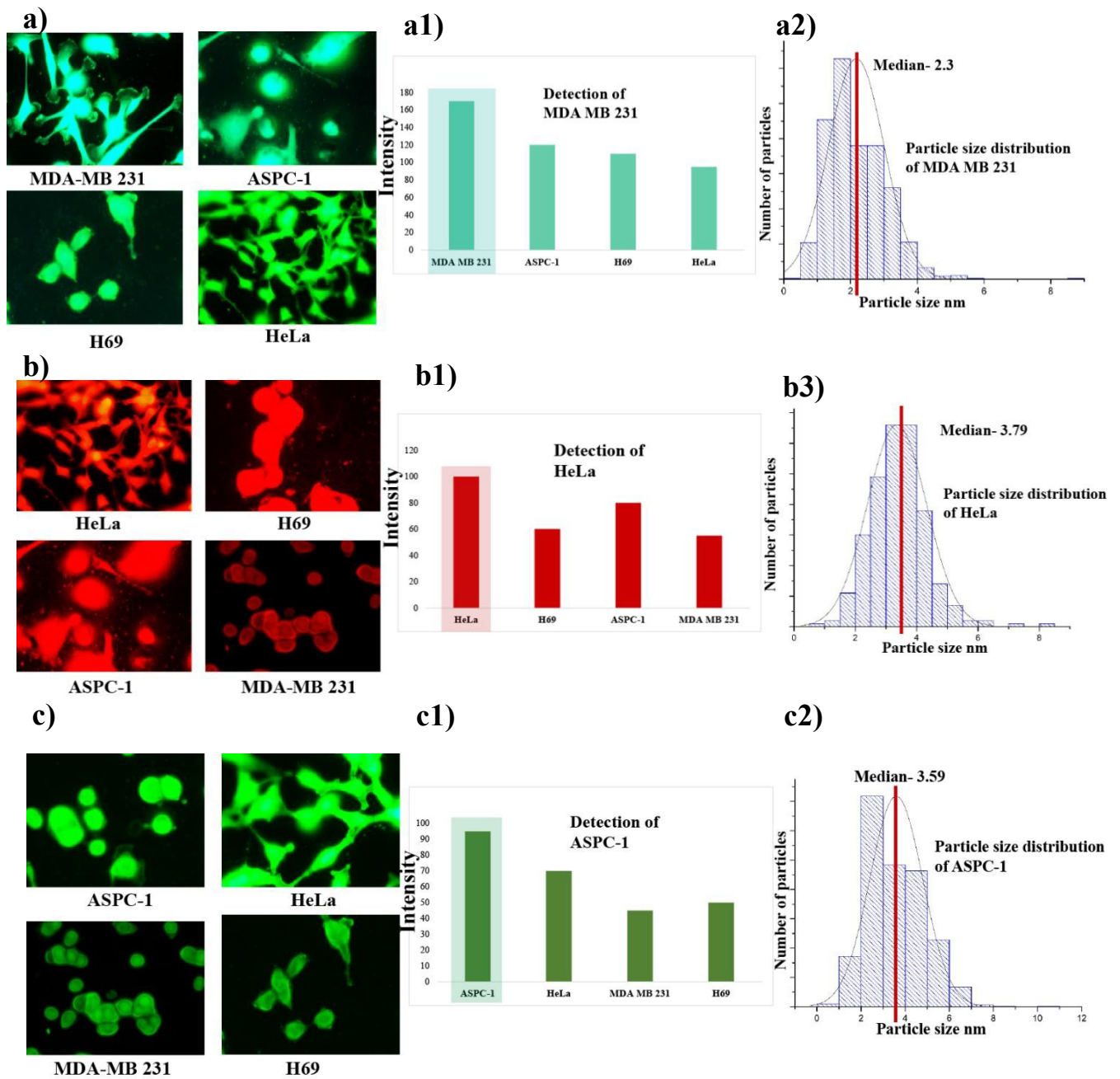
Figure 5.4 a) Detecting breast cancer cells (MDA MB 231) based on different fluorescence intensity at 460 nm wavelength a1) Quantification of fluorescence intensity at 460 nm wavelength a2) Probe distribution curve for bright quantum gold probe present inside MDA MB- 231 b) Detection of cervical cancer cells (HeLa) based on different fluorescence intensity at 615 nm wavelength b1) Quantification of fluorescence intensity at 615 nm wavelength b2) Probe

distribution curve for bright quantum gold probe present inside HeLa c) Detecting pancreatic cancer cells (ASPC-1) based on different fluorescence intensity at 565 nm wavelength c1) Quantification of fluorescence intensity at 565 nm wavelength c2) Probe distribution curve for bright quantum gold probe present inside ASPC-1 Data presented as ± mean, n=3

5.4.4 Generation of reactive oxidative stress (ROS) inside the cancerous cells

In order to determine the generation of ROS in treated cancerous cells plays a role in cell apoptosis, flow cytometer assay was used to quantify the ROS in cancerous and non-cancerous cells.

In this study, four different cancerous cell lines (MDA-MB 231, HeLa, ASPC-1 and H69) and one non-cancerous cell line (NIH3T3) were treated with drug-free quantum gold and incubated for 24 and 48 hours. The results showed that the treatment with drug-free quantum gold significantly increased intracellular ROS production only in the cancerous cells, as seen in Figure 5.5. After 24 hours of treatment, ROS generation in the cancerous cells increased by 42.5%, respectively, in comparison to the non-cancerous cells. The results presented in Supporting Table 1, showing the high concentration of ROS in cancerous cells treated by drug-free quantum gold, were consistent and repeatable throughout numerous experiments. Subsequently, ROS production in the cancerous cells treated with drug-free quantum gold was significantly higher than the non-cancerous cells.

The non-uniform response of cancerous and non-cancerous cells towards quantum gold is attributed mainly to the non-uniform uptake of quantum gold by cancerous and non-cancerous cells. Gold probes internalize in the cells as well as inside the mitochondria (which is the powerhouse of the cell and primary source of reactive oxidative stress) [214], [228], [229]. The

presence of gold probes inside the mitochondria alters the electron transport chain (ETC), which maintains the balance of free radicals, ions, and unpaired electrons for regular cellular metabolism. Alteration in ETC leads to increased production of reactive oxidative species, which amplifies the reactive oxidative stress as compared to normal conditions. ROS is generated by the radicals, ions, or molecules that have an unpaired electron in their outermost shell. Regardless of the many pathways existing for ROS generation, the mitochondrial generation of ROS is the prime mechanism via the electron transport chain [230]. The ROS production in cells targeted by quantum gold was observed by using a marker of ROS, a cell-permeable green dye that fluoresces upon the oxidation by ROS generation [231], [232].

Generally, in cancer cells, the increased metabolic activity, mitochondrial dysfunction, and increased activity of oxidases in cell cytoplasm result in a high level of ROS [233]. Gold nanoparticles usually catalyze nitrogen monoxide through the formation of AU-thiolate on the surface of nanoparticles, which increases the production of ROS.[234] Previous studies have shown that the generation of ROS by gold nanoparticles upon 4 hours of exposure can be counterbalanced by cells. However, 24 hours of exposure can overwhelm antioxidant defenses.[235] So, the higher level of ROS generation in cancer cells after 24hours of cell seeding is partially due to the ROS produced by drug-free quantum gold that damages the mitochondria. This mitochondrial destruction ultimately leads to the opening of pores on the mitochondrial membrane, followed by the electric charge shift of the mitochondrial membrane potential and additional ROS generation. Higher concentrations of ROS and a prolonged pore opening duration on the mitochondrial membrane may lead to the destruction of the mitochondria [232].
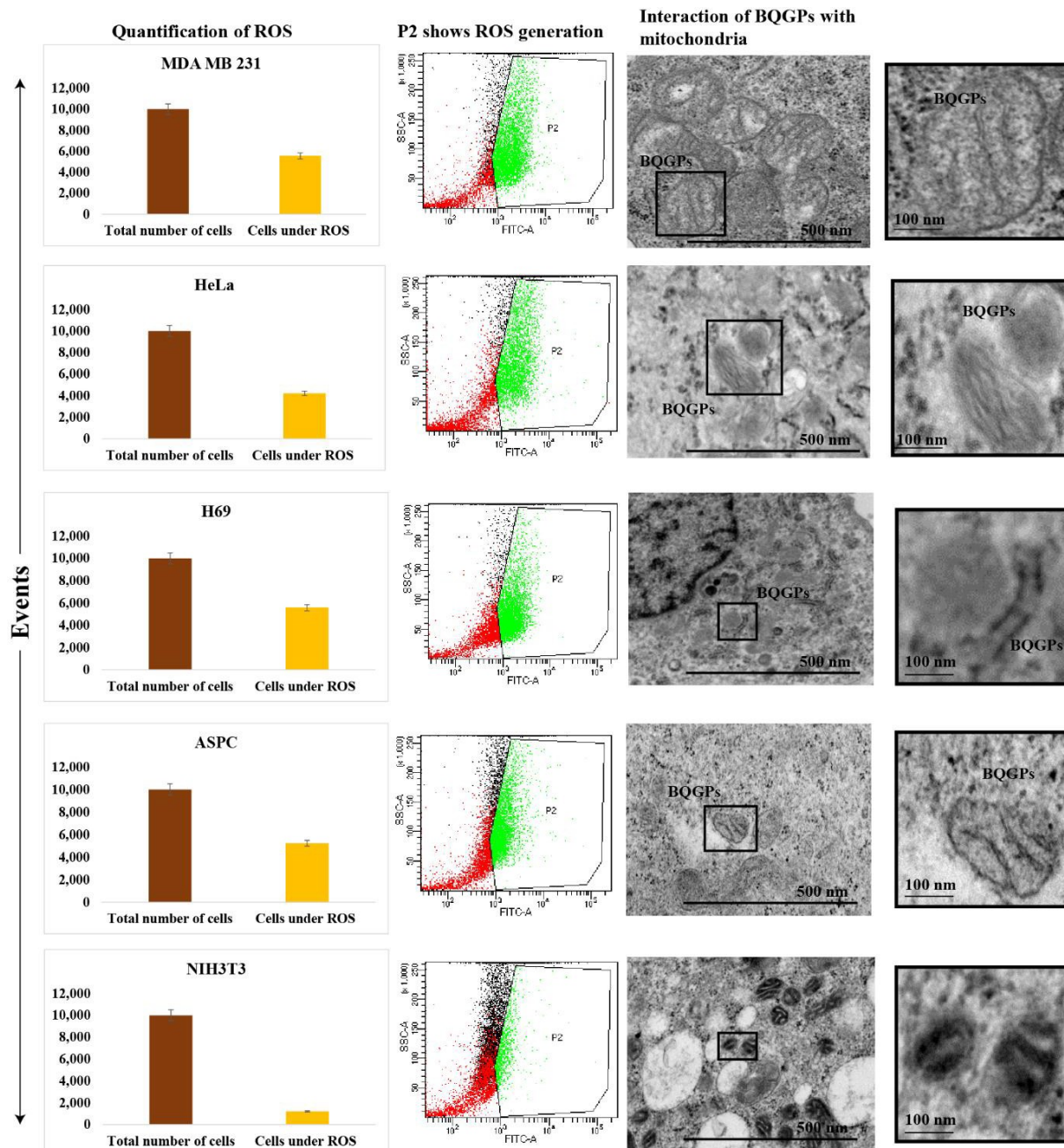
Figure 5.5 Significant increase in ROS production for quantum gold probe treated all four cancerous cells (MDA MB 231, ASPC-1, HeLa, and H69) in comparison to non-cancerous (NIH 3T3) cells. Data presented as mean ± mean, n=3, P-values are calculated using one-way ANOVA, *P<0.05

5.4.5 Mitochondrial membrane potential (MMP) disruption in cancerous cells

To continue the study of effects caused by increased ROS generation inside the mitochondria, here, the MMP disruption of the cells was studied. The mitochondrial disruption involves the alterations in the membrane potential and changes to the oxidation potential of the mitochondria, which results in hyperpolarization [232]. Mitochondria is the powerhouse of the cell and the primary source of reactive oxidative species like superoxide ions and anions [231], [236]. An increase in ROS leads the oxidative damage to cancerous cells and thus reduces the cell viability [237]

The Bio TEM images in Figure 5.6 shows, the interaction between mitochondria of the cells and drug-free BQGPs results in the disruption of the outer mitochondrial membrane, releasing the intermembrane cytochrome c to the cytosol, triggering the cascades signaling and resulting to cancer cell apoptosis [238], [239]. In this study, to assess the early apoptosis of cancerous cells (MDA MB-231, HeLa, ASPC-1, and H69) and non-cancerous cells (NIH3T3) induced by drug-free quantum gold, changes in the MMP were studied by JC-1 dye through a flow cytometer. The green and red intensity ratios were used to explain the changes in MMP. The increase in the ratio of green to red intensity indicates early apoptotic cells. After 24 hours of exposure of cancerous and non-cancerous cells to drug-free quantum gold, JC-1 results showed that drug-free quantum gold induces the mitochondrial damage in all the cancerous cells but not in non-cancerous fibroblast cells. Cancerous cells showed the increased ratio of green to red fluorescence intensity (the disruption of MMP) (Supporting Table 4), which exhibited the increased mitochondrial membrane disruption that might disrupt cellular metabolism, causing apoptosis. Whereas, non-cancerous fibroblast cells resulted in the decreased ratio of green to red fluorescence intensity, which showed that non-cancerous fibroblast cells maintained the intact mitochondrial membrane

121

(Figure 5.6). Thus, the drug-free quantum gold in all cancerous cells has significantly altered the cellular metabolism via the MMP disruption. The drug-free pristine BQGPs induced the disruption of the mitochondrial membrane in cancerous cells. This may due to the existence of quantum gold probes in the mitochondria resulting in the disruption of the mitochondrial membrane, which leads to an increase in cytoplasmic oxidative stress. [240].The flow cytometry data in Figure 5.8 already showed the increased level of ROS in cancerous cells as compared to non-cancerous cells.
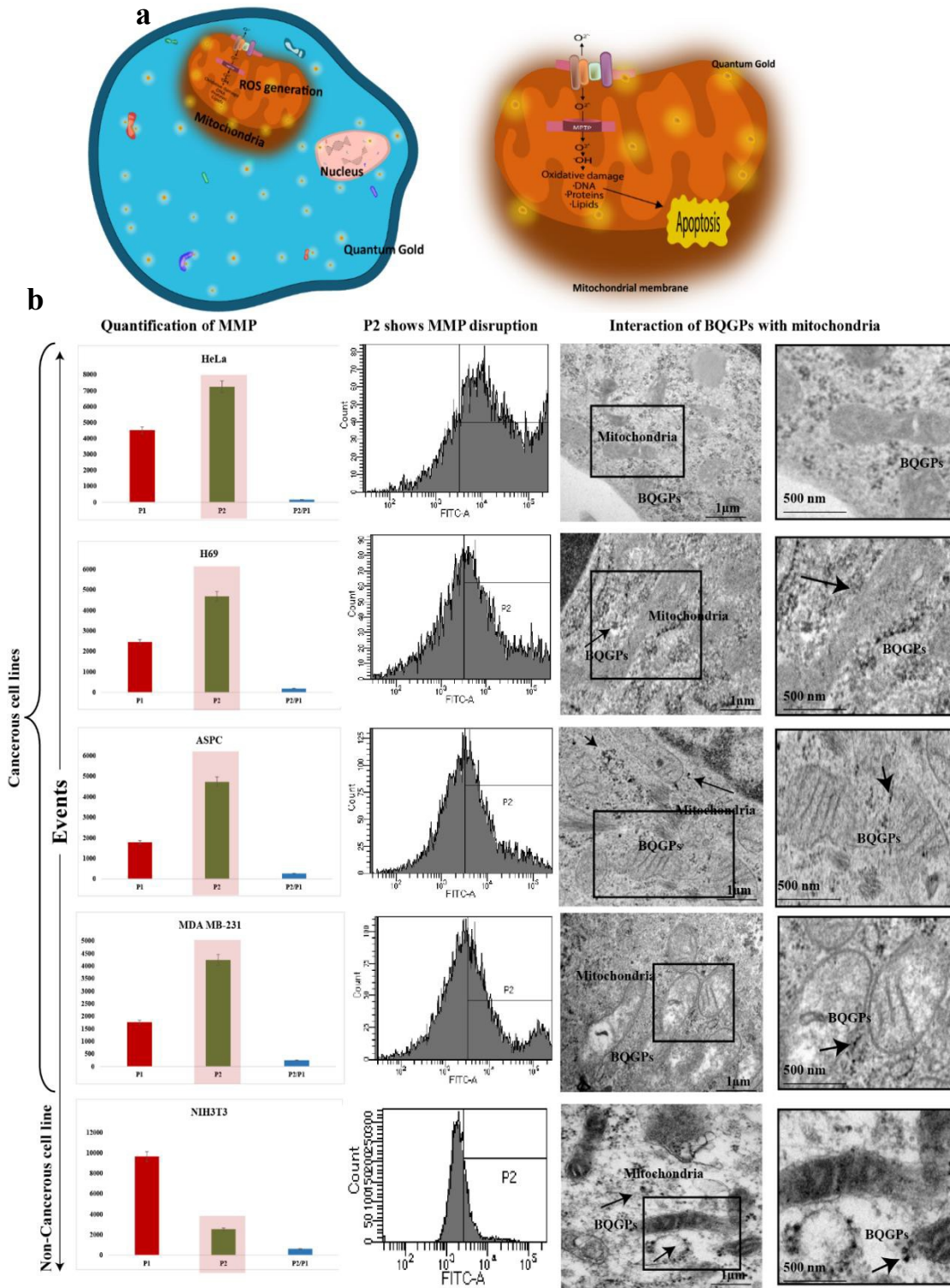
Figure 5.6 a) Schematic illustration of ROS generation inside the mitochondria, which leads to the disruption of mitochondrial membrane b) Increased MMP disruption in drug-free BQGPs treated cancerous cells. Data presented as mean ± mean, n=3, P-values are calculated using one-way ANOVA, *P<0.05

5.4.6 Simultaneous early and late apoptosis in cancerous cells

Apoptosis is linked to the disproportional increase of ROS in the mitochondria and mediates the oxidative damage to DNA. The mitochondrial ROS causes the release of cytochrome C, an irreversible process that leads to the activation of multiple caspases and cell death [241]. Apoptosis can be confirmed by the shrinkage and reduced size of cells and DNA fragmentation.[242]. Most of the researchers use functionalized chemotherapeutic drugs for the treatment of different cancer types. The presently used chemotherapeutic drugs have short and long-term side effects[243]. The use of chemotherapeutic drugs causes complications such as cardiovascular toxicity, mucositis, and neutropenia[244]. Adding to that, few cancer cells become resistant against the drugs, which can be occurred due to many different factors such as alteration in miRNA, cancer stem cells, apoptosis suppression[245], [246]. All these causes generate the need for drug-free treatment for different cancer types. The drug-free quantum gold was bonded with the major and minor grooves of DNA by the electrostatic forces which allowed changes in the DNA. As the experiments performed above explain, the cell death that had occurred in four different cancerous cells was due to the mitochondrial apoptosis pathways [49].

In the present study, to determine the early and late apoptosis of all cancerous cells and non-cancerous cells simultaneously, apoptotic assay by flow cytometry was performed. The cancerous cells were treated with the drug-free quantum gold for 24 hours. The aim is to use the non-cancerous fibroblast cells (non-cancerous cells) as a control to analyze its behavior against the treatment by drug-free quantum gold. The treatment of drug-free quantum gold promotes early and late apoptosis. Figure 5.7 shows that there is indeed a significant increase in the apoptosis of all the cancerous cells after 24 hours of treatment, whereas drug-free quantum gold did not induce statistically significant apoptosis in non-cancerous cells. Treatment by drug-free

quantum gold significantly upregulated the number of all four different types of cancer cells for early and late apoptosis, while promoting the reduction of total apoptosis in the non-cancerous fibroblast cells (Figure 5.7). Also, in order to validate the effect of BQGPs on non-cancerous cells, here healthy osteoblast cells (MC3T3) were studied. Results and discussion presented in supporting information (Note 4). Previous studies have shown that the mitochondria mainly mediate apoptosis induced by a gold nanoparticle. The upstream production of ROS elicited the mitochondria-related apoptosis [247]. The damaged mitochondria initiated the different cell signaling pathways and downregulation of damage repair proteins.
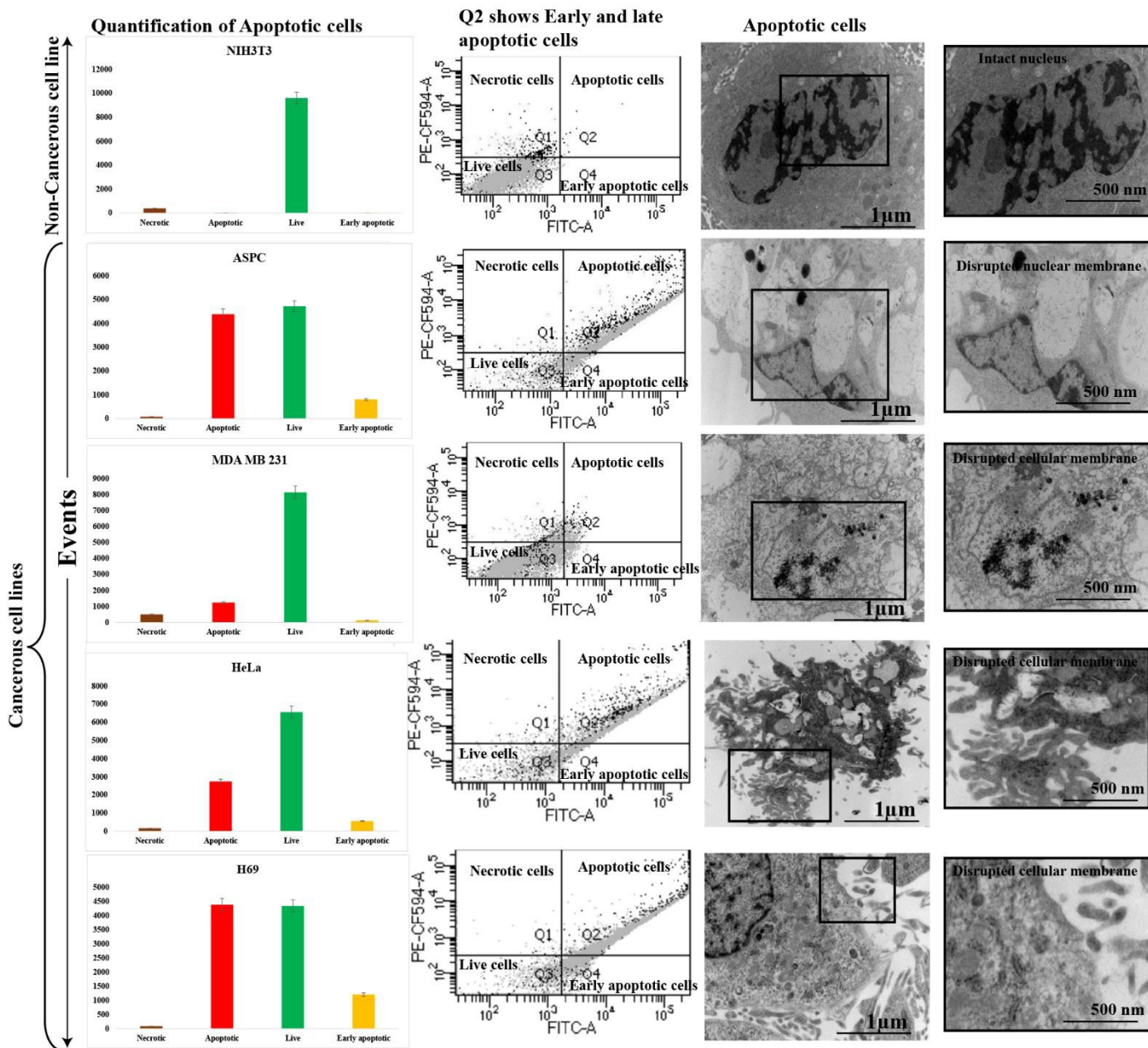
Figure 5.7 a) Schematics representation of cells undergoing apoptosis b) Apoptosis analysis of drug-free BQGPs treated cancerous cells by using flow cytometry. Data presented as mean ± mean, n=3, P-values are calculated using one-way ANOVA, *P<0.05

5.5 Conclusion

In this study, the label-free cancer theranostics was studied by using small-sized self-functionalized pristine BQGPs. Here, by using multiphoton ionization (physical synthesis), non-toxic BQGPs were synthesized without chemical contamination. Synthesized BQGPs were less than 5nm in diameter, demonstrated the fluorescence excitation at broad range wavelength. Small-size BQGPs showed a unique self-internalization phenomenon of energy independent passive uptake and dispersion in all parts of the cell (cytoplasm and nucleus). From cellular images, it was observed that cancerous cells internalized minimum 12 times more than non- cancerous cells, which lead to intensity-based fluorescence differentiation of cancerous and non- cancerous cell lines. Also, the broad range of fluorescence excitation and different series of the quantum size of BQGPs helped to distinguish the different types of cancer. Subsequently, the cancerous cells internalize the high number of probes than non-cancerous cells did, the label-free BQGPs induced mitochondrial apoptosis by generation the ROS in metastatic and multidrug- resistant cancer cell lines H69 (lung cancer), MDA MB 231 (breast cancer), HeLa (cervical cancer), and AspC-1 (pancreatic cancer), indicating cancer-selective treatment.

It was observed that the synthesized BQGPs consisted of different gold oxides and the purest form of gold in addition to being non-specific. Detection based theranostics can be attained without the need for multiple nanomaterials. This research provided the concept of fluorophore- free and drug-free cancer detection and cancer treatment simultaneously by using a single type of nanomaterial. This concept could be used for *in-vivo* detection based theranostics and clinical research in the future.

Chapter 6

Conclusions

Physically synthesized gold quantum particles were studied for cancer theranostics application (Fluorescence and SERS based cancer sensing and therapeutic effect). These gold particles are of a quantum scale and exhibit no-cytotoxic behavior in the intracellular environment.

Physically synthesized gold quantum particles internalize inside the cells and the nucleus by two different mechanisms, namely energy-independent passive uptake mechanism and endocytosis mechanism. The quantum particles self-internalize inside the cells and the nucleus. The gold quantum particles show different uptake rates and interactions with different cell types, which helps to differentiate different cell types. Cancerous cells show a minimum of three time's higher uptake of quantum gold particles as compared to healthy cells. The significant contrast in the number of internalized particles provides the opportunity for dosage-based differentiation of cancer/noncancerous cells and selective targeting of cancer cells.

The presence of native gold quantum particles inside the cellular environment does not perturb the ionic balance (sodium concentration), which is known to affect the stability of the genomic DNA structure directly. Besides, visualization analysis of genomic DNA by gel electrophoresis and fluorescence analysis show that the secondary structure of DNA remains intact. This shows that the nuclear localization of gold quantum particles does not cause changes in the intracellular environment. This is significant because all of the current DNA detection methods induce conformal changes in DNA structure; therefore, the results may not reflect the real chemical structure of DNA. The native gold quantum particles provide the opportunity to sense the DNA with high accuracy.

Two methods are investigated for cancer detection, fluorescence illumination, and SERS. The quantum particles showed selective cell uptake, where it was observed that cancerous cells internalized a minimum 12 times more than non-cancerous cells, which lead to intensity-based fluorescence differentiation of cancerous and non-cancerous cell lines. Besides, the broad range of fluorescence excitation and different series of the quantum size of BQGPs also helped to distinguish the different types of cancer. Also, with the quantum-sized plasmonic probes, label-free, and tag-free SERS detection of cancer were achieved. The quantum-sized plasmonic probes showed unique self-internalization and uniform dispersion inside the cells into the nucleus. Due to the probe size close to the size of cellular metabolites (~2-3nm) which successfully lead to the sensing of multiple mutated cancer receptors and oncoprotein (such as EGFR, HPV E6, and HPV E7) simultaneously, which could also be used to distinguish different cancer types (cervical and breast cancer). From the Raman readout, it was observed that there was a 1000-fold increase in the intensity of cellular metabolites compared to control. The complete biochemistry information of a cell from the surface to the nucleus is revealed by a single detection, which could be used for rapid and accurate identification of cell types. Our research may lead to a new type of platform for point-of-care sensing for reliable early cancer diagnosis.

Adding to this, the un-tamped quantum particles were used for the sensing of DNA molecules in the intracellular environment. The quantum particles internalize inside the cell by the endocytosis mechanism and inside the nucleus by diffusion mechanism. The presence of quantum particles inside the nucleus enhances the SERS signals by at least 700 folds and maximum by 1300 folds as compared to control. The probes were able to reveal the Raman fingerprint of DNA molecule in the complex intracellular/nucleus environment. By using PCA and Hierarchical Clustering analysis, different cancerous (pancreatic and lung cancer) and non-

cancerous (healthy fibroblast) cells were differentiated. Adding to this, different types of cancerous cells (pancreatic and lung cancer) were also distinguished by using PCA and hierarchical clustering analysis. The presented method is a step forward in sensing the DNA molecule in the intracellular environment. Later these gold quantum particles also showed high number of probes internalization in cancerous cells than non-cancerous cells did; the label-free BQGPs induced mitochondrial apoptosis by generation the ROS in metastatic and multidrug- resistant cancer cell lines indicating cancer-selective treatment. Here the current research opens a frontier for the future of gold-based nanomedicine and its application for sensing, diagnosis, and therapeutics in *in vitro* environment.

6.1 Major Contribution

Present salient highlights of the new findings from this study are as follows:

- Gold quantum particles were synthesized, which do not alter the genomic DNA secondary structure, which provides the opportunity to sense the DNA with high accuracy.

- Physically synthesized gold quantum particles self-internalize inside the nucleus by the passive energy-independent mechanism. These quantum particles are the only ones to internalize inside the nucleus without altering the cellular mechanism. The first, to report nuclear detection without labels.

- The contribution was made by studying the drug-free cancer therapy and simultaneous label-free fluorescence cancer diagnosis by using fundamental quantum gold particles.

- The simultaneous sensing of multiple cancer biomarkers and nucleic acids in the cellular environment. It has the potential to improve the accuracy of a cancer diagnosis significantly.

- Physical method (ultrafast laser ionization) for the synthesis of gold quantum particles were used, which eliminates the chemical residues and enables us to retain the small size of gold quantum particles. The synthesized quantum particles are biocompatible and non-cytotoxic.

6.2 Future research recommendations

With the development of these biocompatible and non-cytotoxic quantum gold particles that can exhibit multiplex fluorescence and SERS sensing and therapeutic effects in the *in vitro* environment, the possibility of developing *in vivo* application of physically synthesized un- tamped gold quantum particles can be envisioned. Moreover, some of the preliminary results suggest that the proposed cancer diagnostics and cancer therapeutic methods can be utilized for different cancer cell lines in the present study breast cancer, lung cancer, pancreatic cancer, cervical cancer, and healthy cells were examined and showed promising outcomes. Preliminarily results demonstrated the feasibility of present research methods for biomedical applications in *in vivo* environment.
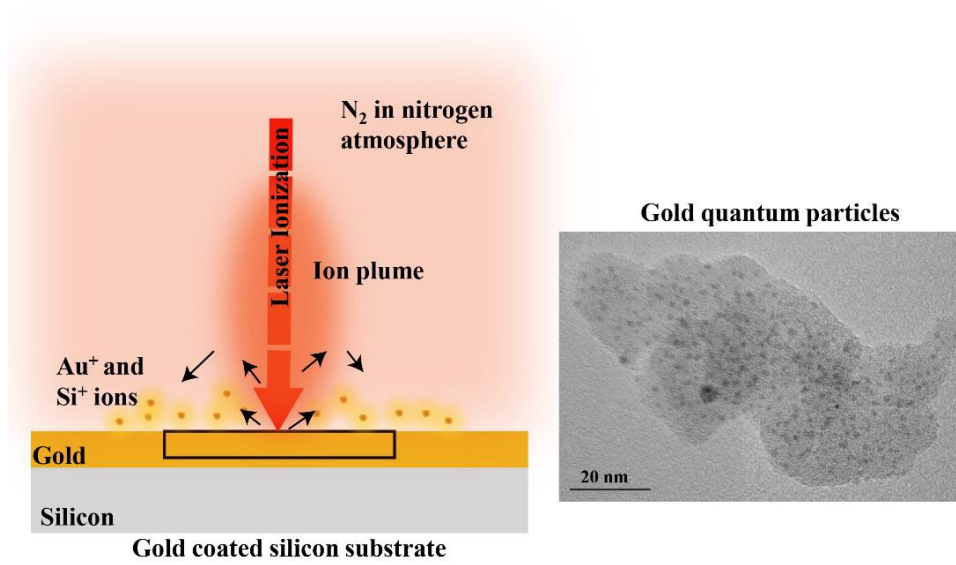
Supplementary Figure A-1 Multiphoton laser ionization synthesis of gold quantum probes
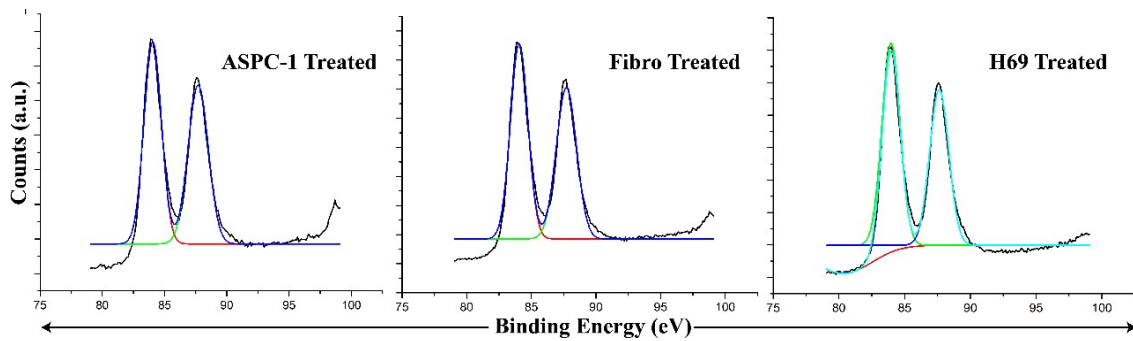
Supplementary Figure A-2 deconvoluted graphs for the gold spectra for treated cells
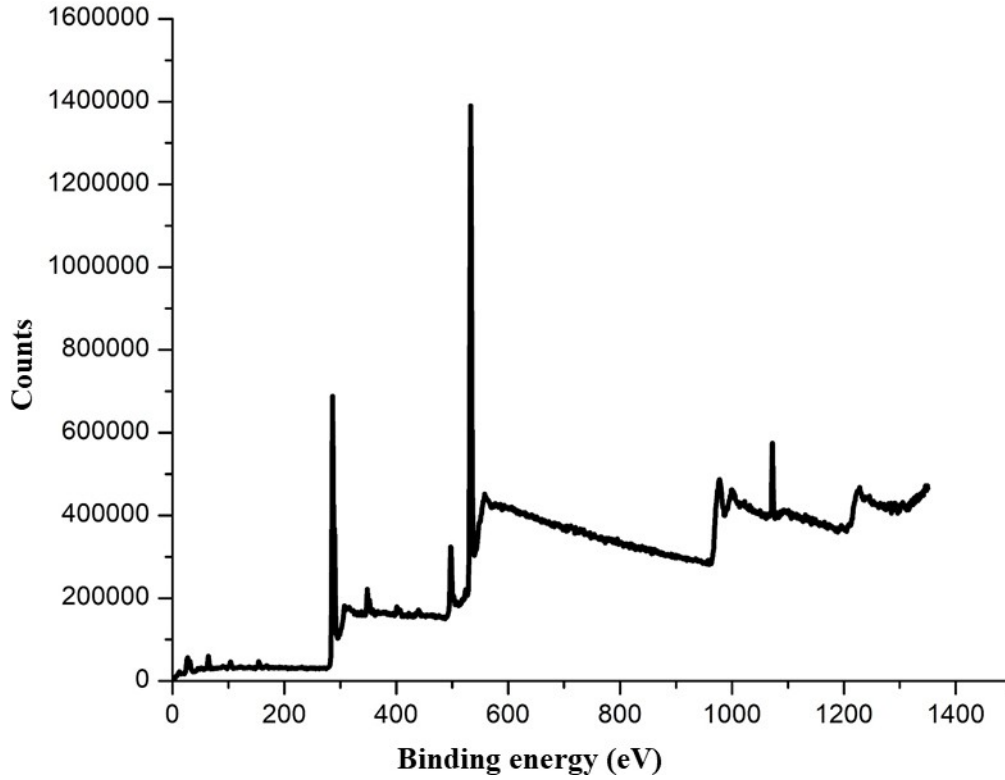
Supplementary Figure B-S1 Different phases of gold and silicon are represented by using survey graph of XPS analysis

Table B-1 Composition variation of Quantum biosensors with laser ionization.

Laser Ionization energy	Concentration of gold	Concentration of Silicon
26 MHz	12.29%	27.27%
12 MHz	4.5%	29.08%
8 MHz	0.7%	32.63%

Table B-2 Size variation of gold and silicon in Quantum biosensors

Laser Ionization energy	Median of gold particles (nm)	Median of silicon particles (nm)
26 MHz	5.74 nm	10.15 nm
12 MHz	3.55 nm	14.8 nm
8 MHz	2.4 nm	23.1 nm

Note B-1 Characterization of PQPs in different solutions (Medium and PBS)

The stability of PQPs was studied in the different solutions cell culturing medium and Phosphate saline buffer. HRTEM images were collected after 24 hours of treatment (Figure SX). PQPs remained almost of the same size 3.55nm, in a different medium environment. The particle distribution curve presented in Figure S represents the hydrodynamic size of PQPs measured. The HRTEM images show that the synthesized PQPs remain stable and retain their hydrodynamic size in cell culturing medium and PBS solution. The calculated particle size of PQPs also shows that there was no formation of the protein corona.
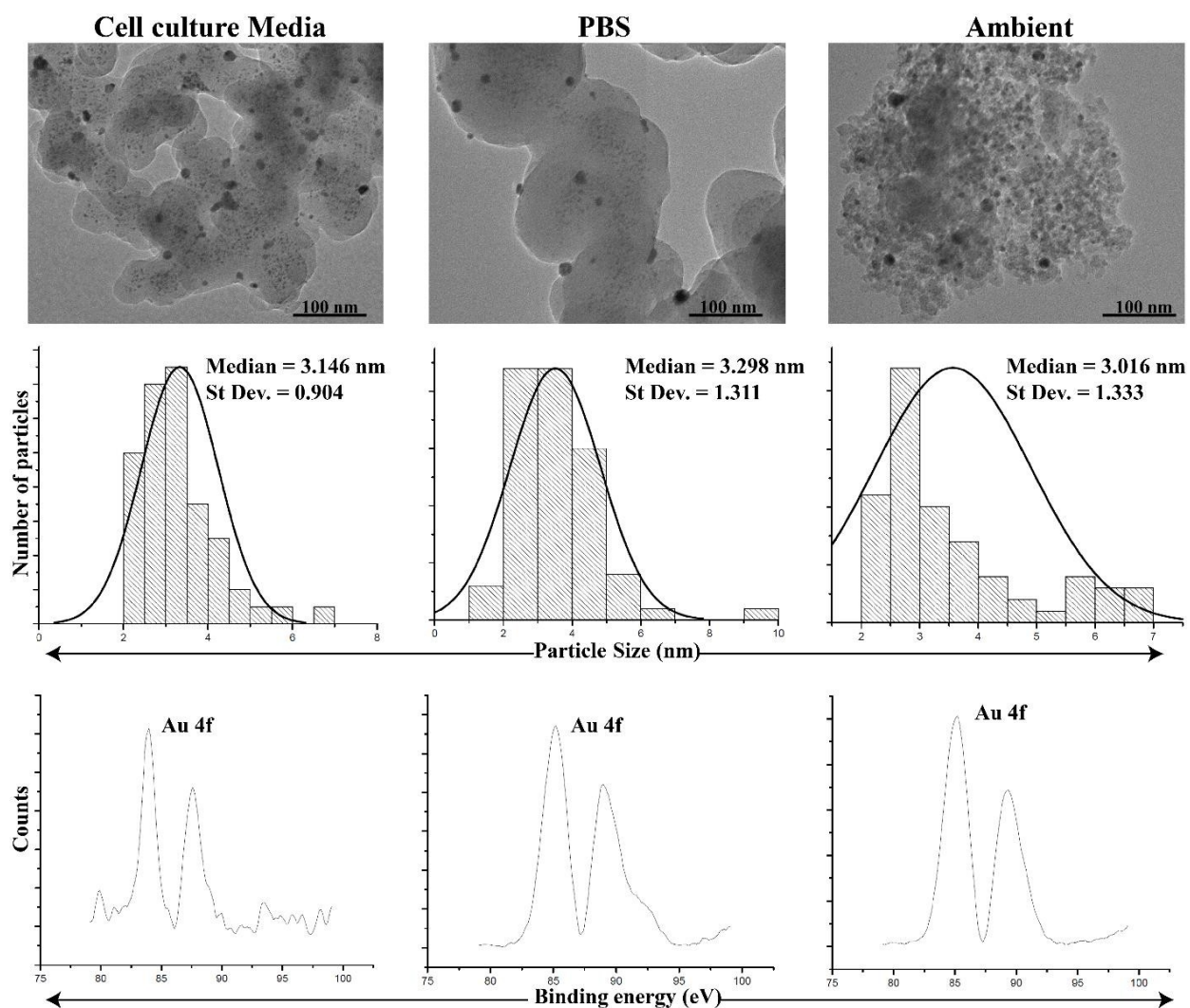
Supplementary Figure B-S2 Particle distribution curve of the gold quantum probes in different

environments and XPS analysis the gold quantum probes in different environments

Note B-2 EDX study of PQPs inside the cells

In order to confirm the presence of PQPs inside the cells, I have performed the EDX analysis of cancerous and non-cancerous cells. EDX elementary graphs show the presence of PQPs inside the cancerous cells. The elementary graphs support the BioTEM images; PQPs self mobilizes inside the cells. The EDX quantification shows the presence of 22.78 atomic% PQPs inside the breast cancer cells, and 16.73 atomic% of PQPs inside the cervical cancer cells and non- cancerous cells do not show the presence of PQPs showed in Figure SX. With the support of EDX analysis, we can validate the uptake of PQPs inside the cancerous cells.
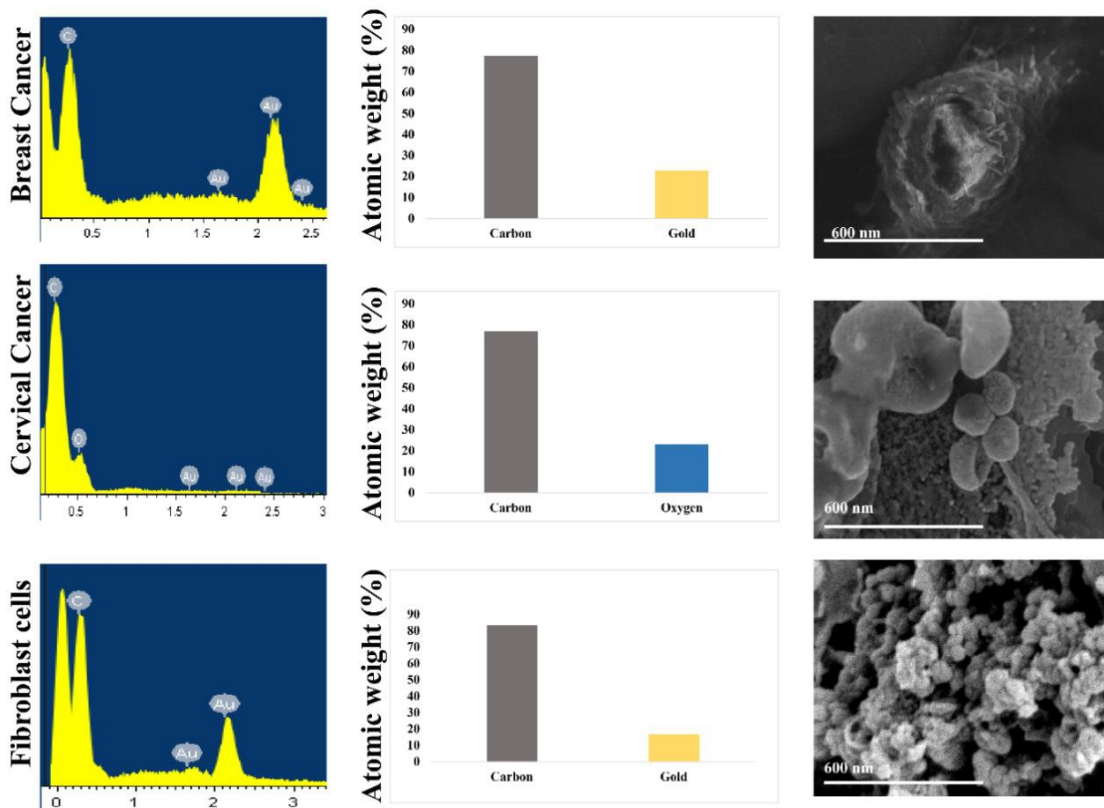
Supplementary Figure B-S3 EDX analysis of cancerous and non-cancerous cells for the quantification of elements

Note B-3- Particle size analysis of PQPs

In order to validate the particle size of PQPs, here we added the unprocessed XPS generated graphs, which shows the broadening of the peaks as the particle size decreases of PQPs (Figure SX). To support the XPS data, we have added HRTEM images to shows the quantum size of plasmonic probes.

In order to validate the HRTEM images and XPS spectrum, here we have calculated the particle sizes of PQPs by using XRD results. To calculate the PQPs particle size by XRD, we have used the Scherrer Equation

$$L = \frac{K\lambda}{\beta \cos\theta}$$

where L is crystallite size (nm),

K is crystallite shape factor constant (0.9),

λ is X-ray wavelength constant (1.54060),

β is full width at half maximum (FWHM) in radians(1.736 deg.)

θ is Braggs' angle (deg.) (38.189 deg.). By using the Scherrer Equation, the

calculate particle size was 5.8 nm.
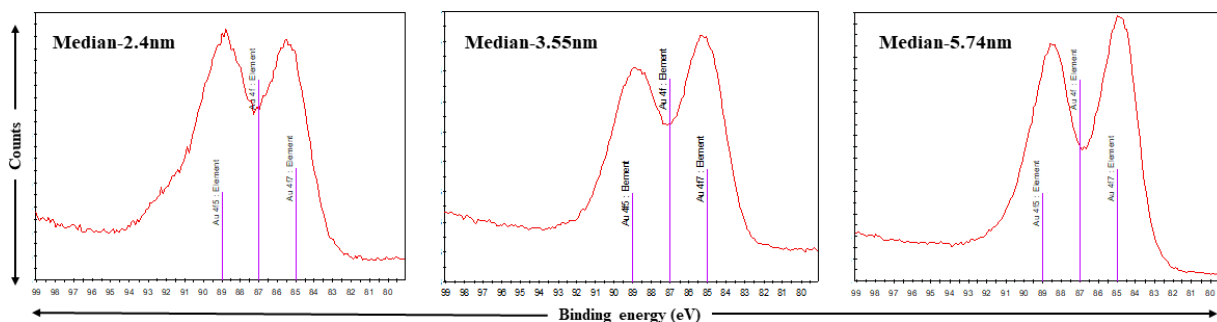
Supplementary Figure B-S4 Unprocessed data for PQPs particle size analysis by XPS

Note B-4- Cytotoxicity analysis of PQPs by using MTT assay

In order to validate the biocompatible nature of synthesized PQPs, here we have performed cytotoxicity analysis. The cancerous and non-cancerous cells were treated with the PQPs for 24 hours. The results show that PQPs does not inhibit cell proliferation, as only 1.6% of breast cancer cells, 1.2% of cervical cancer cells, and 1.6% of healthy fibroblast cells were dead. The PQPs does not have any side effects and are biocompatible.
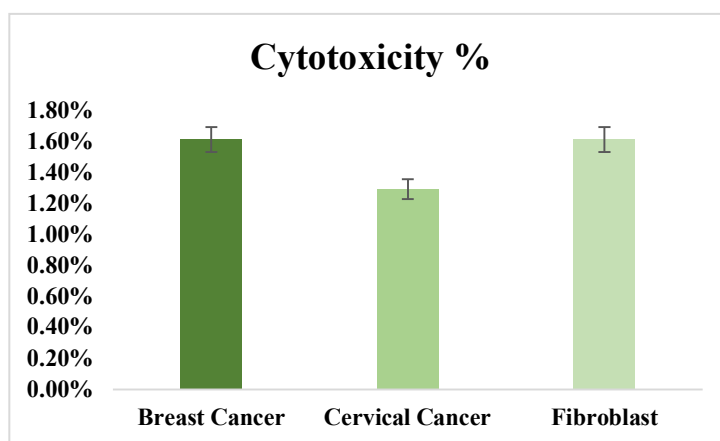
Supplementary Figure B-S5 Plasmonic quantum probes cytotoxicity studied with cancerous and non-cancerous cells
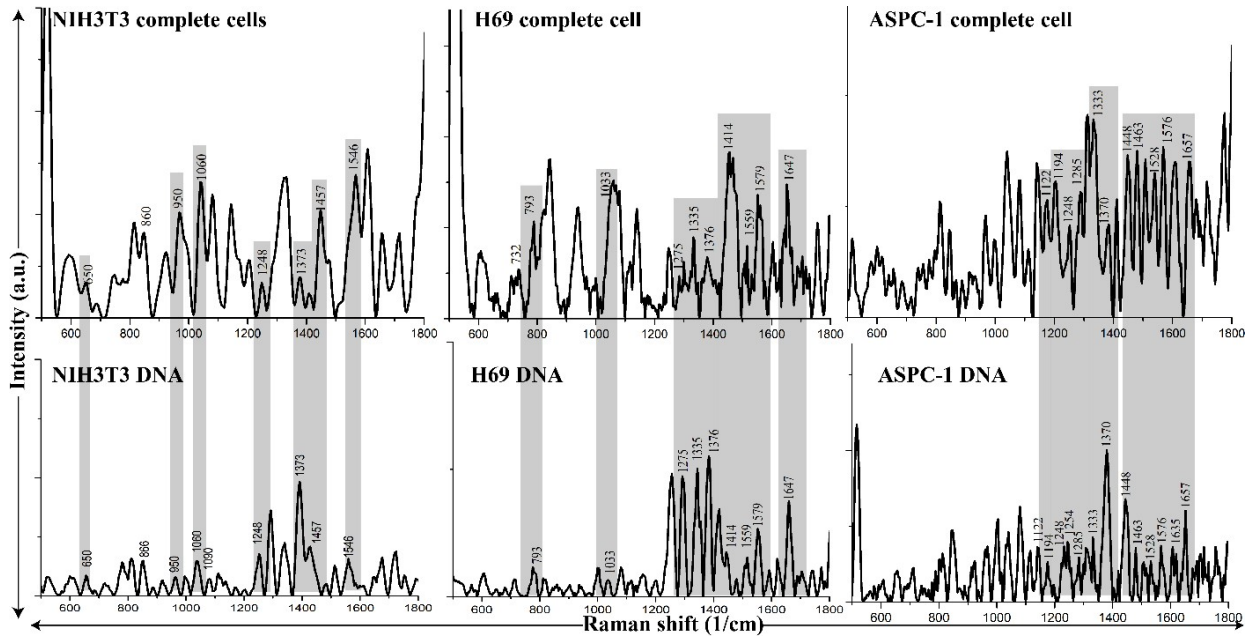
S.I. Figure C-1 Comparison of Isolated DNA with the DNA in the in the intracellular

environment

Table C-1 Peaks associated with the SERS signals presented in Figure 5.3, 5.4 and 5.5

Peak Position (1/cm)	Peaks assignments
650	dC, backbone
745	Symmetric breathing, tryptophan
811	Stretching mode (C-C), proline δ (CCH) ring
866	Guanine
922	C-C structure α helix
950	Guanine
1060	Guanine
1081	C-N structure
1206	C-CH5 structure. Phe, Tyr
1248	Thymine
1330	CH def
1373	dA,dC,dT
1409	Symmetric CH3
1457	A,G,T
1477	δ (CH2), δ (CH3), collagen
1546	Stretching mode (C=C), tryptophan
1607	Stretching mode (C=C), tryptophan
1656	Stretching mode (C=O) amide I, α-helix, collagen, elastin
1716	Stretching mode (C=O), phospholipids

Table C-2 Peaks associated with the SERS signals presented in Figure 5.3, 5.4 and 5.5

Peak Position (1/cm)	Peak assignments
752	Symmetric breathing, tryptophan
855	Stretching mode (C-C), proline δ (CCH) ring
1004	Symmetric stretch, (C-C), symmetric ring breathing, phenylalanine
1223	Asymmetric stretch (PO2) nucleic acids
1322	CH3CH2 twisting, wagging, collagen
1335	CH3 CH2 wagging, collagen
1445	δ (CH2), δ (CH3), collagen
1552	Stretching mode (C=C), tryptophan
1582	Δ (C-C), phenylalanine
1618	Stretching mode (C=C), tryptophan
1655	Stretching mode (C=O) amide I, α-helix, collagen, elastin
1745	Stretching mode (C=O), phospholipids

Table C-3 Peaks associated with the SERS signals presented in Figure 5.3, 5.4 and 5.5

Peak Position (1/cm)	Peak assignments
1248, 1285	Ring Stretching (Cytosine)
1333	CN Stretching (Adenine and Guanine)
1370	Ring Stretching, CN stretching (Thymine)
1448	CN s e CM e bending (Thymine)
1463	CN s e CH b (Guanine)
1576	NH2 sciss (Adenine)
1635	C=O stretching (Guanine)

Table C-4 Peaks associated with the SERS signals presented in Figure 5.3, 5.4 and 5.5

Peak position (1/cm)	Peak assignments
650	dC, backbone
866	Guanine
950	Guanine
1060	Guanine
1090	P02 backbone
1284	Thymine
1373	dA,dC,dT
1457	A,G,T

Table C-5 Peaks associated with the SERS signals presented in Figure 5.3, 5.4 and 5.5

Peak Positions (1/cm)	Peak assignments
732	Ring breathing modes of poly-A
793	Ring breathing modes of poly C poly T
1335	Poly A vibrations
1559	Adenine bands
1579	Poly G
1647	Carbonyl stretching mode of poly C

Appendix-D

Note D-1 Synthesis of pristine BQGPs on silicon nanostructure by using ultra-short femtosecond laser

The quantum gold was fabricated by using the femtosecond pulsed laser with a wavelength of 1030 nm and a 214 fs pulse width.

The processes of nucleation and condensation explain the synthesis of pristine BQGPs on silicon nanostructure. When the femtosecond laser interacts with the surface of the gold-coated silicon substrate, the energy is immediately absorbed by the conduction band electrons. This increases the temperature near the surface. The ultrashort laser pulse increases the temperature of the electrons (present on the substrate) and leaves the surface comparatively cooler at the top. There is a gradual energy transfer from the electron to the surface due to electron-phonon coupling. At high ionization energy, the pulse alters the gold film and consequently increases the absorption of the gold surface. The laser radiations interact with the gold-coated silicon wafer (Supporting Figure 1) and allow the direct ionization of gold and silicon, forming an ion plume containing Si^+, Au^+, and O^{2-} ions. The silicon and gold ions generated will then interact with the ambient environment. [248], [249]. The melting point of silicon (1414°C) [250] is higher than that of gold (1063°C), due to which silicon nucleation stops before that of gold, resulting in silicon condensation before gold. This process explains the formation of gold QDs decorated silicon structure.

In this study, we can program the chemistry of the synthesized quantum gold probe by modifying the laser ionization to tune the material for theranostics application. The material morphology and chemical composition are controlled by several factors, including the repetition rate, pulse

width, and scanning speed. This quantum gold probe can be modified to achieve higher therapeutic reactions to different cancers. Therefore, the laser ionization conditions were stabilized to the conditions which provide the maximum theranostics application for cancer cell differentiation and cancer therapy.
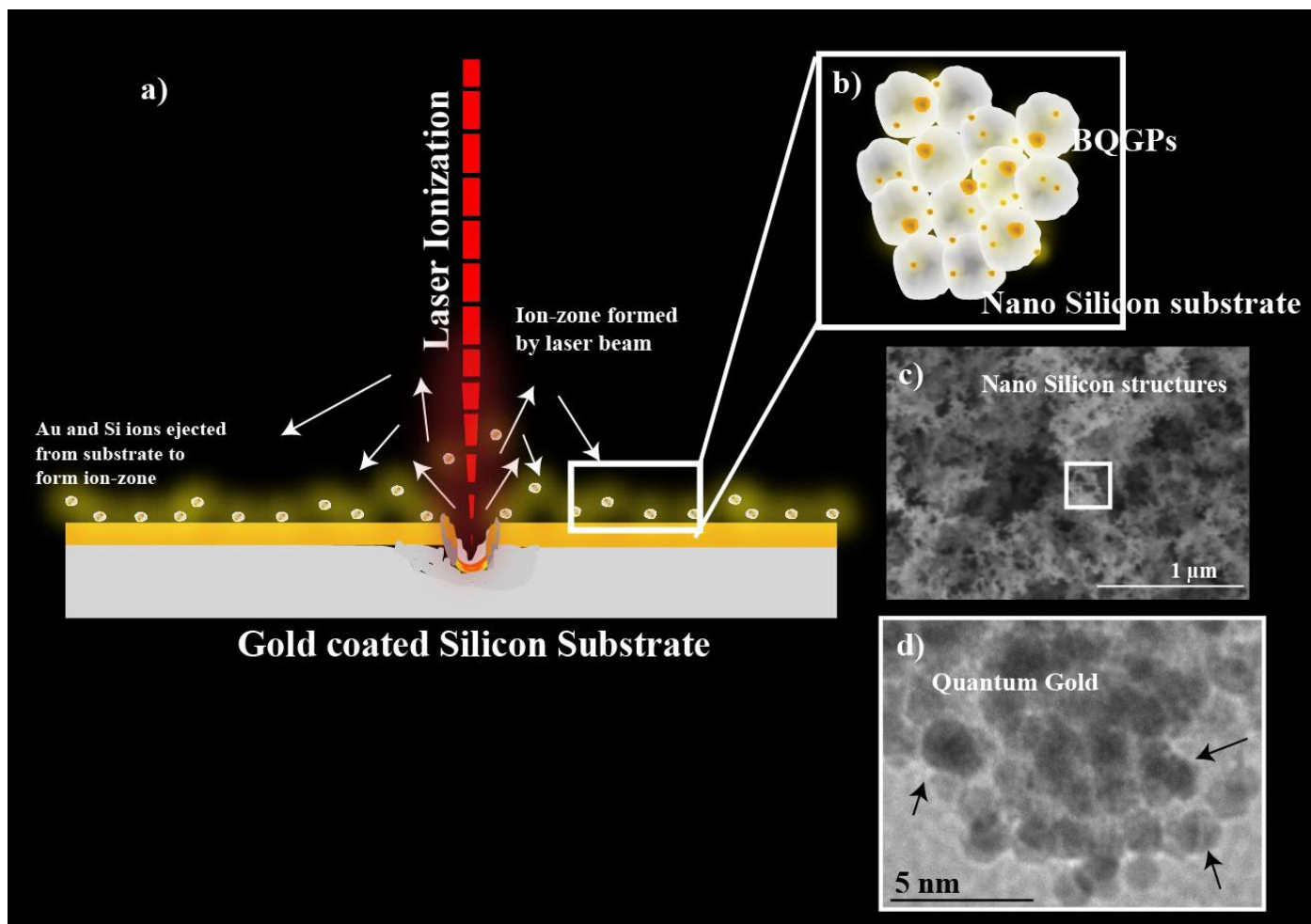
Supporting Figure D-S1 a) the laser synthesis process of gold QDs decorated on silicon nanostructures b) schematic illustration of BQGPs on nano silicon structures c) SEM image showing the silicon nanostructures d) HRTEM image shows the presence of BQGPs
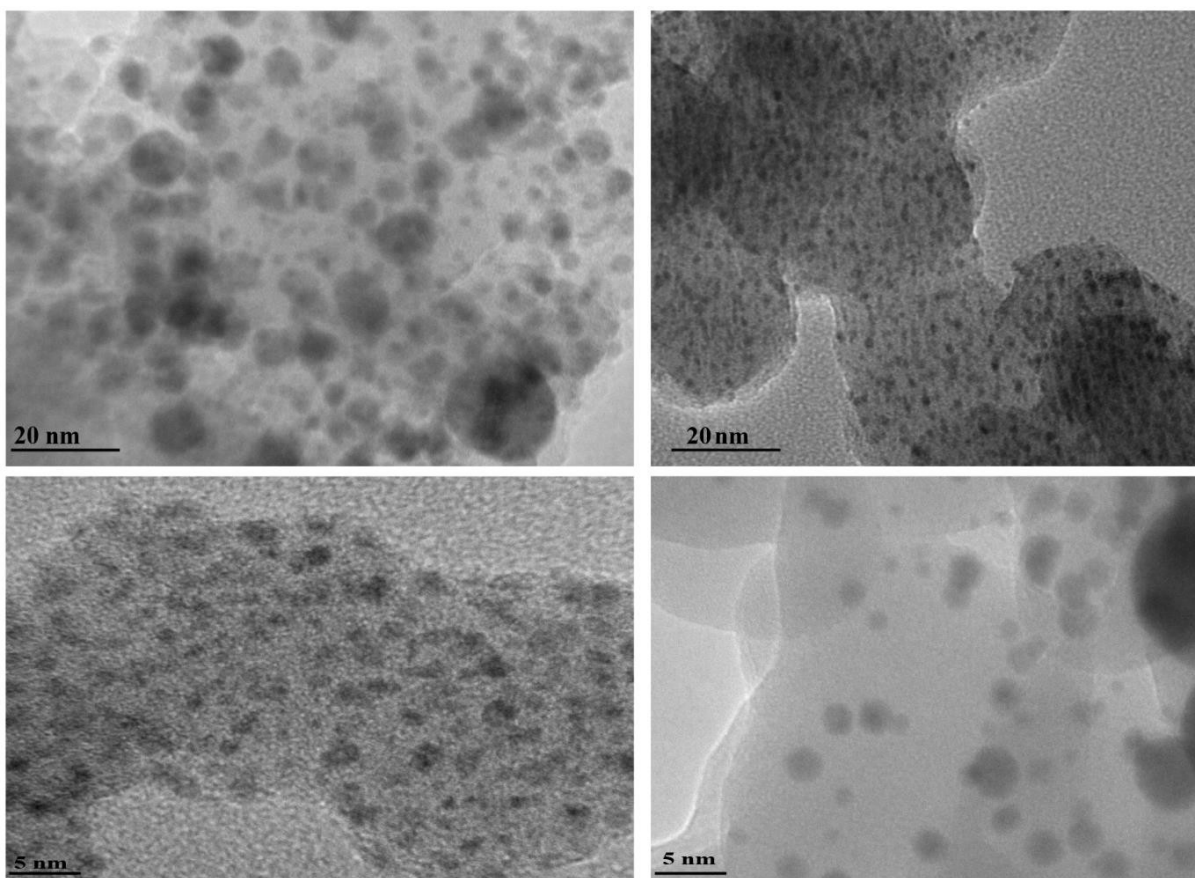
Supporting Figure D-S2 HRTEM images of Quantum Gold probes.

Note B2: Study the stability of synthesized gold quantum probes in different environments

The stability of quantum gold probes was studied in the three different solution Medium, Serum, and PBS solutions. HRTEM images were collected after 24 hours of treatment (Figure S2), Quantum gold probes after treatment remained the almost same size of 3.2 nm. All the gold probes size discussed for the stability in this section representing hydrodynamic diameters measured by the particle distribution curve (Figure S3). The HRTEM images and particle distribution curve shows that the synthesized particles are stable and retain their hydrodynamic diameter in the different environment (Serum, PBS, and Medium). To explain the chemical stability of the synthesized gold probe, we have performed XPS analysis of treated quantum probes in different solutions.
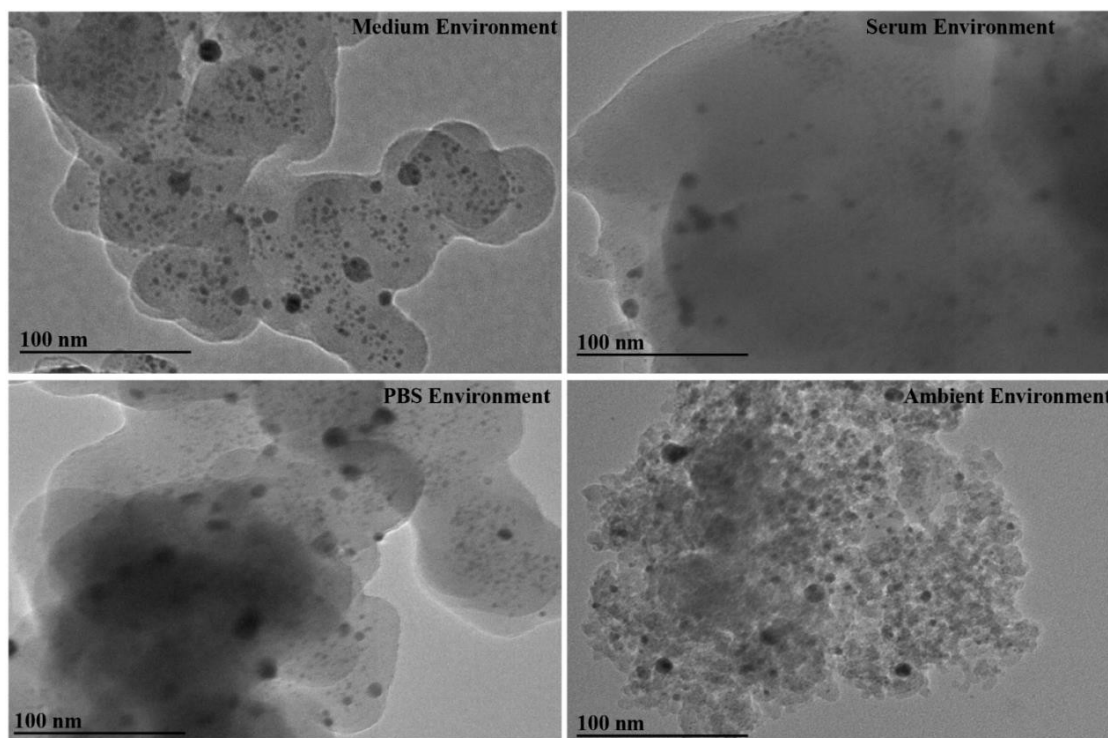
Supporting Figure D-S3 HRTEM images of the gold quantum probes in different environments.
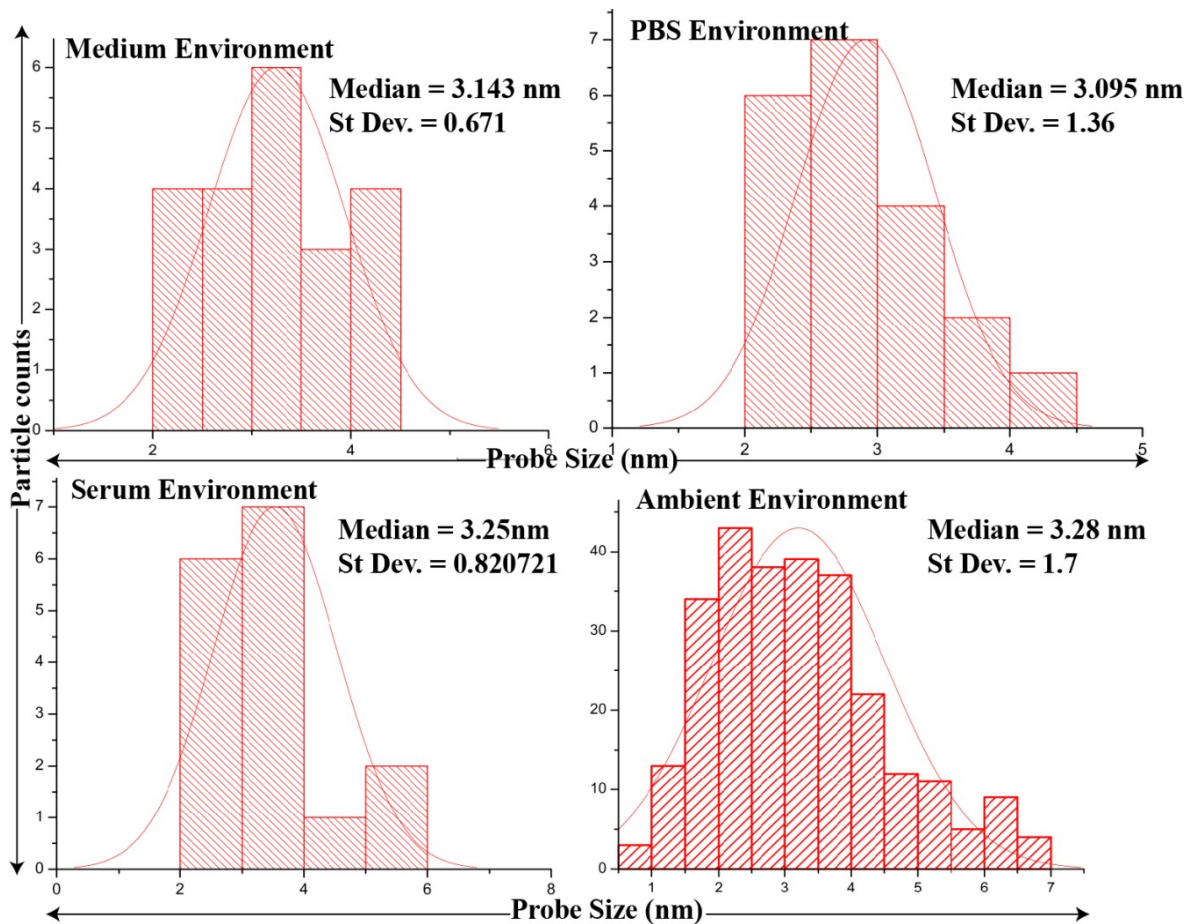
Supporting Figure D-S4 Particle distribution curve of the gold quantum probes in different environments.
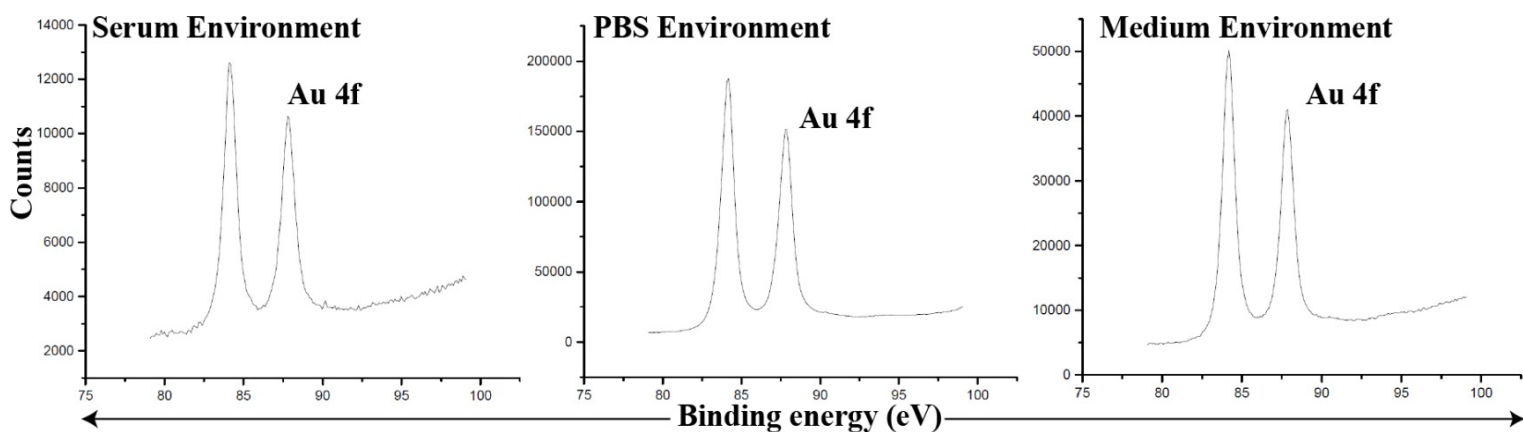
Supporting Figure D-S5 XPS analysis, the gold quantum probes in different environments.
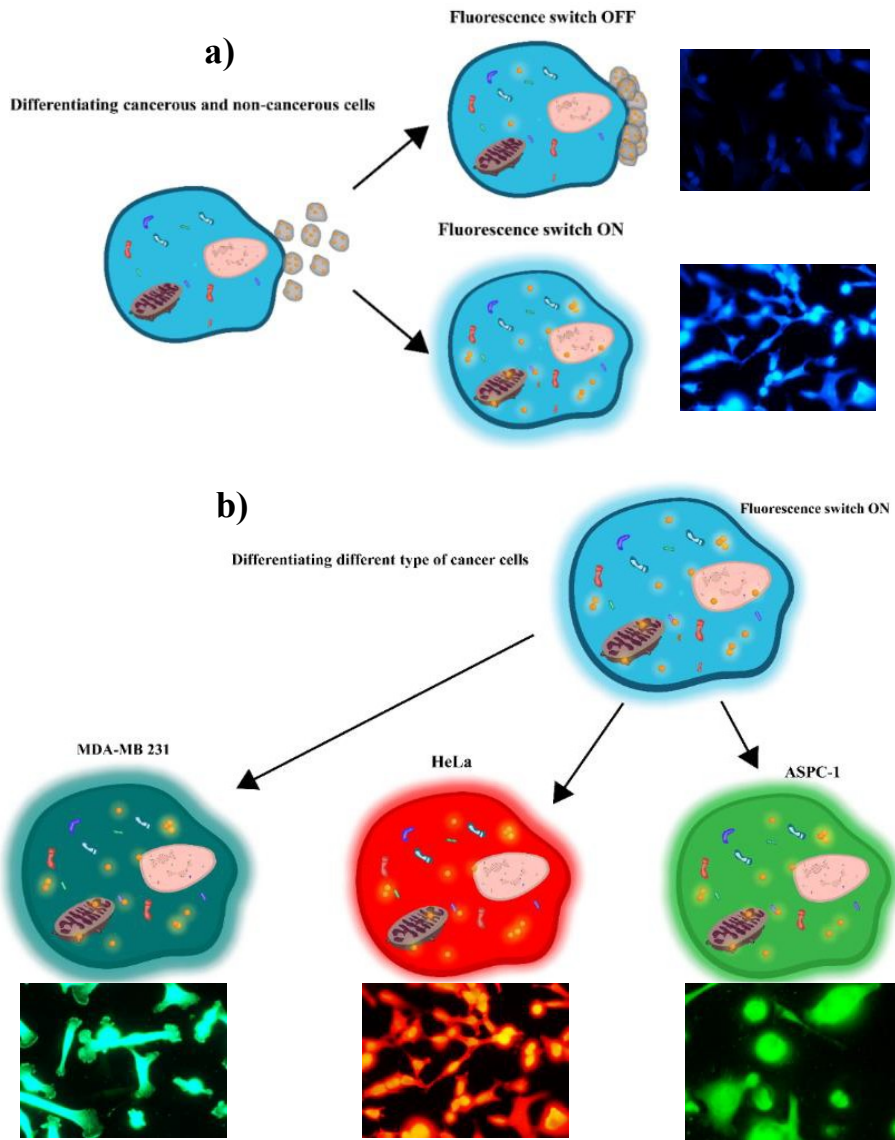
Supporting Figure D-S6 a) represents the schematics differentiating cancer (fluorescence switch ON) and healthy cells (fluorescence switch OFF) and Figure 5 b) shows the schematics of differentiating different types of cancerous cells based on intensity differences

Table D-1 Increased production of ROS in cancerous cells

Cell line	ROS production (%)
HeLa	44
MDA MB 231	55
ASPC-1	35
H69	41
NIH 3T3	5

Note D-3: Difference in uptake and interaction of quantum gold in cancerous and non-cancerous cells, and a nuclear and mitochondrial membrane

Differentiation of cancerous and non-cancerous cells was done based on the bright quantum gold's interaction with the cell membrane and nucleus by using a Bio-TEM after 24 hours of cell seeding. Selected images are shown in Supporting Figure S6.

Primarily, we notice that no BioTEM images show the presence of silicon/silica inside the cells. Even though there are silicon/silica probes were present in the vicinity of the cells, the initialized probes were BQGPs. Based on the previous investigation, silica/silicon nanoparticles of tens of nanometers degrade in a few hours of cell seeding[251]. After 24 hours of cell seeding, we could assume that silicon probes present in the vicinity of cells get non-functional and disintegrates. This explains why there is no silicon/silica probes are present inside the cells. Therefore, the presence of silicon probes acts as cargo for the delivery of gold probes. Moreover, they provide the structural support and adhesive platform for cells to proliferate.

Earlier researches have shown that the cell membrane plays a critical role in the uptake of foreign particles inside the cell. Due to the various compositions and interaction behaviors of the cell membrane, the uptake of foreign particles differs per cell type. Here, Supporting Figure S6 a) shows the schematics of the difference in the interaction between bright quantum gold and the cell membrane of cancerous and non-cancerous cells. Several factors are taken into account for the different uptake and interactions of BQGPS with the cancerous and non-cancerous cell membranes. It is mostly the composition of the lipids, phospholipids, and proteins present in the cancerous cell membrane that is different from the non-cancerous cell membrane. A previous study by Junling Chen [252] showed that cancer cell membranes express a higher concentration of proteins and phospholipids than healthy cell membranes. Not only do they express a higher concentration, but also their distribution of phospholipids is larger in cluster size. The difference in the electrostatic properties of the cell membrane of individual cell lines may also be responsible for different uptake. The internalization of BQGPS is a process which majorly affected by efficient contact of the cell membrane [253]. Supporting Figure S6 a) displays Bio- TEM images of the cell membrane interaction with quantum gold. Therefore, it was hypothesized that the different interaction mechanisms of cancer and non-cancerous cells' membrane with quantum gold led to a different uptake mechanism. Figure 4 and Table 1 show the difference in the uptake of gold quantum probe in the cancerous and non-cancerous cells.

Previous studies show that the nucleus of the cell is the most important, as it controls the cellular functions like proliferation, differentiation, and apoptosis of the cell [169]. To improve the therapy based theranostics here, we targeted the nucleus of the cancerous cells. Supporting Figure S6 b) shows the presence of quantum gold inside the nucleus of the cancerous and non- cancerous cells. However, due to the different uptake numbers of quantum gold, it was easy to

differentiate between the cancerous and non-cancerous nucleus, as shown in Table-2. Generally, the nuclear membrane does not allow molecules to enter the nucleus. The nucleus structure consists of a nuclear envelope, which includes a double layer of lipid, nuclear lumina, chromosomes, which consist of DNA, RNA, and nucleosomes, which include rRNA and rDNA. As a result, the nuclear envelope the entry of the nanoparticles inside the nucleus unless the nanoparticles are extremely small (<5nm) [42], [254]. Since the synthesized quantum gold is

3.28 nm in size, it can easily penetrate the nucleus membrane. Based on the previous studies [255], [256], it was theorized that the difference in uptake ratio of quantum gold in cancerous and non-cancerous cells was due to the composition of the nuclear membrane. Elucidation of BQGPs nucleus interaction provides the crucial insight into the biological activity of BQGPs.

Supporting Figure S6 explains the interaction of quantum gold with the cellular components in cancer and non-cancerous cells.

Table D-2 The number of a probe in cancerous and non-cancerous cells, collected from Bio TEM images of cells presented in Supporting Figure C-S6a.

Cell line	The average number of probe/cell
HeLa	1295
MDA MB 231	1184
ASPC-1	1074
H69	1306
Fibro	87

Table D-3 The number of probe uptake in the cancerous and non-cancers nucleus, collected

from Bio TEM images of cells presented in Supporting Figure S6 b

Cell line	The average number of probe/nucleus
HeLa	46
MDA MB 231	36
ASPC-1	37
H69	57
Fibro	7
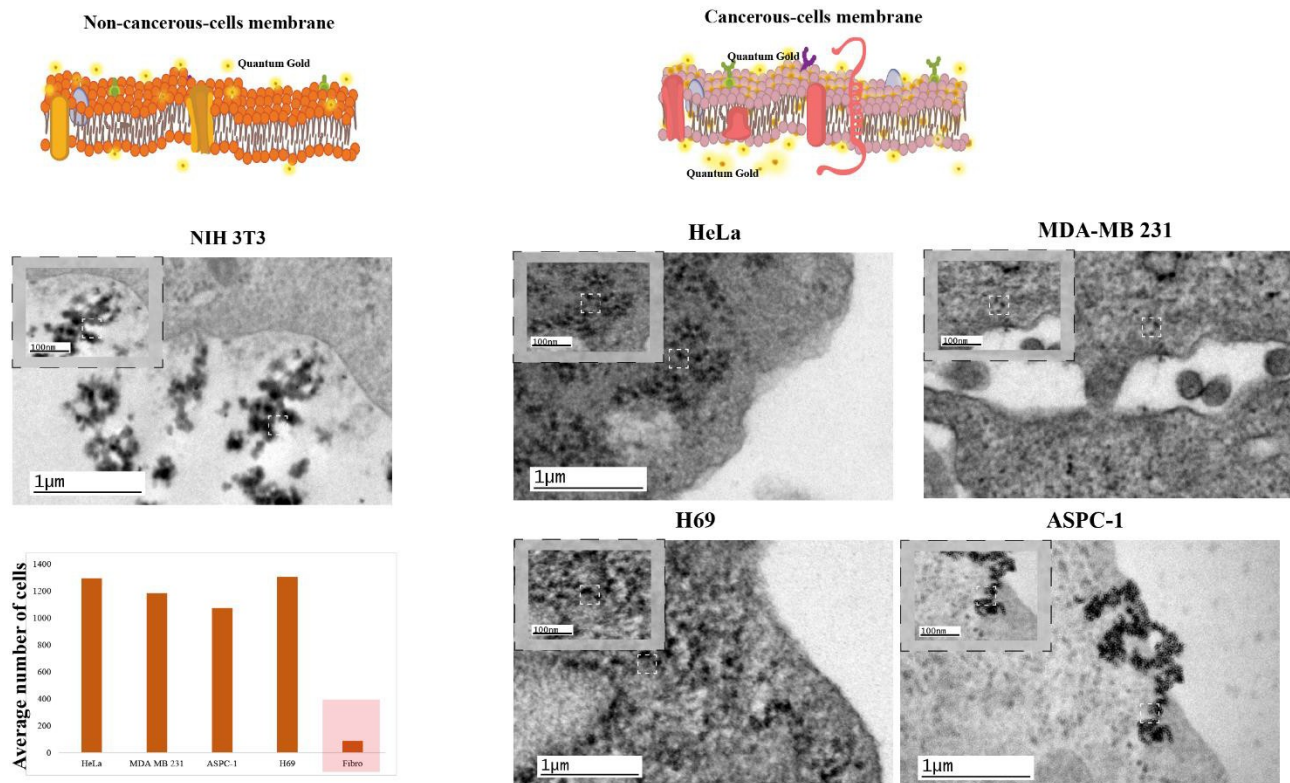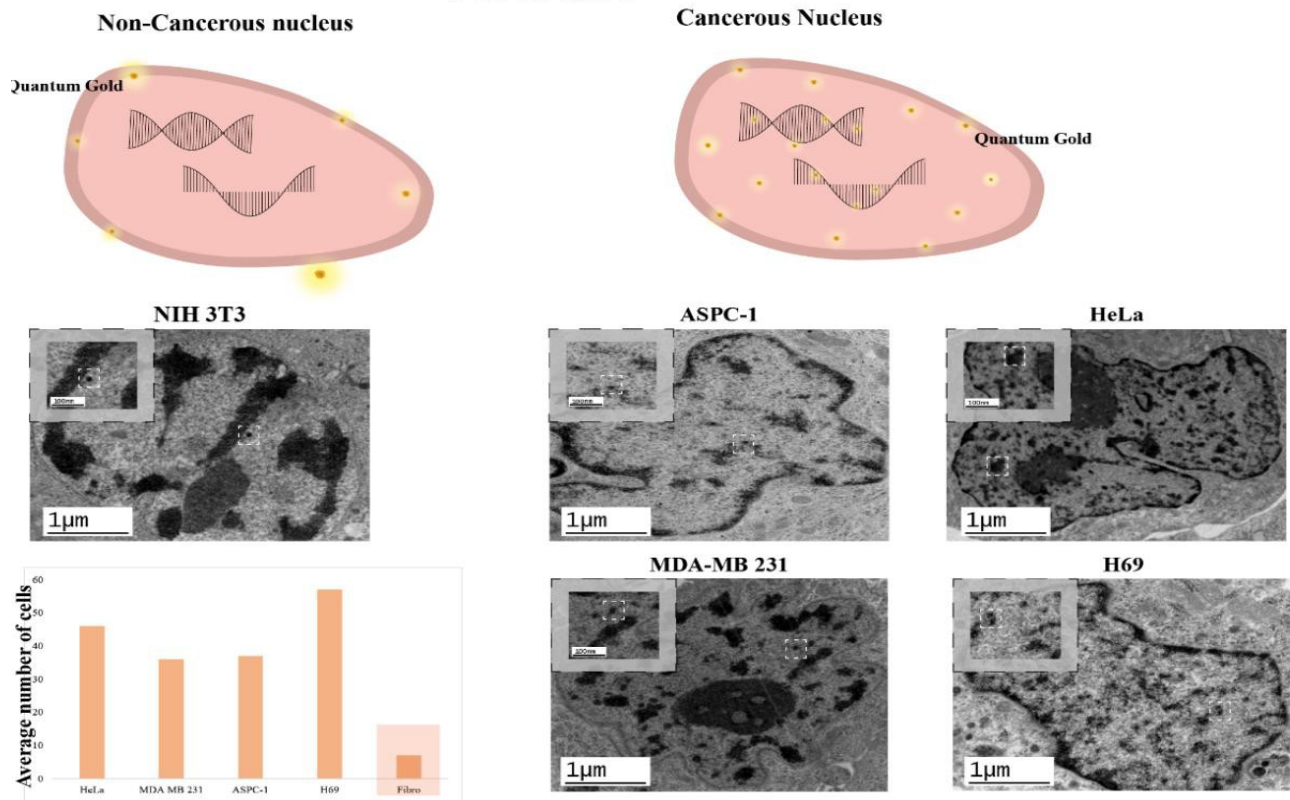
Supporting Figure D-S7 a) different probe uptake by cell membrane b) different probe uptake in nucleus
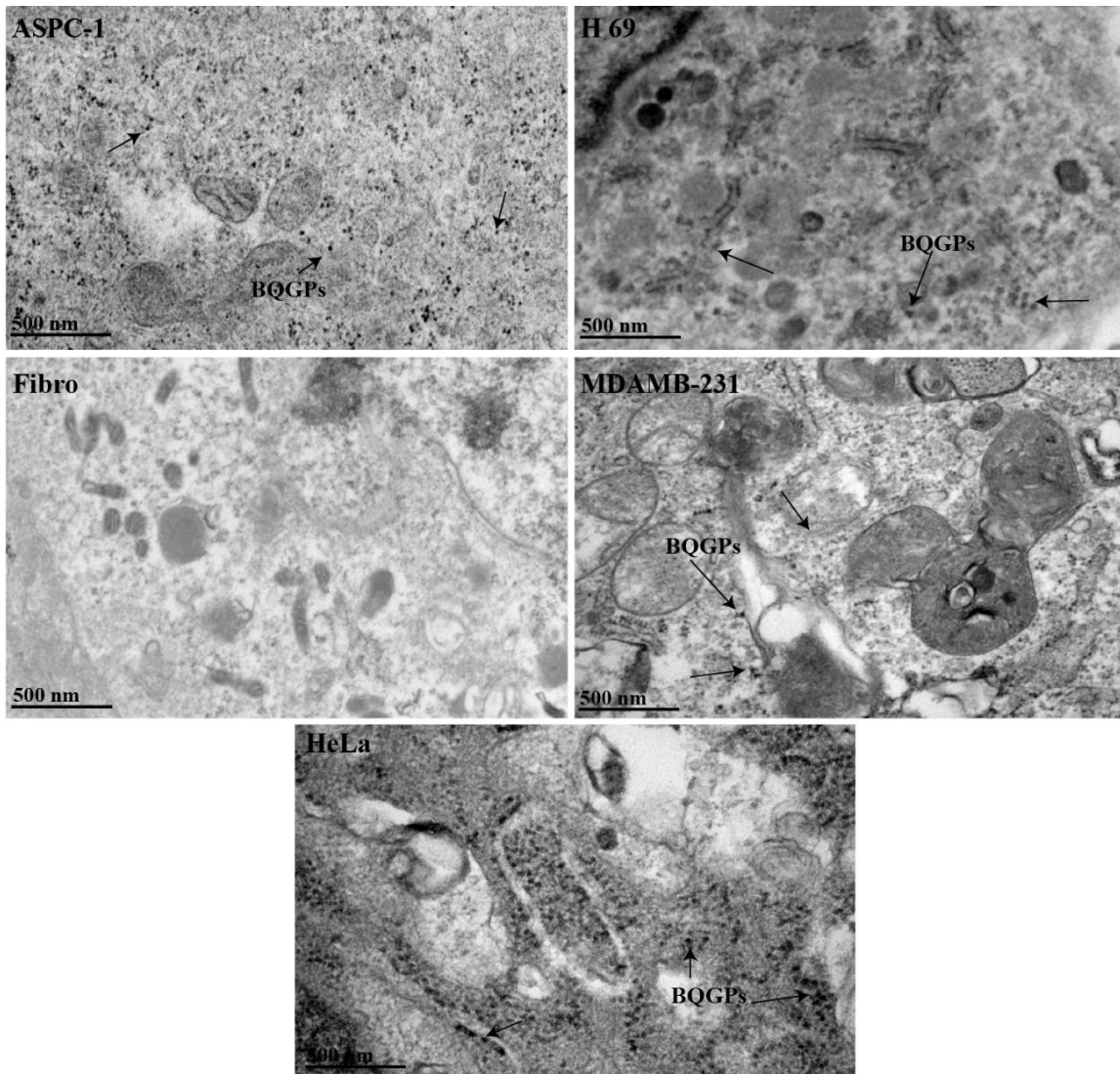
Supporting Figure D-S8 Presence of BQGPs inside the cancerous cells (ASPC-1, H69, MDA-MB-231, and HeLa).

Table D-4 Ratio of green/red intensity for MMP disruption

Cell line	The ratio of green/red intensity for MMP disruption
HeLa	5
MDA MB 231	8
ASPC-1	7
H69	4.5
NIH 3T3	0.21

Note D-4: Effect of BQGPs on healthy osteoblast cells (MC 3T3)

In order to validate the effect of BQGPs on non-cancerous cells, here, authors have performed new apoptosis experiments for a new non-cancerous osteoblast cell (MC3T3). To study the early and late apoptosis in normal cells (MC3T3), apoptotic assay by flow cytometry was performed. The normal cells (MC3T3) were treated with the BQGPs for 24hours, and supporting Figure SX shows 0.7% of cells undergo apoptosis similar to the other normal cells (NIH 3T3), which show 0.1% of early and late apoptosis.
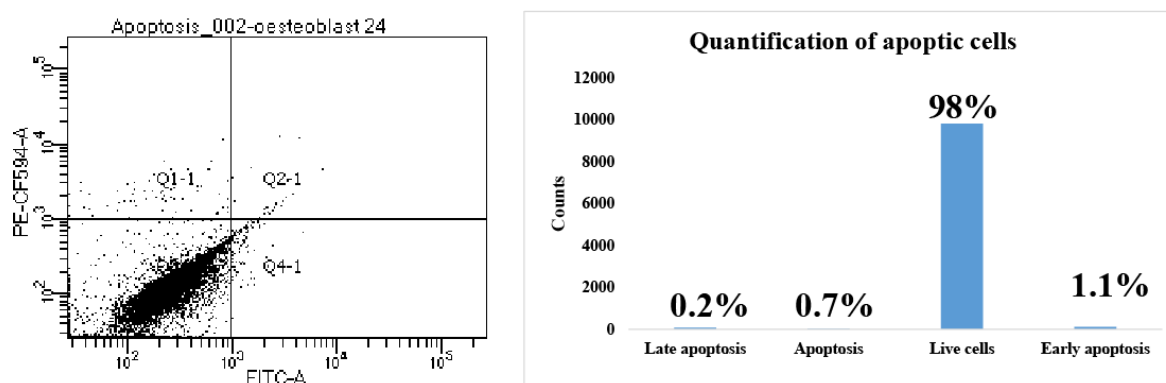
Supporting Figure D-S9 Apoptosis analysis of drug-free BQGPs treated non-cancerous cells (MC3T3) by using flow cytometry

Note D-5 Particle size distribution of silicon nanostructure

The HRTEM images show that there is a bimodal distribution of nanoparticles. Here, we can differentiate the gold QDs from the silicon particles in HRTEM images, due to the difference in the density of the gold and silicon [257], [258]. The dark sphere-like structures in HRTEM images in Supporting Figure S10 corresponds to gold. Hereby using the Image J software, we can calculate the size of gold and silicon particles. Supporting Figure S10 shows the particle size distribution curve for gold and silicon particles separately. The average size of gold QDs synthesized was 3.2 nm, and silicon nanostructures were 10.8 nm.
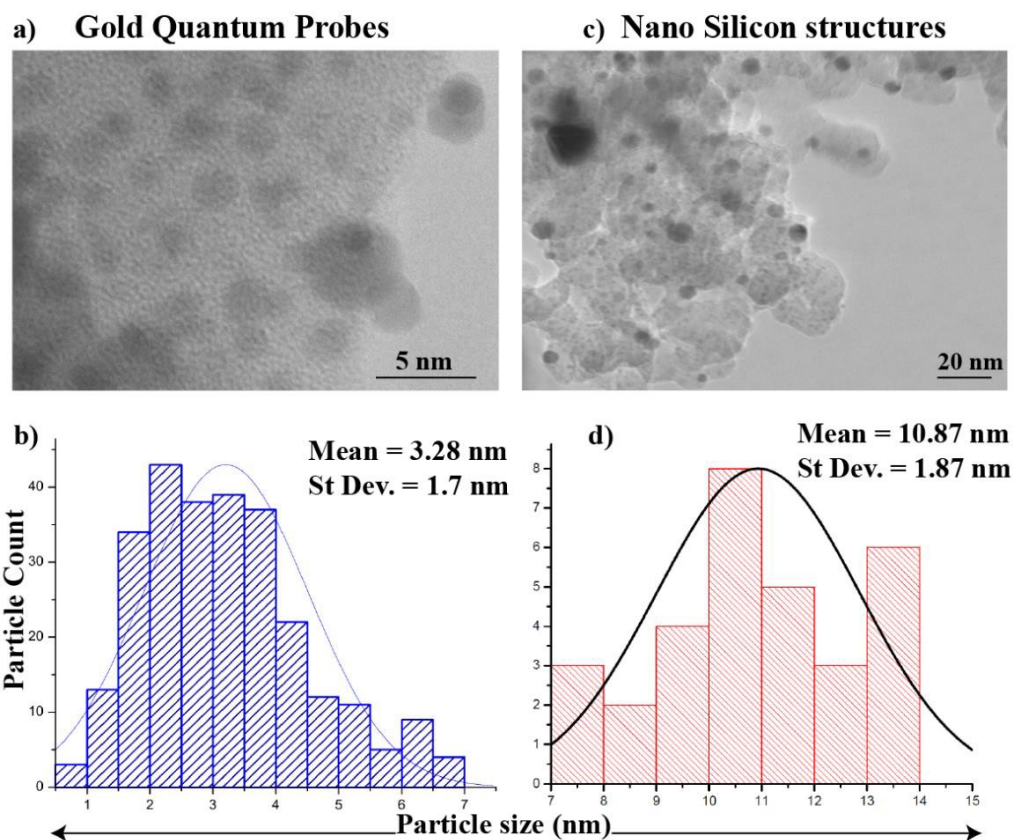
Supporting Figure D-S10 a) The dark spherical structures are bright quantum gold probes and b) shows the particle distribution curve of BQGPs c) shows the Silicon nanostructures and d) shows the particle distribution curve of silicon nanostructure

Note B-6 Cell adhesion on the silicon nanostructure

For efficient theranostics study, it is essential to growing the cancer cells in *in vivo* environment. The presence of silicon structures provides the *in vivo* habitat for cells to adhere and proliferate and allow the cells to grow correspondingly as in *in vivo* environment. **T**o study the structural support provided by the silicon nanoparticles, we have performed new experiments and collected new SEM images shown in Supporting Figure S11. Adding to that, due to the small quantum size, gold QDs uniquely self-mobilizes inside the cells through a passive energy independent mechanism.
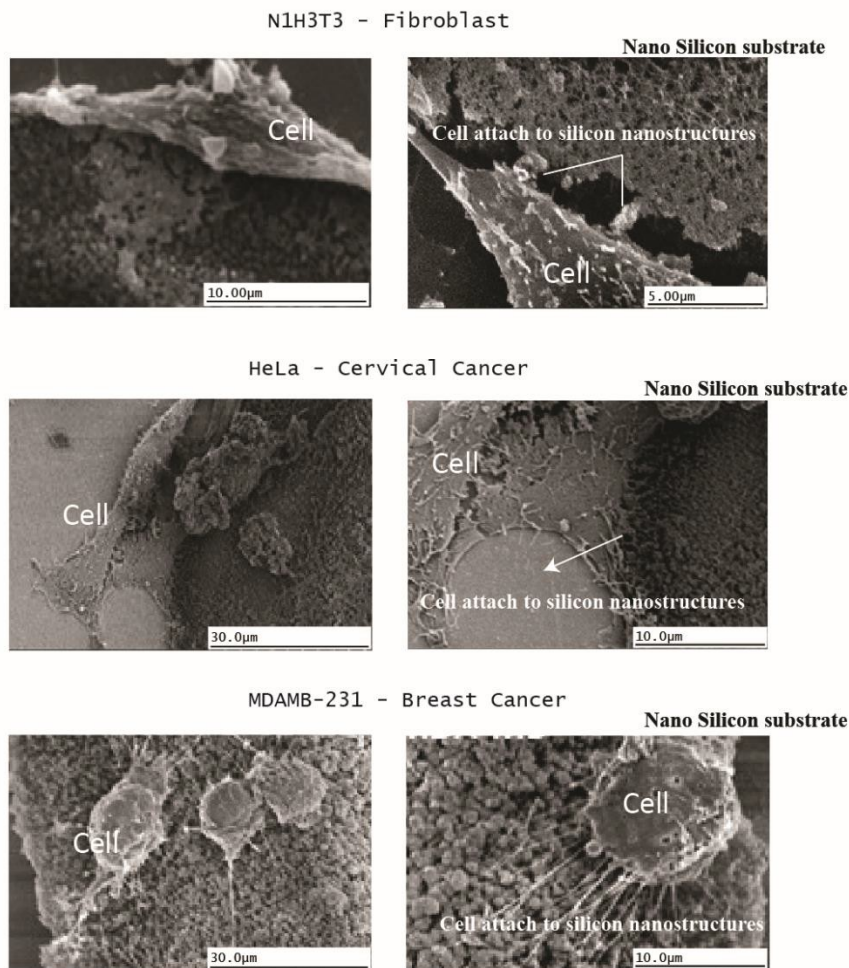
Supporting Figure D-S11 Cell adhesion on the silicon nanostructure, silicon nanostructures provides the support for cells to adhere.

Note D-7 XRD analysis of BQGPs and silicon nanostructures

XRD experiments were performed to characterize the gold QDs-embedded silicon nanoparticles. The peak at 69.21° explains the presence of crystalline silicon, and the peak at 38.22° shows the presence of gold. Other peaks present shows the silicon dioxide and different phases of gold. All the generated peaks show the presence of gold and silicon material individually showed in Supporting Figure S12
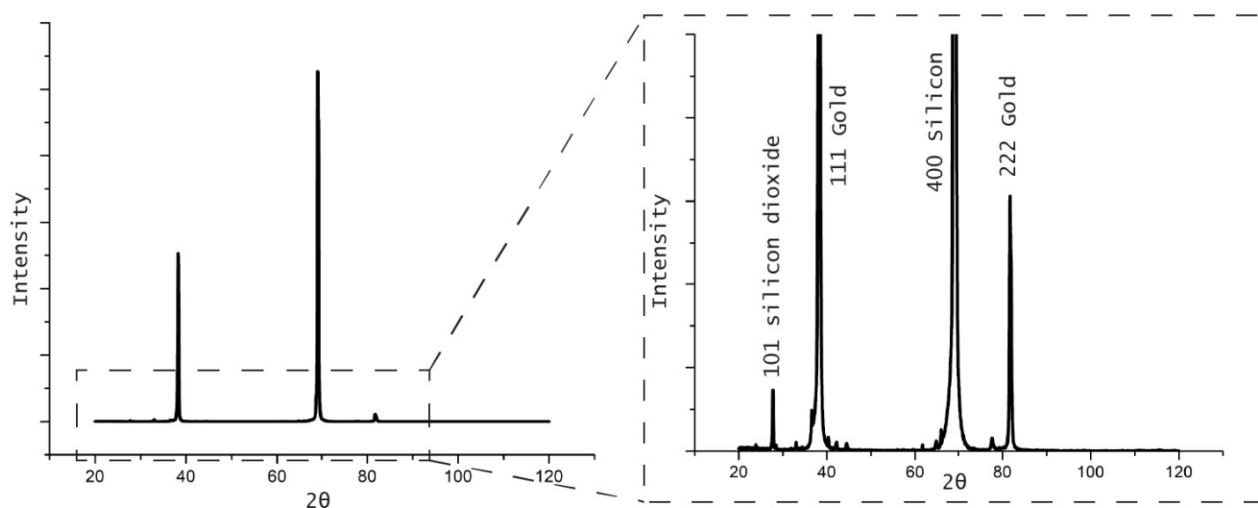
Supporting Figure D-S12 XRD analysis of BQGPs and silicon nanostructures

Note D-8 EDX analysis of BQGPs inside the cells

In order to validate the presence of gold quantum probes inside the cells, we have studied the EDX analysis of the complete cell. EDX analysis shows the presence of gold QDs inside the cells. EDX analysis supports the BioTEM image, and only gold QDs mobilize inside the cells due to the small quantum size of gold QDs. With the support of EDX analysis, we can confirm the increased uptake of gold QDs inside the cancerous cells as compared to the non-cancerous cells. The ED X quantifications show the presence of 7.47 atomic% gold QDs inside the

cancerous cells and 2.56 atomic% of gold QDs inside the non-cancerous cells showed in

Supporting Figure S13.

Cervical cancer cells
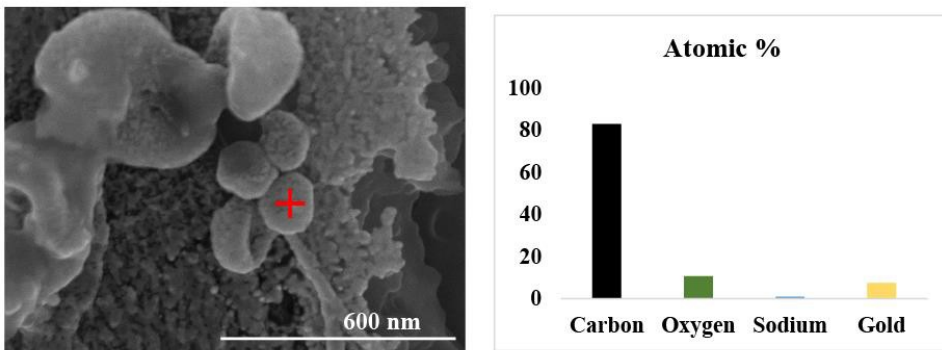
Fibroblast cells
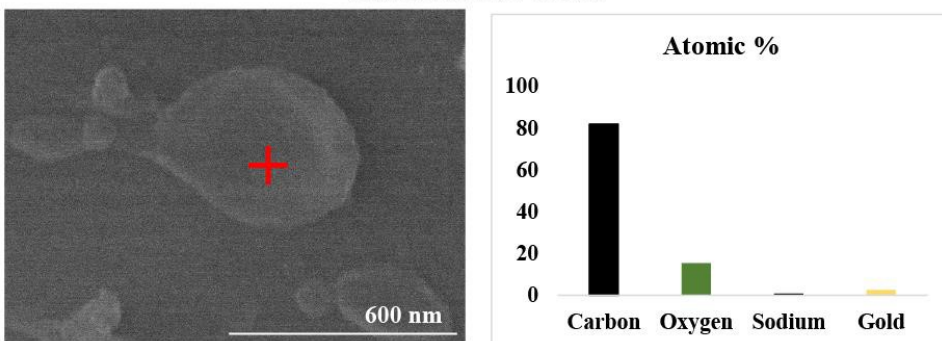
Supporting Figure D-S13 EDX analysis of cancerous and non-cancerous cells for the

quantification of elements

Bibliography

References

[1]   E. C. Dreaden, M. A. MacKey, X. Huang, B. Kang, and M. A. El-Sayed, "Beating cancer in multiple ways using nanogold," *Chem. Soc. Rev.*, vol. 40, no. 7, pp. 3391–3404, 2011, doi: 10.1039/c0cs00180e.

[2]   O. S. Wolfbeis, "An overview of nanoparticles commonly used in fluorescent bioimaging," *Chem. Soc. Rev.*, vol. 44, no. 14, pp. 4743–4768, 2015, doi: 10.1039/c4cs00392f.

[3]   A. S. Thakor, J. Jokerst, C. Zavaleta, T. F. Massoud, and S. S. Gambhir, "Gold nanoparticles: A revival in precious metal administration to patients," *Nano Letters*, vol. 11, no. 10. pp. 4029–4036, 2011, doi: 10.1021/nl202559p.

[4]   A. J. Mieszawska, W. J. M. Mulder, Z. A. Fayad, and D. P. Cormode, "Multifunctional gold nanoparticles for diagnosis and therapy of disease," *Molecular Pharmaceutics*, vol. 10, no. 3. pp. 831–847, 2013, doi: 10.1021/mp3005885.

[5]   G. Chen, I. Roy, C. Yang, and P. N. Prasad, "Nanochemistry and Nanomedicine for Nanoparticle-based Diagnostics and Therapy," 2016, doi: 10.1021/acs.chemrev.5b00148.

[6]   E. C. Dreaden, A. M. Alkilany, X. Huang, C. J. Murphy, and M. A. El-Sayed, "The golden age: Gold nanoparticles for biomedicine," *Chem. Soc. Rev.*, vol. 41, no. 7, pp. 2740–2779, 2012, doi: 10.1039/c1cs15237h.

[7]   J. V. Jokerst, A. J. Cole, D. Van De Sompel, and S. S. Gambhir, "Gold nanorods for ovarian cancer detection with photoacoustic imaging and resection guidance via Raman

imaging in living mice," *ACS Nano*, vol. 6, no. 11, pp. 10366–10377, Nov. 2012, doi: 10.1021/nn304347g.

[8] H. He, C. Xie, and J. Ren, "Nonbleaching fluorescence of gold nanoparticles and its applications in cancer cell imaging," *Anal. Chem.*, 2008, doi: 10.1021/ac8005796.

[9] D. Ho *et al.*, "Intracellular speciation of gold nanorods alters the conformational dynamics of genomic DNA," doi: 10.1038/s41565-018-0272-2.

[10] A. M. Alkilany, P. K. Nagaria, C. R. Hexel, T. J. Shaw, C. J. Murphy, and M. D. Wyatt, "Cellular uptake and cytotoxicity of gold nanorods: Molecular origin of cytotoxicity and surface effects," *Small*, vol. 5, no. 6, pp. 701–708, 2009, doi: 10.1002/smll.200801546.

[11] L. Wang *et al.*, "Surface chemistry of gold nanorods: origin of cell membrane damage and cytotoxicity," doi: 10.1039/c3nr01626a.

[12] F. Philipp Seib, G. T. Jones, J. Rnjak-Kovacina, Y. Lin, and D. L. Kaplan, "pH-Dependent anticancer drug release from silk nanoparticles," doi: 10.1002/adhm.201300034.

[13] J. Palomäki *et al.*, "Long, needle-like carbon nanotubes and asbestos activate the NLRP3 inflammasome through a similar mechanism," *ACS Nano*, vol. 5, no. 9, pp. 6861–6870, 2011, doi: 10.1021/nn200595c.

[14] A. Ambrosi and M. Pumera, "Regulatory Peptides Are Susceptible to Oxidation by Metallic Impurities within Carbon Nanotubes," *Chem. Eur. J*, vol. 16, pp. 1786–1792, 2010, doi: 10.1002/chem.200902534.

[15] Y. Zhang *et al.*, "Mechanistic toxicity evaluation of uncoated and PEGylated single-walled carbon nanotubes in neuronal PC12 cells," *ACS Nano*, vol. 5, no. 9, pp. 7020–

7033, 2011, doi: 10.1021/nn2016259.

[16]   A. M. Alkilany, P. K. Nagaria, C. R. Hexel, T. J. Shaw, C. J. Murphy, and M. D. Wyatt, "Cellular Uptake and Cytotoxicity of Gold Nanorods: Molecular Origin of Cytotoxicity and Surface Effects," doi: 10.1002/smll.200801546.

[17]   S. Tenzer *et al.*, "Rapid formation of plasma protein corona critically affects nanoparticle pathophysiology," 2013, doi: 10.1038/NNANO.2013.181.

[18]   S. T. Zakhidov *et al.*, "Effect of Ultrasmall Gold Nanoparticles on the Murine Native Sperm Chromatin," *Izv. Akad. Nauk Ser. Biol.*, no. 6, pp. 565–572, Nov. 2015.

[19]   N. Feliu, M. Hassan, E. Garcia Rico, D. Cui, W. Parak, and R. Alvarez-Puebla, "SERS Quantification and Characterization of Proteins and Other Biomolecules," *Langmuir*, vol. 33, no. 38, pp. 9711–9730, 2017, doi: 10.1021/acs.langmuir.7b01567.

[20]   H. Lin, J. Mock, D. Smith, T. Gao, and M. J. Sailor, "Surface-enhanced Raman scattering from silver-plated porous silicon," *J. Phys. Chem. B*, vol. 108, no. 31, pp. 11654–11659, 2004, doi: 10.1021/jp049008b.

[21]   T. Vo-Dinh, L. R. Allain, and D. L. Stokes, "Cancer gene detection using surface-enhanced Raman scattering (SERS)," *J. Raman Spectrosc.*, vol. 33, no. 7, pp. 511–516, 2002, doi: 10.1002/jrs.883.

[22]   K. W. Kho, U. S. Dinish, A. Kumar, and M. Olivo, "Frequency shifts in SERS for biosensing," *ACS Nano*, vol. 6, no. 6, pp. 4892–4902, 2012, doi: 10.1021/nn300352b.

[23]   T. Zhang, Y. He, J. Wei, and L. Que, "Nanostructured optical microchips for cancer biomarker detection," *Biosens. Bioelectron.*, vol. 38, no. 1, pp. 382–388, 2012, doi:

10.1016/j.bios.2012.06.029.

[24] C. C. Lin, Y. M. Yang, Y. F. Chen, T. S. Yang, and H. C. Chang, "A new protein A assay based on Raman reporter labeled immunogold nanoparticles," *Biosens. Bioelectron.*, vol. 24, no. 2, pp. 178–183, 2008, doi: 10.1016/j.bios.2008.03.035.

[25] S. J. Soenen *et al.*, "Cytotoxic effects of gold nanoparticles: A multiparametric study," *ACS Nano*, vol. 6, no. 7, pp. 5767–5783, 2012, doi: 10.1021/nn301714n.

[26] B. D. Chithrani, A. A. Ghazani, and W. C. W. Chan, "Determining the size and shape dependence of gold nanoparticle uptake into mammalian cells," *Nano Lett.*, 2006, doi: 10.1021/nl052396o.

[27] C. Izanloo, "Effect of gold nanoparticle on stability of the DNA molecule: A study of molecular dynamics simulation," 2017.

[28] Q. Mu *et al.*, "Chemical basis of interactions between engineered nanoparticles and biological systems," *Chem. Rev.*, vol. 114, no. 15, pp. 7740–7781, 2014, doi: 10.1021/cr400295a.

[29] E. A. Foley, J. D. Carter, F. Shan, and T. Guo, "Enhanced relaxation of nanoparticle-bound supercoiled DNA in X-ray radiation," *Chem. Commun.*, no. 25, pp. 3192–3194, 2005, doi: 10.1039/b503425f.

[30] C. M. McIntosh, E. A. Esposito, A. K. Boal, J. M. Simard, C. T. Martin, and V. M. Rotello, "Inhibition of DNA transcription using cationic mixed monolayer protected gold clusters," *J. Am. Chem. Soc.*, vol. 123, no. 31, pp. 7626–7629, 2001, doi: 10.1021/ja015556g.

[31] J. Yang, J. Y. Lee, H.-P. Too, and G.-M. Chow, "Inhibition of DNA hybridization by small metal nanoparticles," 2005, doi: 10.1016/j.bpc.2005.10.011.

[32] A. Estévez-Torres and D. Baigl, "DNA compaction: Fundamentals and applications," *Soft Matter*, vol. 7, no. 15, pp. 6746–6756, 2011, doi: 10.1039/c1sm05373f.

[33] G. Han, C. T. Martin, and V. M. Rotello, "Stability of Gold Nanoparticle-Bound DNA toward Biological, Physical, and Chemical Agents," doi: 10.1111/j.1747-0285.2005.00324.x.

[34] T. Akitaya, A. Seno, T. Nakai, N. Hazemoto, S. Murata, and K. Yoshikawa, "Weak Interaction Induces an ON/OFF Switch, whereas Strong Interaction Causes Gradual Change: Folding Transition of a Long Duplex DNA Chain by Poly-L-lysine," 2007, doi: 10.1021/bm060634j.

[35] T. S. Hauck, A. A. Ghazani, and W. C. W. Chan, "Assessing the effect of surface chemistry on gold nanorod uptake, toxicity, and gene expression in mammalian cells," *Small*, vol. 4, no. 1, pp. 153–159, 2008, doi: 10.1002/smll.200700217.

[36] J. G. Railsback *et al.*, "Weakly charged cationic nanoparticles induce DNA bending and strand separation," *Adv. Mater.*, vol. 24, no. 31, pp. 4261–4265, 2012, doi: 10.1002/adma.201104891.

[37] M. Vinod, R. S. Jayasree, and K. G. Gopchandran, "Synthesis of pure and biocompatible gold nanoparticles using laser ablation method for SERS and photothermal applications," *Curr. Appl. Phys.*, 2017, doi: 10.1016/j.cap.2017.08.004.

[38] S. A. Aromal, K. V Dinesh Babu, and D. Philip, "Characterization and catalytic activity of

gold nanoparticles synthesized using ayurvedic arishtams," *Spectrochim. Acta Part A Mol. Biomol. Spectrosc.*, vol. 96, pp. 1025–1030, 2012, doi: 10.1016/j.saa.2012.08.010.

[39]   C. D. Walkey *et al.*, "Protein corona fingerprinting predicts the cellular interaction of gold and silver nanoparticles," *ACS Nano*, vol. 8, no. 3, pp. 2439–2455, 2014, doi: 10.1021/nn406018q.

[40]   G. Oberdörster, "Safety assessment for nanotechnology and nanomedicine: Concepts of nanotoxicology," *J. Intern. Med.*, vol. 267, no. 1, pp. 89–105, 2010, doi: 10.1111/j.1365-2796.2009.02187.x.

[41]   A. M. Nyström and B. Fadeel, "Safety assessment of nanomaterials: Implications for nanomedicine," 2012, doi: 10.1016/j.jconrel.2012.01.027.

[42]   H. Akita *et al.*, "Multi-layered nanoparticles for penetrating the endosome and nuclear membrane via a step-wise membrane fusion process," *Biomaterials*, vol. 30, no. 15, pp. 2940–2949, 2009, doi: 10.1016/j.biomaterials.2009.02.009.

[43]   J. Conroy *et al.*, "CdTe nanoparticles display tropism to core histones and histone-rich cell organelles," *Small*, vol. 4, no. 11, pp. 2006–2015, 2008, doi: 10.1002/smll.200800088.

[44]   F. Chen and D. Gerion, "Fluorescent CdSe/ZnS nanocrystal-peptide conjugates for long-term, nontoxic imaging and nuclear targeting in living cells," *Nano Lett.*, vol. 4, no. 10, pp. 1827–1832, 2004, doi: 10.1021/nl049170q.

[45]   A. M. Alkilany and C. J. Murphy, "Toxicity and cellular uptake of gold nanoparticles: What we have learned so far?," *J. Nanoparticle Res.*, vol. 12, no. 7, pp. 2313–2333, 2010, doi: 10.1007/s11051-010-9911-8.

[46] M. Zheng *et al.*, "DNA-assisted dispersion and separation of carbon nanotubes," *Nat. Mater.*, vol. 2, no. 5, pp. 338–342, 2003, doi: 10.1038/nmat877.

[47] G. Han, N. S. Chari, A. Verma, R. Hong, C. T. Martin, and V. M. Rotello, "Controlled recovery of the transcription of nanoparticle-bound DNA by intracellular concentrations of glutathione," *Bioconjug. Chem.*, vol. 16, no. 6, pp. 1356–1359, 2005, doi: 10.1021/bc050173j.

[48] E. A. Foley, J. D. Carter, F. Shan, and T. Guo, "Enhanced relaxation of nanoparticle-bound supercoiled DNA in X-ray radiation," *Chem. Commun.*, no. 25, pp. 3192–3194, 2005, doi: 10.1039/b503425f.

[49] S. J. Hurst, A. K. R. Lytton-Jean, and C. A. Mirkin, "Maximizing DNA loading on a range of gold nanoparticle sizes," *Anal. Chem.*, vol. 78, no. 24, pp. 8313–8318, 2006, doi: 10.1021/ac0613582.

[50] A. R. Wolfe and T. Meehan, "The effect of sodium ion concentration on intrastrand base-pairing in single-stranded DNA," 1994.

[51] A. Wolfe, G. H. Shimer, and T. Meehan, "Polycyclic Aromatic Hydrocarbons Physically Intercalate into Duplex Regions of Denatured DNA," *Biochemistry*, vol. 26, no. 20, pp. 6392–6396, 1987, doi: 10.1021/bi00394a013.

[52] A. R. Wolfe and T. Meehan, "The effect of sodium ion concentration on intrastrand base-pairing in single-stranded DNA," 1994.

[53] "Interplay between Metal Ions and Nucleic Acids," 2012.

[54] S. Peters, "X-ray spectroscopy of deposited noble metal clusters," no. August 2012, 2012.

[55] T. Zou, C. T. Lum, C.-N. Lok, J.-J. Zhang, and C.-M. Che, "Chem Soc Rev Chemical Society Reviews Includes a collection of articles on the theme of molecular medicine and cancer Chemical biology of anticancer gold(III) and gold(I) complexes," *Chem. Soc. Rev.*, vol. 44, p. 8786, 2015, doi: 10.1039/c5cs00132c.

[56] G. Oster, "Principles of polymer chemistry," Cornell Uni-versity Press, 2009.

[57] H. N. Wang and T. Vo-Dinh, "Multiplex detection of breast cancer biomarkers using plasmonic molecular sentinel nanoprobes," *Nanotechnology*, vol. 20, no. 6, p. 6, 2009, doi: 10.1088/0957-4484/20/6/065101.

[58] S. Sloan-Dennison and Z. D. Schultz, "Label-free plasmonic nanostar probes to illuminate in vitro membrane receptor recognition †," 2018, doi: 10.1039/c8sc05035j.

[59] J. Su *et al.*, "Multicolor Gold-Silver Nano-Mushrooms as Ready-to-Use SERS Probes for Ultrasensitive and Multiplex DNA/miRNA Detection," *Anal. Chem.*, vol. 89, no. 4, pp. 2531–2538, 2017, doi: 10.1021/acs.analchem.6b04729.

[60] H. N. Wang, B. M. Crawford, A. M. Fales, M. L. Bowie, V. L. Seewaldt, and T. Vo-Dinh, "Multiplexed Detection of MicroRNA Biomarkers Using SERS-Based Inverse Molecular Sentinel (iMS) Nanoprobes," *J. Phys. Chem. C*, 2016, doi: 10.1021/acs.jpcc.6b03299.

[61] A. Pallaoro, M. R. Hoonejani, G. B. Braun, C. D. Meinhart, and M. Moskovits, "Rapid identification by surface-enhanced raman spectroscopy of cancer cells at low concentrations flowing in a microfluidic channel," *ACS Nano*, vol. 9, no. 4, pp. 4328–4336, 2015, doi: 10.1021/acsnano.5b00750.

[62] D. Cialla, S. Pollok, C. Steinbrücker, K. Weber, and J. Popp, "SERS-based detection of

biomolecules," *Nanophotonics*, vol. 3, no. 6, pp. 383–411, 2014, doi: 10.1515/nanoph-2013-0024.

[63] P. Matteini *et al.*, "Site-Selective Surface-Enhanced Raman Detection of Proteins," *ACS Nano*, vol. 11, no. 1, pp. 918–926, 2017, doi: 10.1021/acsnano.6b07523.

[64] P. Owens, N. Phillipson, J. Perumal, G. M. O'Connor, and M. Olivo, "Sensing of p53 and EGFR biomarkers using high efficiency SERS substrates," *Biosensors*, vol. 5, no. 4, pp. 664–677, 2015, doi: 10.3390/bios5040664.

[65] J. Morla-Folch, H.-N. Xie, R. A. Alvarez-Puebla, and L. Guerrini, "Fast Optical Chemical and Structural Classification of RNA," 2016, doi: 10.1021/acsnano.5b07966.

[66] S. Dick, S. E. J. Bell, K. J. Alexander, I. A. O'neil, and R. Cosstick, "SERS and SERRSDetectionofthe DNA Lesion 8-Nitroguanine: ASelf-LabelingModification," doi: 10.1002/chem.201701791.

[67] E. Papadopoulou and S. E. J. Bell, "Angewandte Chemie DNA Analysis Label-Free Detection of Single-Base Mismatches in DNA by Surface-Enhanced Raman Spectroscopy**," doi: 10.1002/anie.201102776.

[68] L.-J. Xu, Z.-C. Lei, J. Li, C. Zong, C. James Yang, and B. Ren, "Label-Free Surface-Enhanced Raman Spectroscopy Detection of DNA with Single-Base Sensitivity," 2015, doi: 10.1021/jacs.5b01426.

[69] S. R. Panikkanvalappil, M. A. MacKey, and M. A. El-Sayed, "Probing the unique dehydration-induced structural modifications in cancer cell DNA using surface enhanced Raman spectroscopy," *J. Am. Chem. Soc.*, vol. 135, no. 12, pp. 4815–4821, 2013, doi:

10.1021/ja400187b.

[70] S. R. Panikkanvalappil, M. A. Mahmoud, M. A. MacKey, and M. A. El-Sayed, "Surface-enhanced raman spectroscopy for real-time monitoring of reactive oxygen species-induced DNA damage and its prevention by platinum nanoparticles," *ACS Nano*, vol. 7, no. 9, pp. 7524–7533, 2013, doi: 10.1021/nn403722x.

[71] M. Masetti, H. Xie, eljka Krpetic, M. Recanatini, R. A. Alvarez-Puebla, and L. Guerrini, "Revealing DNA Interactions with Exogenous Agents by Surface-Enhanced Raman Scattering," *J. Am. Chem. Soc*, vol. 137, p. 32, 2015, doi: 10.1021/ja511398w.

[72] J. Wang, K. M. Koo, E. J. H. Wee, Y. Wang, and M. Trau, "A nanoplasmonic label-free surface-enhanced Raman scattering strategy for non-invasive cancer genetic subtyping in patient samples †," 2017, doi: 10.1039/c6nr09928a.

[73] B. Kang, L. A. Austin, and M. A. El-Sayed, "Observing Real-Time Molecular Event Dynamics of Apoptosis in Living Cancer Cells using Nuclear-Targeted Plasmonically Enhanced Raman Nanoprobes," 2014, doi: 10.1021/nn500840x.

[74] M. L. Coluccio *et al.*, "Detection of single amino acid mutation in human breast cancer by disordered plasmonic self-similar chain," *Sci. Adv.*, vol. 1, no. 8, p. e1500487, Sep. 2015, doi: 10.1126/sciadv.1500487.

[75] T. Yoon Jeon, D. Jae Kim, S.-G. Park, S.-H. Kim, and D.-H. Kim, "Nanostructured plasmonic substrates for use as SERS sensors," *Nano Converg.*, vol. 3, p. 18, 2016, doi: 10.1186/s40580-016-0078-6.

[76] S. Zhao *et al.*, "Ultrasensitive SERS detection of VEGF based on a self-assembled Ag

ornamented-AU pyramid superstructure," 2016, doi: 10.1016/j.bios.2015.01.056.

[77]   P. Wang *et al.*, "Label-Free SERS Selective Detection of Dopamine and Serotonin Using Graphene-Au Nanopyramid Heterostructure," *Anal. Chem.*, vol. 87, no. 20, pp. 10255–10261, 2015, doi: 10.1021/acs.analchem.5b01560.

[78]   S. Behzadi *et al.*, "Cellular uptake of nanoparticles: journey inside the cell," *Chem. Soc. Rev.*, vol. 46, no. 14, pp. 4218–4244, 2017, doi: 10.1039/C6CS00636A.

[79]   P. J. Chueh, R. Y. Liang, Y. H. Lee, Z. M. Zeng, and S. M. Chuang, "Differential cytotoxic effects of gold nanoparticles in different mammalian cell lines," *J. Hazard. Mater.*, vol. 264, no. 2014, pp. 303–312, 2014, doi: 10.1016/j.jhazmat.2013.11.031.

[80]   P. K. Jain, I. H. ElSayed, and M. A. El-Sayed, "Au nanoparticles target cancer," *Nano Today*, vol. 2, no. 1, pp. 18–29, 2007, doi: 10.1016/S1748-0132(07)70016-6.

[81]   X. Qian *et al.*, "In vivo tumor targeting and spectroscopic detection with surface-enhanced Raman nanoparticle tags," *Nat. Biotechnol.*, vol. 26, no. 1, pp. 83–90, 2008, doi: 10.1038/nbt1377.

[82]   L. Jensen, C. M. Aikens, and G. C. Schatz, "Electronic structure methods for studying surface-enhanced Raman scattering," doi: 10.1039/b706023h.

[83]   J. N. Anker, W. P. Hall, O. Lyandres, N. C. Shah, J. Zhao, and R. P. Van Duyne, "Biosensing with plasmonic nanosensors," *Nature Materials*. 2008, doi: 10.1038/nmat2162.

[84]   M. S. Wilson and W. Nie, "Multiplex measurement of seven tumor markers using an electrochemical protein chip," *Anal. Chem.*, vol. 78, no. 18, pp. 6476–6483, 2006, doi:

10.1021/ac060843u.

[85]   J. J. Gregory and J. L. Finlay, "Alpha-fetoprotein and beta-human chorionic gonadotropin: their clinical significance as tumour markers.," *Drugs*, vol. 57, no. 4, pp. 463–7, Apr. 1999.

[86]   N. Wentzensen, M. Von, and K. Doeberitz, "Biomarkers in cervical cancer screening," *Dis. Markers*, vol. 23, pp. 315–330, 2007.

[87]   E.-K. Yim and J.-S. Park, "The Role of HPV E6 and E7 Oncoproteins in HPV-associated Cervical Carcinogenesis," *Cancer Res Treat*, vol. 37, no. 6, pp. 319–324, 2005.

[88]   X. Kang *et al.*, "Photothermal therapeutic application of gold nanorods-porphyrin-trastuzumab complexes in HER2-positive breast cancer," *Sci. Rep.*, 2017, doi: 10.1038/srep42069.

[89]   S. Lee *et al.*, "Surface-enhanced Raman scattering imaging of HER2 cancer markers overexpressed in single MCF7 cells using antibody conjugated hollow gold nanospheres," *Biosens. Bioelectron.*, vol. 24, no. 7, pp. 2260–2263, 2009, doi: 10.1016/j.bios.2008.10.018.

[90]   Y. Liu *et al.*, "Detection and Identification of Estrogen Based on Surface-Enhanced Resonance Raman Scattering (SERRS)," *Molecules*, vol. 23, no. 6, p. 1330, 2018, doi: 10.3390/molecules23061330.

[91]   Q. Mu *et al.*, "Chemical basis of interactions between engineered nanoparticles and biological systems," *Chem. Rev.*, vol. 114, no. 15, pp. 7740–7781, 2014, doi: 10.1021/cr400295a.

[92]   G. Sonavane, K. Tomoda, and K. Makino, "Biodistribution of colloidal gold nanoparticles after intravenous administration: Effect of particle size," *Colloids Surfaces B Biointerfaces*, vol. 66, pp. 274–280, 2008, doi: 10.1016/j.colsurfb.2008.07.004.

[93]   W. H. De Jong, W. I. Hagens, P. Krystek, M. C. Burger, A. J. A. M. Sips, and R. E. Geertsma, "Particle size-dependent organ distribution of gold nanoparticles after intravenous administration," *Biomaterials*, vol. 29, no. 12, pp. 1912–1919, 2008, doi: 10.1016/j.biomaterials.2007.12.037.

[94]   B. Devika Chithrani and W. C. W. Chan, "Elucidating the Mechanism of Cellular Uptake and Removal of Protein-Coated Gold Nanoparticles of Different Sizes and Shapes," 2007, doi: 10.1021/nl070363y.

[95]   M. Semmler-Behnke *et al.*, "Biodistribution of 1.4- and 18-nm gold particles in rats," *Small*, vol. 4, no. 12, pp. 2108–2111, 2008, doi: 10.1002/smll.200800922.

[96]   G. S. Terentyuk *et al.*, "Circulation and distribution of gold nanoparticles and induced alterations of tissue morphology at intravenous particle delivery," *J. Biophotonics*, vol. 2, no. 5, pp. 292–302, 2009, doi: 10.1002/jbio.200910005.

[97]   A. B. Etame, C. A. Smith, W. C. W. Chan, and J. T. Rutka, "Design and potential application of PEGylated gold nanoparticles with size-dependent permeation through brain microvasculature," *Nanomedicine Nanotechnology, Biol. Med.*, vol. 7, no. 6, pp. 992–1000, 2011, doi: 10.1016/j.nano.2011.04.004.

[98]   E. Cepeda-Pérez *et al.*, "SERS and integrative imaging upon internalization of quantum dots into human oral epithelial cells," *J. Biophotonics*, vol. 9, no. 7, pp. 683–693, 2016, doi: 10.1002/jbio.201600034.

[99] C. Schaeffer and C. Strausser, "Data for General, Organic, and Physical Chemistry," 1989.

[100] M. P. Casaletto, A. Longo, A. Martorana, A. Prestianni, and A. M. Venezia, "XPS study of supported gold catalysts: the role of Au 0 and Au +d species as active sites," *Surf. INTERFACE Anal. Surf. Interface Anal*, vol. 38, pp. 215–218, 2006, doi: 10.1002/sia.2180.

[101] P. Tarakeshwar, D. Finkelstein-Shapiro, S. J. Hurst, T. Rajh, and V. Mujica, "Surface-enhanced Raman scattering on semiconducting oxide nanoparticles: Oxide nature, size, solvent, and pH effects," *J. Phys. Chem. C*, 2011, doi: 10.1021/jp202590e.

[102] K. Unfried, C. Albrecht, L. O. Klotz, A. Von Mikecz, S. Grether-Beck, and R. P. F. Schins, "Cellular responses to nanoparticles: Target structures and mechanisms," *Nanotoxicology*, vol. 1, no. 1, pp. 52–71, 2007, doi: 10.1080/00222930701314932.

[103] Y. Xiao, S. P. Forry, X. Gao, R. D. Holbrook, W. G. Telford, and A. Tona, "Dynamics and mechanisms of quantum dot nanoparticle cellular uptake," *J. Nanobiotechnology*, vol. 8, 2010.

[104] L. W. Zhang and N. A. Monteiro-Riviere, "Mechanisms of quantum dot nanoparticle cellular uptake," *Toxicol. Sci.*, vol. 110, no. 1, pp. 138–155, 2009, doi: 10.1093/toxsci/kfp087.

[105] V. Belli, D. Guarnieri, M. Biondi, F. Della Sala, and P. A. Netti, "Dynamics of nanoparticle diffusion and uptake in three-dimensional cell cultures," *Colloids Surfaces B Biointerfaces*, vol. 149, pp. 7–15, 2017, doi: 10.1016/j.colsurfb.2016.09.046.

[106] X. Jiang, J. Jiang, Y. Jin, E. Wang, and S. Dong, "Effect of Colloidal Gold Size on the Conformational Changes of Adsorbed Cytochrome c: Probing by Circular Dichroism, UV-Visible, and Infrared Spectroscopy," doi: 10.1021/bm049744l.

[107] Y. Liu, W. Meyer-Zaika, S. Franzka, G. Schmid, M. Tsoli, and H. Kuhn, "Gold-cluster degradation by the transition of B-DNA into A-DNA and the formation of nanowires," *Angew. Chemie - Int. Ed.*, vol. 42, no. 25, pp. 2853–2857, 2003, doi: 10.1002/anie.200250235.

[108] A. Parrales and T. Iwakuma, "p53 as a Regulator of Lipid Metabolism in Cancer," *Int. J. Mol. Sci.*, 2016, doi: 10.3390/ijms17122074.

[109] A. Downes and A. Elfick, "Raman spectroscopy and related techniques in biomedicine," *Sensors*, vol. 10, no. 3, pp. 1871–1889, 2010, doi: 10.3390/s100301871.

[110] A. A. Changavi, A. Shashikala, and A. S. Ramji, "Epidermal Growth Factor Receptor Expression in Triple Negative and Nontriple Negative Breast Carcinomas.," *J. Lab. Physicians*, vol. 7, no. 2, pp. 79–83, 2015, doi: 10.4103/0974-2727.163129.

[111] X. Dai, H. Cheng, Z. Bai, and J. Li, "Breast cancer cell line classification and Its relevance with breast tumor subtyping," *Journal of Cancer*, vol. 8, no. 16. pp. 3131–3141, 2017, doi: 10.7150/jca.18457.

[112] H. S. Park *et al.*, "High EGFR gene copy number predicts poor outcome in triple-negative breast cancer," *Mod. Pathol.*, vol. 27, no. 9, pp. 1212–1222, 2014, doi: 10.1038/modpathol.2013.251.

[113] L. Wang *et al.*, "Evaluation of Raman spectroscopy for diagnosing EGFR mutation status

in lung adenocarcinoma," 2014, doi: 10.1039/c3an01381b.

[114] J. Zhu *et al.*, "Surface-enhanced Raman spectroscopy investigation on human breast cancer cells," *Chem. Cent. J.*, vol. 7, no. 1, p. 1, 2013, doi: 10.1186/1752-153X-7-37.

[115] M. Liang, M. Pan, J. Hu, F. Wang, and X. Liu, "Electrochemical Biosensor for MicroRNA Detection Based on Cascade Hybridization Chain Reaction," *ChemElectroChem*, vol. 5, no. 10, pp. 1380–1386, 2018, doi: 10.1002/celc.201800255.

[116] D. Chaturvedi, S. A. Balaji, V. K. Bn, F. Ariese, S. Umapathy, and A. Rangarajan, "Different phases of breast cancer cells: Raman study of immortalized, transformed, and invasive cells," *Biosensors*, vol. 6, no. 4, 2016, doi: 10.3390/bios6040057.

[117] U. S. Dinish, G. Balasundaram, Y.-T. Chang, and M. Olivo, "Actively Targeted In Vivo Multiplex Detection of Intrinsic Cancer Biomarkers Using Biocompatible SERS Nanotags," 2014, doi: 10.1038/srep04075.

[118] P. Gao *et al.*, "Review Article The Clinical Application of Raman Spectroscopy for Breast Cancer Detection," vol. 2017, no. 1, 2017.

[119] P. R. T. Jess, D. D. W. Smith, M. Mazilu, K. Dholakia, A. C. Riches, and C. S. Herrington, "Early detection of cervical neoplasia by Raman spectroscopy," *Int. J. Cancer*, vol. 121, no. 12, pp. 2723–2728, 2007, doi: 10.1002/ijc.23046.

[120] D. H. Kim *et al.*, "Raman chemical mapping reveals site of action of HIV protease inhibitors in HPV16 E6 expressing cervical carcinoma cells," *Anal. Bioanal. Chem.*, vol. 398, no. 7–8, pp. 3051–3061, 2010, doi: 10.1007/s00216-010-4283-6.

[121] X. Bi, B. Rexer, C. L. Arteaga, M. Guo, and A. Mahadevan-Jansen, "Evaluating HER2

amplification status and acquired drug resistance in breast cancer cells using Raman spectroscopy," 2014, doi: 10.1117/1.JBO.19.2.025001.

[122] R. A. Defilippis, E. C. Goodwin, L. Wu, and D. Dimaio, "Endogenous Human Papillomavirus E6 and E7 Proteins Differentially Regulate Proliferation, Senescence, and Apoptosis in HeLa Cervical Carcinoma Cells," *J. Virol.*, vol. 77, no. 2, pp. 1551–1563, 2003, doi: 10.1128/JVI.77.2.1551-1563.2003.

[123] T. Crook, J. A. Tidy, and K. H. Vousden, "Degradation of ~53 Can Be Targeted by HPV E6 Sequences Distinct from Those Required for ~53 Binding and Trans-Activation," 1991.

[124] N. Wentzensen, M. Von, and K. Doeberitz, "Biomarkers in cervical cancer screening," *Dis. Markers*, vol. 23, pp. 315–330, 2007.

[125] A. A. Wright *et al.*, "Oncogenic mutations in cervical cancer: genomic differences between adenocarcinomas and squamous cell carcinomas of the cervix," *Cancer Novemb.*, vol. 1, no. 11921, pp. 3776–3783, 2013, doi: 10.1002/cncr.28288.

[126] F. M. Lyng, D. Traynor, I. R. M. Ramos, F. Bonnier, and H. J. Byrne, "Raman spectroscopy for screening and diagnosis of cervical cancer," *Anal. Bioanal. Chem.*, 2015, doi: 10.1007/s00216-015-8946-1.

[127] J.-S. Park and E.-K. Yim, "Biomarkers in Cervical Cancer," *Biomark. Insights*, vol. 1, pp. 215–225, 2006.

[128] "The Cell Cycle, Mitosis and Meiosis — University of Leicester." [Online]. Available: https://www2.le.ac.uk/projects/vgec/highereducation/topics/cellcycle-mitosis-meiosis.

[Accessed: 05-Mar-2019].

[129]   Y. Oshima, H. Shinzawa, T. Takenaka, and C. Furihata, "Discrimination analysis of human lung cancer cells associated with histological type and malignancy using Raman spectroscopy," vol. 15, no. February 2010, pp. 1–8, 2019, doi: 10.1117/1.3316296.

[130]   W. Xie *et al.*, "Nuclear Targeted Nanoprobe for Single Living Cell Detection by Surface-Enhanced Raman Scattering," doi: 10.1021/bc800469g.

[131]   K. Kneipp, H. Kneipp, and J. Kneipp, "Surface-Enhanced Raman Scattering in Local Optical Fields of Silver and Gold NanoaggregatessFrom Single-Molecule Raman Spectroscopy to Ultrasensitive Probing in Live Cells," 2006, doi: 10.1021/ar050107x.

[132]   B. Kang, L. A. Austin, and M. A. El-Sayed, "Real-Time Molecular Imaging throughout the Entire Cell Cycle by Targeted Plasmonic-Enhanced Rayleigh/Raman Spectroscopy," 2012, doi: 10.1021/nl3027586.

[133]   I. Notingher *et al.*, "Discrimination between ricin and sulphur mustard toxicity in vitro using Raman spectroscopy," *J. R. Soc. Interface*, vol. 1, no. 1, pp. 79–90, 2004, doi: 10.1098/rsif.2004.0008.

[134]   Z. Movasaghi, S. Rehman, and I. U. Rehman, "Raman spectroscopy of biological tissues," *Applied Spectroscopy Reviews*. 2007, doi: 10.1080/05704920701551530.

[135]   N. Stone, C. Kendall, J. Smith, P. Crow, and H. Barr, "Raman spectroscopy for identification of epithelial cancers," *Faraday Discuss.*, vol. 126, no. May 2003, p. 141, 2004, doi: 10.1039/b304992b.

[136]   J. W. Chan, D. S. Taylor, T. Zwerdling, S. M. Lane, K. Ihara, and T. Huser, "Micro-raman

spectroscopy detects individual neoplastic and normal hematopoietic cells," *Biophys. J.*, vol. 90, no. 2, pp. 648–656, 2006, doi: 10.1529/biophysj.105.066761.

[137] J. Binoy, J. P. Abraham, I. H. Joe, V. S. Jayakumar, G. R. Pettit, and O. F. Nielsen, "NIR-FT Raman and FT-IR spectral studies and ab initio calculations of the anti-cancer drug combretastatin-A4," *J. Raman Spectrosc.*, vol. 35, no. 11, pp. 939–946, 2004, doi: 10.1002/jrs.1236.

[138] S. Phetsang *et al.*, "Investigation of a gold quantum dot/plasmonic gold nanoparticle system for improvement of organic solar cells †," 2019, doi: 10.1039/c8na00119g.

[139] L. A. Austin, B. Kang, M. A. El-Sayed, and M. A. El-Sayed, "ScienceDirect Probing molecular cell event dynamics at the single-cell level with targeted plasmonic gold nanoparticles: A review," *Nano Today*, vol. 10, pp. 542–558, 2015, doi: 10.1016/j.nantod.2015.07.005.

[140] J. D. Jackson and R. F. Fox, "Classical Electrodynamics, 3rd ed," *Cit. Am. J. Phys.*, vol. 67, p. 841, 1999, doi: 10.1119/1.19136.

[141] J. Piella, "Size-Dependent Protein − Nanoparticle Interactions in Citrate- Stabilized Gold Nanoparticles: The Emergence of the Protein Corona," 2017, doi: 10.1021/acs.bioconjchem.6b00575.

[142] S. Goy-Lópezlópez *et al.*, "Physicochemical Characteristics of Protein−NP Bioconjugates: The Role of Particle Curvature and Solution Conditions on Human Serum Albumin Conformation and Fibrillogenesis Inhibition," 2012, doi: 10.1021/la300402w.

[143] J. F. Hillyer and R. M. Albrecht, "Gastrointestinal persorption and tissue distribution of

differently sized colloidal gold nanoparticles," 2001.

[144] Q. Mu *et al.*, "Chemical basis of interactions between engineered nanoparticles and biological systems," *Chem. Rev.*, vol. 114, no. 15, pp. 7740–7781, 2014, doi: 10.1021/cr400295a.

[145] B. D. Chithrani, A. A. Ghazani, and W. C. W. Chan, "Determining the size and shape dependence of gold nanoparticle uptake into mammalian cells," *Nano Lett.*, vol. 6, no. 4, pp. 662–668, 2006, doi: 10.1021/nl052396o.

[146] L.-J. Xu, Z.-C. Lei, J. Li, C. Zong, C. James Yang, and B. Ren, "Label-Free Surface-Enhanced Raman Spectroscopy Detection of DNA with Single-Base Sensitivity," 2015, doi: 10.1021/jacs.5b01426.

[147] G. R. Sant, K. B. Knopf, and D. M. Albala, "Live-single-cell phenotypic cancer biomarkers-future role in precision oncology?," *npj Precis. Oncol.*, vol. 1, no. 1, Dec. 2017, doi: 10.1038/s41698-017-0025-y.

[148] C. A. K Borrebaeck, "Precision diagnostics: moving towards protein biomarker signatures of clinical utility in cancer," 2017.

[149] L. Guerrini and R. A. Alvarez-Puebla, "Surface-enhanced raman spectroscopy in cancer diagnosis, prognosis and monitoring," *Cancers*, vol. 11, no. 6. MDPI AG, 01-Jun-2019, doi: 10.3390/cancers11060748.

[150] A. Kim, M. H. Jang, S. J. Lee, and Y. K. Bae, "Mutations of the epidermal growth factor receptor gene in triple-negative breast cancer," *J. Breast Cancer*, vol. 20, no. 2, pp. 150–159, 2017, doi: 10.4048/jbc.2017.20.2.150.

[151] R. Lappano and M. Maggiolini, "G protein-coupled receptors: Novel targets for drug discovery in cancer," *Nature Reviews Drug Discovery*, 2011. [Online]. Available: https://search-proquest-com.ezproxy.lib.ryerson.ca/docview/821746396?accountid=13631. [Accessed: 02-Dec-2019].

[152] A. J. Deans and S. C. West, "DNA interstrand crosslink repair and cancer," *Nature Reviews Cancer*, 2011. [Online]. Available: https://search-proquest-com.ezproxy.lib.ryerson.ca/docview/881363878?accountid=13631. [Accessed: 02-Dec-2019].

[153] L. Guerrini and R. A. Alvarez-Puebla, "Surface-Enhanced Raman Spectroscopy in Cancer Diagnosis, Prognosis and Monitoring," *Cancers (Basel).*, vol. 11, no. 6, p. 748, 2019, doi: 10.3390/cancers11060748.

[154] H. R. Culver, M. E. Wechsler, and N. A. Peppas, "Label-Free Detection of Tear Biomarkers Using Hydrogel-Coated Gold Nanoshells in a Localized Surface Plasmon Resonance-Based Biosensor," *ACS Nano*, vol. 12, no. 9, pp. 9342–9354, 2018, doi: 10.1021/acsnano.8b04348.

[155] C. M. Muntean, N. Leopold, A. Halmagyi, and S. Valimareanu, "Surface-enhanced Raman spectroscopy of DNA from leaves of in vitro grown apple plants," *J. Raman Spectrosc.*, vol. 42, no. 4, pp. 844–850, 2011, doi: 10.1002/jrs.2780.

[156] S. Nie and S. R. Emory, "Probing single molecules and single nanoparticles by surface-enhanced Raman scattering," *Science (80-.).*, vol. 275, no. 5303, pp. 1102–1106, 1997, doi: 10.1126/science.275.5303.1102.

[157] J. I. A. Rashid and N. A. Yusof, "The strategies of DNA immobilization and hybridization detection mechanism in the construction of electrochemical DNA sensor: A review," *Sensing and Bio-Sensing Research*, vol. 16. Elsevier B.V., pp. 19–31, 01-Nov-2017, doi: 10.1016/j.sbsr.2017.09.001.

[158] J. I. A. Rashid and N. A. Yusof, "The strategies of DNA immobilization and hybridization detection mechanism in the construction of electrochemical DNA sensor: A review," *Sensing and Bio-Sensing Research*, 2017. [Online]. Available: https://reader.elsevier.com/reader/sd/pii/S2214180417300788?token=1FE370514F791D3 D13F3735AEFEB3E4A8498C63CEE48B03E04F176E3A8A564F379F1B705A19A475D A39953AA12B4CEB6. [Accessed: 02-Dec-2019].

[159] H. Shin, H. Jeong, J. Park, S. Hong, and Y. Choi, "Correlation between Cancerous Exosomes and Protein Markers Based on Surface-Enhanced Raman Spectroscopy (SERS) and Principal Component Analysis (PCA)," *ACS Sensors*, vol. 3, no. 12, pp. 2637–2643, 2018, doi: 10.1021/acssensors.8b01047.

[160] A. Agarwal, K. Venkatakrishnan, and B. Tan, "Cancer signaling by plasmonic quantum probes," *Appl. Mater. Today*, vol. 18, p. 100465, 2019, doi: 10.1016/j.apmt.2019.100465.

[161] A. Agarwal, K. Venkatakrishnan, and B. Tan, "Small Gold Quantum Probes for Drug-Free Cancer Theranostics," *Adv. Ther.*, vol. 2, no. 10, p. 1900051, 2019, doi: 10.1002/adtp.201900051.

[162] S. Ganesh, K. Venkatakrishnan, and B. Tan, "Quantum cytosensor for early detection of cancer," *Med. Devices Sensors*, pp. 1–14, 2020, doi: 10.1002/mds3.10058.

[163] J. A. Powell, K. Venkatakrishnan, and B. Tan, "Hybridized enhancement of the SERS

detection of chemical and bio-marker molecules through Au nanosphere ornamentation of hybrid amorphous/crystalline Si nanoweb nanostructure biochip devices," *J. Mater. Chem. B*, vol. 4, no. 34, pp. 5713–5728, 2016, doi: 10.1039/C6TB01301E.

[164] J. A. Powell, K. Venkatakrishnan, and B. Tan, "Toward Universal SERS Detection of Disease Signaling Bioanalytes Using 3D Self-Assembled Nonplasmonic near-Quantum-Scale Silicon Probe," *ACS Appl. Mater. Interfaces*, vol. 9, no. 46, pp. 40127–40142, 2017, doi: 10.1021/acsami.7b15393.

[165] J. Alexander Powell, K. Venkatakrishnan, and B. Tan, "A primary SERS-active interconnected Si-nanocore network for biomolecule detection with plasmonic nanosatellites as a secondary boosting mechanism," *RSC Adv.*, vol. 7, no. 53, pp. 33688–33700, 2017, doi: 10.1039/c7ra01970j.

[166] J. A. Powell, K. Venkatakrishnan, and B. Tan, "Programmable SERS active substrates for chemical and biosensing applications using amorphous/crystalline hybrid silicon nanomaterial," *Sci. Rep.*, vol. 6, no. August 2015, pp. 1–13, 2016, doi: 10.1038/srep19663.

[167] S. Krishnamurthy, A. Esterle, N. C. Sharma, and S. V Sahi, "Yucca-derived synthesis of gold nanomaterial and their catalytic potential," *Nanoscale Res. Lett.*, 2014, doi: 10.1186/1556-276X-9-627.

[168] K. Sneha, M. Sathishkumar, S. Kim, and Y.-S. Yun, "Counter ions and temperature incorporated tailoring of biogenic gold nanoparticles," *Process Biochem.*, vol. 45, pp. 1450–1458, 2010, doi: 10.1016/j.procbio.2010.05.019.

[169] A. Sohrabi Kashani *et al.*, "Uptake of Medium-size Gold Particles in the Nucleus of

Living cells," *Angew. Chemie Int. Ed.*, vol. 53, no. 46, pp. 970–978, doi: 10.11159/tann18.109.

[170] M. Kafshgari, F. Harding, and N. Voelcker, "Insights into Cellular Uptake of Nanoparticles," *Curr. Drug Deliv.*, vol. 12, no. 1, pp. 63–77, 2015, doi: 10.2174/1567201811666140821110631.

[171] T. D. Allen, J. M. Cronshaw, S. Bagley, E. Kiseleva, and M. W. Goldberg, "The nuclear pore complex: Mediator of translocation between nucleus and cytoplasm," *J. Cell Sci.*, vol. 113, no. 10, pp. 1651–1659, 2000.

[172] H. Akita *et al.*, "Multi-layered nanoparticles for penetrating the endosome and nuclear membrane via a step-wise membrane fusion process," 2009, doi: 10.1016/j.biomaterials.2009.02.009.

[173] F. Chen and D. Gerion, "Fluorescent CdSe/ZnS nanocrystal-peptide conjugates for long-term, nontoxic imaging and nuclear targeting in living cells," *Nano Lett.*, vol. 4, no. 10, pp. 1827–1832, 2004, doi: 10.1021/nl049170q.

[174] W. T. Godbey, K. K. Wut, and A. G. Mikost, "Tracking the Intracellular Path of Poly (ethylenimine)/ DNA Complexes for Gene Delivery Author (s): W . T . Godbey , Kenneth K . Wu and Antonios G . Mikos Source : Proceedings of the National Academy of Sciences of the United States of America , Publi," vol. 96, no. 9, pp. 5177–5181, 2019.

[175] D. Görlich, "Transport into and out of the cell nucleus," *EMBO J.*, vol. 17, no. 10, pp. 2721–2727, 1998, doi: 10.1093/emboj/17.10.2721.

[176] C. M. Feldherr and D. Akin, "Regulation of nuclear transport in proliferating and

quiescent cells," *Experimental Cell Research*, vol. 205, no. 1. pp. 179–186, 1993, doi: 10.1006/excr.1993.1073.

[177] A. G. Tkachenko *et al.*, "Multifunctional gold nanoparticle-peptide complexes for nuclear targeting," *J. Am. Chem. Soc.*, vol. 125, no. 16, pp. 4700–4701, 2003, doi: 10.1021/ja0296935.

[178] P. Nativo, I. A. Prior, and M. Brust, "Uptake and Intracellular Fate of Surface- Modified Gold Nanoparticles," doi: 10.1021/nn800330a.

[179] B. Kang, M. A. Mackey, and M. A. El-Sayed, "Nuclear targeting of gold nanoparticles in cancer cells induces DNA damage, causing cytokinesis arrest and apoptosis," *J. Am. Chem. Soc.*, 2010, doi: 10.1021/ja9102698.

[180] S. Jain, K. T. Butterworth, L. E. Taggart, G. R. Dickson, S. J. Mcmahon, and . . Prise, "Cell type-dependent uptake, localization, and cytotoxicity of 1.9 nm gold nanoparticles," *Int. J. Nanomedicine*, vol. 7, pp. 2673–2685, 2012, doi: 10.2147/IJN.S31751.

[181] Y. J. Gu, J. Cheng, C. C. Lin, Y. W. Lam, S. H. Cheng, and W. T. Wong, "Nuclear penetration of surface functionalized gold nanoparticles," *Toxicol. Appl. Pharmacol.*, vol. 237, no. 2, pp. 196–204, 2009, doi: 10.1016/j.taap.2009.03.009.

[182] G. Xu, S. Zeng, B. Zhang, M. T. Swihart, K. T. Yong, and P. N. Prasad, "New Generation Cadmium-Free Quantum Dots for Biophotonics and Nanomedicine," *Chem. Rev.*, vol. 116, no. 19, pp. 12234–12327, 2016, doi: 10.1021/acs.chemrev.6b00290.

[183] J. Langer, S. M. Novikov, and L. M. Liz-Marzán, "From nucleotides to DNA analysis by a SERS substrate of a self similar chain of silver nanospheres Related content Sensing

using plasmonic nanostructures and nanoparticles," 2015, doi: 10.1088/2040-8978/17/11/114021.

[184] A. Barhoumi, D. Zhang, F. Tam, and N. J. Halas, "Surface-Enhanced Raman Spectroscopy of DNA," doi: 10.1021/ja800023j.

[185] L. Ou, Y. Chen, Y. Su, C. Zou, and Z. Chen, "Detection of Genomic DNA Damage from Radiated Nasopharyngeal Carcinoma Cells Using Surface-Enhanced Raman Spectroscopy (SERS)," doi: 10.1177/0003702816671073.

[186] J. Morla-Folch, R. A. Alvarez-Puebla, and L. Guerrini, "Direct Quantification of DNA Base Composition by Surface-Enhanced Raman Scattering Spectroscopy," *J. Phys. Chem. Lett*, vol. 7, pp. 3037–3041, 2016, doi: 10.1021/acs.jpclett.6b01424.

[187] Y. Wang, Z. Wei, Y. Zhang, and Y. Chen, "Direct detection of DNA using 3D surface enhanced Raman scattering hotspot matrix," *Electrophoresis*, pp. 2104–2111, 2019, doi: 10.1002/elps.201900009.

[188] A. Barhoumi, D. Zhang, F. Tam, and N. J. Halas, "Surface-Enhanced Raman Spectroscopy of DNA," doi: 10.1021/ja800023j.

[189] E. Papadopoulou and S. E. J. Bell, "Angewandte Chemie DNA Analysis Label-Free Detection of Single-Base Mismatches in DNA by Surface-Enhanced Raman Spectroscopy**," doi: 10.1002/anie.201102776.

[190] F. Gao, J. Lei, and H. Ju, "Label-Free Surface-Enhanced Raman Spectroscopy for Sensitive DNA Detection by DNA-Mediated Silver Nanoparticle Growth," *Anal. Chem*, vol. 85, p. 28, 2013, doi: 10.1021/ac4032109.

[191] G. P. Szekeres and J. Kneipp, "SERS Probing of Proteins in Gold Nanoparticle Agglomerates," vol. 7, no. January, pp. 1–10, 2019, doi: 10.3389/fchem.2019.00030.

[192] D. Radziuk and H. Moehwald, "Highly effective hot spots for SERS signatures of live fibroblasts †," 2014, doi: 10.1039/c4nr00594e.

[193] E. Y. Lukianova-Hleb, Y. S. Kim, I. Belatsarkouski, A. M. Gillenwater, B. E. O'Neill, and D. O. Lapotko, "Intraoperative diagnostics and elimination of residual microtumours with plasmonic nanobubbles," *Nat. Nanotechnol.*, 2016, doi: 10.1038/nnano.2015.343.

[194] C. H. Li *et al.*, "Fluorescence-guided probes of aptamer-targeted gold nanoparticles with computed tomography imaging accesses for in vivo tumor resection," *Sci. Rep.*, vol. 5, 2015, doi: 10.1038/srep15675.

[195] R. Meir *et al.*, "Nanomedicine for Cancer Immunotherapy: Tracking Cancer-Specific T-Cells in Vivo with Gold Nanoparticles and CT Imaging," *ACS Nano*, 2015, doi: 10.1021/acsnano.5b01939.

[196] X. Jiang, S. Zong, C. Chen, Y. Zhang, Z. Wang, and Y. Cui, "Gold-carbon dots for the intracellular imaging of cancer-derived exosomes," *Nanotechnology*, vol. 29, no. 17, p. 175701, 2018, doi: 10.1088/1361-6528/aaaf14.

[197] L. V. Nair, S. S. Nazeer, R. S. Jayasree, and A. Ajayaghosh, "Fluorescence Imaging Assisted Photodynamic Therapy Using Photosensitizer-Linked Gold Quantum Clusters," *ACS Nano*, 2015, doi: 10.1021/acsnano.5b00406.

[198] R. Mendes, P. Pedrosa, J. C. Lima, A. R. Fernandes, and P. V Baptista, "Photothermal enhancement of chemotherapy in breast cancer by visible irradiation of Gold

Nanoparticles OPEN," doi: 10.1038/s41598-017-11491-8.

[199] H. Chen *et al.*, "Multifunctional gold nanostar conjugates for tumor imaging and

combined photothermal and chemo-therapy," *Theranostics*, vol. 3, no. 9, pp. 633–649,

2013, doi: 10.7150/thno.6630.

[200] Q. Dai *et al.*, "Quantifying the Ligand-Coated Nanoparticle Delivery to Cancer Cells in

Solid Tumours," 2018, doi: 10.1021/acsnano.8b03900.

[201] Y. H. Bae and K. Park, "Targeted drug delivery to tumors: Myths, reality and possibility,"

J. Control. Release, vol. 153, no. 3, pp. 198–205, 2011, doi:

10.1016/j.jconrel.2011.06.001.

[202] P. Magala, W. E. Bocik, A. Majumdar, and J. R. Tolman, "Conformational Dynamics

Modulate Activation of the Ubiquitin Conjugating Enzyme Ube2g2," 2017.

[203] J. H. Lee *et al.*, "Artificially engineered magnetic nanoparticles for ultra-sensitive

molecular imaging," *Nat. Med.*, vol. 13, no. 1, pp. 95–99, 2007, doi: 10.1038/nm1467.

[204] E. S. Davidi *et al.*, "Cisplatin-conjugated gold nanoparticles as a theranostic agent for

head and neck cancer," *Head Neck*, vol. 40, no. 1, pp. 70–78, 2018, doi:

10.1002/hed.24935.

[205] Z. Zhang *et al.*, "Silver Nanoparticle Gated, Mesoporous Silica Coated Gold Nanorods

(AuNR@MS@AgNPs): Low Premature Release and Multifunctional Cancer Theranostic

Platform," *ACS Appl. Mater. Interfaces*, vol. 7, p. 45, 2015, doi: 10.1021/acsami.5b00368.

[206] D. Dutta, A. Chattopadhyay, and S. S. Ghosh, "Cationic BSA Templated Au−Ag

Bimetallic Nanoclusters As a Theranostic Gene Delivery Vector for HeLa Cancer Cells,"

2016, doi: 10.1021/acsbiomaterials.6b00517.

[207] K. Lee, V. P. Drachev, and J. Irudayaraj, "DNA-gold nanoparticle reversible networks grown on cell surface marker sites: Application in diagnostics," *ACS Nano*, 2011, doi: 10.1021/nn1030862.

[208] E. B. Ehlerding, P. Grodzinski, W. Cai, and C. H. Liu, "Big Potential from Small Agents: Nanoparticles for Imaging-Based Companion Diagnostics," *ACS Nano*, p. acsnano.7b07252, 2018, doi: 10.1021/acsnano.7b07252.

[209] C. T. Matea *et al.*, "Quantum dots in imaging, drug delivery and sensor applications," *Int. J. Nanomedicine*, vol. 12, pp. 5421–5431, 2017, doi: 10.2147/IJN.S138624.

[210] M. A. Walling, J. A. Novak, and J. R. E. Shepard, "Quantum Dots for Live Cell and In Vivo Imaging," *OPEN ACCESS Int. J. Mol. Sci*, vol. 10, p. 10, 2009, doi: 10.3390/ijms10020441.

[211] J. Liu, M. Yu, C. Zhou, and J. Zheng, "Renal clearable inorganic nanoparticles: a new frontier of bionanotechnology," *Biochem. Pharmacol.*, vol. 16, pp. 477–486, 2013, doi: 10.1016/j.mattod.2013.11.003.

[212] Y. Kim, J.-H. Park, H. Lee, and J.-M. Nam, "How Do the Size, Charge and Shape of Nanoparticles Affect Amyloid β Aggregation on Brain Lipid Bilayer? OPEN," 2015, doi: 10.1038/srep19548.

[213] A. M. Alkilany and C. J. Murphy, "Toxicity and cellular uptake of gold nanoparticles: What we have learned so far?," *J. Nanoparticle Res.*, vol. 12, no. 7, pp. 2313–2333, 2010, doi: 10.1007/s11051-010-9911-8.

[214] Y. Pan *et al.*, "Gold nanoparticles of diameter 1.4 nm trigger necrosis by oxidative stress and mitochondrial damage," *Small*, vol. 5, no. 18, pp. 2067–2076, 2009, doi: 10.1002/smll.200900466.

[215] M. Turner *et al.*, "Selective oxidation with dioxygen by gold nanoparticle catalysts derived from 55-atom clusters," *Nature*, vol. 454, no. 7207, pp. 981–983, 2008, doi: 10.1038/nature07194.

[216] E. E. Connor, J. Mwamuka, A. Gole, C. J. Murphy, and M. D. Wyatt, "Gold nanoparticles are taken up by human cells but do not cause acute cytotoxicity," *Small*, vol. 1, no. 3, pp. 325–327, 2005, doi: 10.1002/smll.200400093.

[217] D. Mirska, K. Schirmer, S. S. Funari, A. Langner, B. Dobner, and G. Brezesinski, "Biophysical and biochemical properties of a binary lipid mixture for DNA transfection," *Colloids Surfaces B Biointerfaces*, vol. 40, no. 1, pp. 51–59, 2005, doi: 10.1016/j.colsurfb.2004.10.007.

[218] H. Shi, R. Asahi, and C. Stampfl, "Properties of the gold oxides Au2 O3 and Au2 O: First-principles investigation," *Phys. Rev. B - Condens. Matter Mater. Phys.*, vol. 75, no. 20, pp. 75–83, 2007, doi: 10.1103/PhysRevB.75.205125.

[219] J. Zheng, P. R. Nicovich, and R. M. Dickson, "Highly Fluorescent Noble Metal Quantum Dots," *Annu. Rev. Phys. Chem.*, vol. 22, no. 5, p. 4109, 2008, doi: 10.1146/annurev.physchem.58.032806.104546.Highly.

[220] J. Zheng, C. Zhang, and R. M. Dickson, "Highly fluorescent, water-soluble, size-tunable gold quantum dots," *Phys. Rev. Lett.*, vol. 93, no. 7, pp. 5–8, 2004, doi: 10.1103/PhysRevLett.93.077402.

[221] J. Zheng, J. T. Petty, and R. M. Dickson, "High quantum yield blue emission from water-soluble Au8 nanodots," *J. Am. Chem. Soc.*, vol. 125, no. 26, pp. 7780–7781, 2003, doi: 10.1021/ja035473v.

[222] M. A. Walling, J. A. Novak, and J. R. E. Shepard, "Quantum Dots for Live Cell and In Vivo Imaging," *OPEN ACCESS Int. J. Mol. Sci*, vol. 10, p. 10, 2009, doi: 10.3390/ijms10020441.

[223] A. Gaiduk, P. V. Ruijgrok, M. Yorulmaz, and M. Orrit, "Making gold nanoparticles fluorescent for simultaneous absorption and fluorescence detection on the single particle level," *Phys. Chem. Chem. Phys.*, 2011, doi: 10.1039/C0CP01389G.

[224] C. H. R, J. D. Schiffman, and R. Geetha Balakrishna, "Quantum dots as fluorescent probes: Synthesis, surface chemistry, energy transfer mechanisms, and applications," *Sensors Actuators B. Chem.*, vol. 258, pp. 1191–1214, 2018, doi: 10.1016/j.snb.2017.11.189.

[225] H. He, C. Xie, and J. Ren, "Nonbleaching Fluorescence of Gold Nanoparticles and Its Applications in Cancer Cell Imaging," *Proc. Natl. Acad. Sci. U.S.A*, vol. 120, no. 7, pp. 5951–5957, 1998, doi: 10.1021/ac8005796.

[226] K. D. Wegner and N. Hildebrandt, "Quantum dots: Bright and versatile in vitro and in vivo fluorescence imaging biosensors," *Chemical Society Reviews*. 2015, doi: 10.1039/c4cs00532e.

[227] Y. Jin and X. Gao, "Plasmonic fluorescent quantum dots," *Nat. Nanotechnol.*, 2009, doi: 10.1038/NNANO.2009.193.

[228] L. Minai, D. Yeheskely-Hayon, and D. Yelin, "High levels of reactive oxygen species in gold nanoparticle-targeted cancer cells following femtosecond pulse irradiation," *Sci. Rep.*, vol. 3, pp. 1–7, 2013, doi: 10.1038/srep02146.

[229] H. Huang, Y. yao Quan, X. ping Wang, and T. sheng Chen, "Gold Nanoparticles of Diameter 13 nm Induce Apoptosis in Rabbit Articular Chondrocytes," *Nanoscale Res. Lett.*, vol. 11, no. 1, 2016, doi: 10.1186/s11671-016-1461-2.

[230] H. R. McLennan and M. D. Esposti, "The contribution of mitochondrial respiratory complexes to the production of reactive oxygen species," *J. Bioenerg. Biomembr.*, vol. 32, no. 2, pp. 153–162, 2000, doi: 10.1023/A:1005507913372.

[231] J. St-Pierre, J. A. Buckingham, S. J. Roebuck, and M. D. Brand, "Topology of superoxide production from different sites in the mitochondrial electron transport chain," *J. Biol. Chem.*, vol. 277, no. 47, pp. 44784–44790, 2002, doi: 10.1074/jbc.M207217200.

[232] D. B. Zorov, M. Juhaszova, and S. J. Sollott, "Mitochondrial Reactive Oxygen Species (ROS) and ROS-Induced ROS Release," *Physiol. Rev.*, vol. 94, no. 3, pp. 909–950, 2014, doi: 10.1152/physrev.00026.2013.

[233] P. Storz, "Reactive oxygen species in tumor progression.," *Front. Biosci.*, vol. 10, pp. 1881–96, 2005, doi: 1667 [pii].

[234] H. Ying Jia *et al.*, "Potential Oxidative Stress of Gold Nanoparticles by Induced-NO Releasing in Serum," *J. AM. CHEM. SOC*, vol. 131, p. 50, 2009, doi: 10.1021/ja808033w.

[235] A. S. Thakor *et al.*, "Oxidative Stress Mediates the Effects of Raman-Active Gold Nanoparticles in Human Cells," *Small*, vol. 7, no. 1, pp. 126–136, 2011, doi:

10.1002/smll.201001466.

[236] D. Han, E. Williams, and E. Cadenas, "Mitochondrial respiratory chain-dependent generation of superoxide anion and its release into the intermembrane space," *Biochem. J.*, vol. 353, no. 2, pp. 411–416, 2001, doi: 10.1042/0264-6021:3530411.

[237] K. K. Singh, "Mitochondria damage checkpoint in apoptosis and genome stability," *FEMS Yeast Res.*, vol. 5, no. 2, pp. 127–132, 2004, doi: 10.1016/j.femsyr.2004.04.008.

[238] S. Biswas and V. P. Torchilin, "Nanopreparations for organelle-specific delivery in cancer," *Adv. Drug Deliv. Rev.*, vol. 66, pp. 26–41, 2014, doi: 10.1016/j.addr.2013.11.004.

[239] V. Borutaite, "Mitochondria as decision-makers in cell death," *Environ. Mol. Mutagen.*, vol. 51, no. 5, p. NA-NA, Jun. 2010, doi: 10.1002/em.20564.

[240] L. Wang *et al.*, "Selective targeting of gold nanorods at the mitochondria of cancer cells: Implications for cancer therapy," *Nano Lett.*, vol. 11, no. 2, pp. 772–780, 2011, doi: 10.1021/nl103992v.

[241] E. Cadenas, "Mitochondrial free radical production and cell signaling," *Mol. Aspects Med.*, vol. 25, no. 1–2, pp. 17–26, 2004, doi: 10.1016/j.mam.2004.02.005.

[242] R. T. Allen, W. J. Hunter, and D. K. Agrawal, "Morphological and biochemical characterization and analysis of apoptosis.," *J. Pharmacol. Toxicol. Methods*, vol. 37, no. 4, pp. 215–228, 1997, doi: 10.1016/S1056-8719(97)00033-6.

[243] C. Carr, J. Ng, and T. Wigmore, "The side effects of chemotherapeutic agents," *Curr. Anaesth. Crit. Care*, vol. 19, pp. 70–79, 2008, doi: 10.1016/j.cacc.2008.01.004.

[244] N. O. Vietor and B. J. George, "Oxaliplatin-induced hepatocellular injury and ototoxicity:

A review of the literature and report of unusual side effects of a commonly used chemotherapeutic agent," *J. Oncol. Pharm. Pract.*, vol. 18, no. 3, pp. 355–359, 2012, doi: 10.1177/1078155212437901.

[245] G. Housman *et al.*, "Drug Resistance in Cancer: An Overview," *Cancers (Basel).*, vol. 6, pp. 1769–1792, 2014, doi: 10.3390/cancers6031769.

[246] B. Mansoori, A. Mohammadi, S. Davudian, S. Shirjang, and B. Baradaran, "The Different Mechanisms of Cancer Drug Resistance: A Brief Review," *Adv Pharm Bull*, vol. 7, no. 3, pp. 339–348, 2017, doi: 10.15171/apb.2017.041.

[247] M. Matulionyte, D. Dapkute, L. Budenaite, G. Jarockyte, and R. Rotomskis, "Photoluminescent gold nanoclusters in cancer cells: Cellular uptake, toxicity, and generation of reactive oxygen species," *Int. J. Mol. Sci.*, vol. 18, no. 2, pp. 1–17, 2017, doi: 10.3390/ijms18020378.

[248] E. G. Gamaly, A. V. Rode, B. Luther-Davies, and V. T. Tikhonchuk, "Ablation of solids by femtosecond lasers: Ablation mechanism and ablation thresholds for metals and dielectrics," *Phys. Plasmas*, vol. 9, no. 3, p. 949, 2002, doi: 10.1063/1.1447555.

[249] D. von der Linde and K. Sokolowski-Tinten, "The physical mechanisms of short-pulse laser ablation," *Appl. Surf. Sci.*, vol. 154, pp. 1–10, 2000, doi: 10.1016/S0169-4332(99)00440-7.

[250] L. M. Xiao *et al.*, "In-fiber Silicon Microspheres."

[251] G. J. Triggs, G. J. O. Evans, and T. F. Krauss, "Degradation of silicon photonic biosensors in cell culture media: analysis and prevention," *Biomed. Opt. Express*, vol. 8, no. 6, p.

2924, 2017, doi: 10.1364/boe.8.002924.

[252] J. Chen *et al.*, "Variation in carbohydrates between cancer and normal cell membranes revealed by super-resolution fluorescence imaging," *Adv. Sci.*, vol. 3, no. 12, 2016, doi: 10.1002/advs.201600270.

[253] G. Rago *et al.*, "Uptake of Gold Nanoparticles in Healthy and Tumor Cells Visualized by Nonlinear Optical Microscopy," *J. Phys. Chem. B*, vol. 115, p. 36, 2011, doi: 10.1021/jp2009012.

[254] J. A. Ryan *et al.*, "Cellular uptake of gold nanoparticles passivated with BSA-SV40 large T antigen conjugates," *Anal. Chem.*, vol. 79, no. 23, pp. 9150–9159, 2007, doi: 10.1021/ac0715524.

[255] N. DB, "Cancer Cell Nucleus: An Insight," *J. Mol. Biomark. Diagn.*, vol. 8, no. s2, pp. 1–8, 2017, doi: 10.4172/2155-9929.S2-026.

[256] J. R. Tang, N. A. M. Isa, and E. S. Ch'Ng, "Evaluating nuclear membrane irregularity for the classification of cervical squamous epithelial cells," *PLoS One*, vol. 11, no. 10, 2016, doi: 10.1371/journal.pone.0164389.

[257] "General Properties of Silicon." [Online]. Available: https://pvcdrom.pveducation.org/APPEND/Silicon.htm. [Accessed: 13-Jun-2019].

[258] G. Elert, "Density - The Physics Hypertextbook," 2013. [Online]. Available: http://physics.info/density/. [Accessed: 13-Jun-2019].